

**Structure/ Reactivity study of model and biodiesel soot in
DPF regeneration conditions**

Ophélie Pereira

Thesis to obtain the Master of Science Degree in

Chemical Engineering

Supervisors: Prof. Carlos Manuel Faria de Barros Henriques (IST)

Prof. Patrick da Costa (Sorbonne Université)

Examination Committee

Chairperson: Francisco Manuel Da Silva Lemos

Supervisor: Prof. Carlos Manuel Faria de Barros Henriques

Member of the Committee: Prof. Mário Manuel Gonçalves da Costa

June 2018

This work was done in collaboration with



“Pleasure in the job puts perfection in the work.”

Aristotle

THIS PAGE WAS INTENTIONALLY LEFT BLANK

Acknowledgements

The present work was accomplished at Institut Jean Le Rond D'Alembert (IJLRA) of Sorbonne Université. This project was not possible without the collaboration and help of many people I met there. To them, I express all my gratitude.

I would like to thank Professor Carlos Henriques, for the given opportunity of developing this work at the IJLRA, for the provided help during the internship and for the final revision of this work. I also would like to thank Professor Patrick da Costa for all the dedication, support and precious advices provided throughout this internship. It was a pleasure to work with you both. All their scientific support contributed to improve my knowledge. Of course, I also would like to express my gratitude to Renault-Volvo Trucks for supplying some soot samples.

I also would like to express my gratitude to Professor Elena Galves, Jérôme Bonnet and Renaud Jalain for their help. The several conversations allowed to a better understanding of the subject and to discuss many points of view. I want to thank Hailong Zhang for being a great work partner. It was not possible to do all this without each other's help.

During this internship I met extraordinary people, who made my time in Paris amazing. To them: Renaud, Armando, Kasia, Sandrine, Achraf, Lauréanne, Natalia, María, Mira, António and Marta, thank you for everything. With them, I shared office, coffee, lunches, parties and travels, which made these months unforgettable.

To my friends at IST who stayed in Portugal but made me the enormous pleasure to visit me. To my friends from my home town, who have seen me grow as a person. Finally, to my family for their huge support. Especially, to my parents, for never stop to believe in me.

THIS PAGE WAS INTENTIONALLY LEFT BLANK

Abstract

This study aimed to evaluate the effect of oxygenated compounds concentration and the length of their carbon chains, on the structure and reactivity of soot. These particles, which were obtained from diesel/biodiesel surrogates, in an atmospheric Santoro-type burner with a diffusion flame, were called “model” particles. A comparative analysis was carried out between “model” samples and soot produced on an engine bench, representative of heavy-duty vehicle engine. Soot characteristics were studied through diverse techniques, such as laser granulometry, elemental analysis (CHNS/O), thermogravimetric analysis (TGA), Raman spectroscopy and transmission electron microscopy (TEM). Higher content and/or carbon chain length of the studied compounds promoted the formation of smaller particles. Oxygen and Soluble Organic Fraction (SOF) content in soot samples decreased with higher concentration and/or chain length. No significant dissimilarities were registered in the graphitic structures. Temperature Programmed Oxidations (TPO) were performed to correlate soot composition and structure with oxidation reactivity. Soot from surrogates with higher oxygenated compounds concentration revealed a lower reactivity. During a catalytic study, the impact of the presence of MnO_x-CeO₂- type catalyst on soot oxidation was analysed. The temperature to obtain 10% of carbon conversion showed considerable modifications. The decrease of temperature in the case of “real” soot was probably due to the oxidation of the Soluble Organic Fraction. The synergetic effect of oxygen and nitrogen dioxide was evaluated. Finally, the impact of the soot-catalyst contact was assessed. Generally, the obtained results revealed that “model” particles had a structure and reactivity comparable to particles produced in real conditions.

KEYWORDS

Model soot, biodiesel, DPF, soot reactivity, regeneration

THIS PAGE WAS INTENTIONALLY LEFT BLANK

Resumo

Este estudo pretendeu avaliar o efeito da concentração de compostos oxigenados e do comprimento das cadeias de carbono, na estrutura e reatividade da fuligem. Estas partículas, obtidas a partir de substitutos de diesel/biodiesel, num queimador de Santoro à pressão atmosférica com uma chama de difusão, foram designadas partículas “modelo”. Uma análise comparativa foi realizada entre amostras “modelo” e fuligem produzida em banco de ensaio, representativa de um motor de veículo pesado. As suas características foram estudadas através de diversas técnicas, como granulometria laser, análise elementar, análise termogravimétrica, espectroscopia Raman e microscopia eletrónica de transmissão. Um maior teor e/ou comprimento de cadeia dos compostos promoveu a formação de menores partículas. O conteúdo em oxigénio e fração orgânica solúvel diminuíram com o aumento da concentração e/ou comprimento de cadeia. Nenhuma diferença significativa foi registada na estrutura gráfica. Oxidações a temperatura programada foram efetuadas para relacionar a composição e estrutura da fuligem com a oxidação. A fuligem obtida com maiores concentrações de compostos oxigenados revelou uma menor reatividade. Durante um estudo catalítico, o impacto da presença de catalisadores MnO_x - CeO_2 na oxidação das partículas foi analisado. A temperatura para obter 10% de conversão de carbono mostrou modificações consideráveis. A diminuição de temperatura para a fuligem “real” deveu-se provavelmente à oxidação da fração orgânica solúvel. O efeito sinérgico do oxigénio e dióxido de azoto foi avaliado. Finalmente, estudou-se o impacto do contacto fuligem-catalisador. De modo geral, os resultados obtidos revelaram que as partículas “modelo” possuíam uma estrutura e reatividade comparáveis às produzidas em condições reais.

PALAVRAS-CHAVE

Fuligem modelo, biodiesel, DPF, reatividade de fuligem, regeneração

THIS PAGE WAS INTENTIONALLY LEFT BLANK

Table of contents

1 Context and Objectives	1
2 State of the Art	5
2.1 Biodiesel.....	5
2.2 Mechanism of soot formation.....	7
2.3 Properties of diesel soot.....	9
2.3.1 Composition.....	9
2.3.2 Impact of biodiesel on soot nanostructure and reactivity.....	10
2.3.3 Diesel soot oxidation.....	12
2.4 Exhaust post-treatment system.....	14
2.4.1 Diesel Particulate Filter (DPF).....	15
3 Experimental methodology	21
3.1 Soot generation.....	21
3.2 Laser particle size analysis.....	23
3.3 Elemental Analysis: CHNS/O.....	24
3.4 Thermogravimetric Analysis (TGA).....	24
3.5 Raman Spectroscopy.....	25
3.6 Transmission Electron Microscopy (TEM).....	27
3.7 Temperature Programmed Oxidation (TPO).....	28
3.7.1 Non-catalytic oxidation.....	28
3.7.2 Catalytic oxidation.....	29
4 Results and discussion	31
4.1 Soot structure and composition.....	31
4.1.1 Particles size distribution: Aggregates.....	31
4.1.2 Soot composition.....	37
4.1.3 Raman Spectroscopy.....	38
4.1.4 Nanostructure.....	40
4.2 Soot oxidation reactivity.....	51
4.2.1 Non-catalytic soot oxidation.....	51
4.2.2 Catalytic soot oxidation.....	56
5 Conclusion	63
6 Future perspectives	65
7 References	67
8 Appendix	a
A. TEM image processing with <i>Image J</i> ®.....	a
B. Calculation of soot conversion.....	c
C. Laser particle size analysis.....	d
D. Thermogravimetric analysis (TGA).....	e

E.	Raman Spectroscopy.....	f
F.	Transmission Electron Microscopy (TEM)	h
G.	Characterization of MnO _x -CeO ₂ mixed oxides.....	l
H.	Temperature programmed oxidation (TPO).....	m

List of tables

Table 1. European Emission Standards for diesel passenger cars [6].	2
Table 2. European Emission Standards for Heavy-Duty diesel engines [6].	2
Table 3. Statistics of effect of pure biodiesel on engine emissions [18].	5
Table 4. Composition of diesel and biodiesel surrogates.	22
Table 5. Chemical formula and structure of methyl ester-based additives used for biodiesel surrogates.	22
Table 6. Composition of soot.	37
Table 7. FWHM (cm^{-1}) of D1 band, Raman shift (cm^{-1}) of G band and I_{D3}/I_G ratio obtained through Raman spectrums of the studied soot samples.	39
Table 8. Mean value (nm) and standard deviation (σ) of the normal distribution of soot fringe length from diesel surrogate «Aref» and biodiesel surrogates «MB7», «MO7» and «MD7».	47
Table 9. Mean value (nm) and standard deviation (σ) of the normal distribution of soot fringe length from diesel surrogate «Aref», biodiesel surrogates «MD», as well as “real” diesel and biodiesel.	49
Table 10. Temperature programmed oxidation results in 9% O_2/Ar .	52
Table 11. Temperature programmed oxidation results in 400 ppmv $\text{NO}_2 + 9\% \text{O}_2/\text{Ar}$.	54
Table 12. Temperature programmed oxidation results in 9% O_2/Ar , in “loose” contact conditions.	57
Table 13. Temperature programmed oxidation results in 9% O_2/Ar in presence of mixed oxides, under “loose”, “pressure” and “tight” conditions.	59
Table 14. Temperature programmed oxidation results in 400 ppmv $\text{NO}_2 + 9\% \text{O}_2/\text{Ar}$, in “loose” contact conditions.	60
Table E- 1. Results of Raman spectroscopy for «Aref» soot.	f
Table E- 2. Results of Raman spectroscopy for «MB7» soot.	f
Table E- 3. Results of Raman spectroscopy for «MO7» soot.	g
Table E- 4. Results of Raman spectroscopy for «MD7» soot.	g
Table E- 5. Results of Raman spectroscopy for «MB30» soot.	g
Table E- 6. Results of Raman spectroscopy for «MO30» soot.	g
Table E- 7. Results of Raman spectroscopy for «MD30» soot.	g
Table E- 8. Results of Raman spectroscopy for «B7-BM» soot.	h
Table E- 9. Results of Raman spectroscopy for «B100-BM» soot.	h
Table G- 1. XPS results of the $\text{MnO}_x\text{-CeO}_2$ catalyst.	l

THIS PAGE WAS INTENTIONALLY LEFT BLANK

List of figures

Figure 1. a) Evolution of GHG emissions between 1990 and 2015 in the EU-28 (emissions from transport include those from international aviation but exclude international shipping) [5]. b) Share of GHG emissions by transport mode, EU 28, 2017 [5].	1
Figure 2. Transesterification reaction [17].	5
Figure 3. a) Chemical reactions and physical processes involved in soot formation [38].	7
Figure 4. Elemental particle of soot produced in the combustion chamber of a diesel engine [47].	9
Figure 5. Schematic representation of diesel particulate matter (soot) [51].	9
Figure 6. Internal structure of diesel soot [55].	10
Figure 7. HRTEM images of soot from B100 and B0 [62].	11
Figure 8. Internal combustion process of B100 soot with O ₂ , proposed by Song. et al. [60].	14
Figure 9. After-treatment system of exhaust emissions [80].	14
Figure 10. a) Cordierite honeycomb ceramic [85]. b) Schematic view of a wall-flow filter [81].	15
Figure 11. Schematic representation of the soot combustion mechanism of the Ce-based catalysts. a) active oxygen mechanism. b) NO ₂ -assisted mechanism [112].	19
Figure 12. Introduction of Mn in the CeO ₂ lattice and evolution of oxygen vacancies in soot oxidation [107].	19
Figure 13. Configuration of the burner to establish a non-premixed flame as described by Santoro et al. [117].	21
Figure 14. Optical structure of the ANALYSETTE 22 FRITSCH NanoTec. a) IR laser active.	23
Figure 15. Layout for CHNS/O determination [125].	24
Figure 16. Jablonski Diagram representing the working principle of Raman spectroscopy [126].	25
Figure 17. Example of the decomposition of a Raman Spectre ($\lambda_0=514$ nm) of untreated EURO VI soot, in five Lorentzian bands [129].	26
Figure 18. a) Diagram of the optical electron beam in a TEM microscope [130]. b) JEOL JEM 100CX transmission electron microscope.	27
Figure 19. a) Quartz reactor. b) Installation diagram for TPO experiments under 9% O ₂ /Ar.	28
Figure 20. TEM images of «Aref» soot at 200, 50 and 10 nm, respectively.	32
Figure 21. Size distribution of “model” soot aggregates from the diesel surrogate and biodiesel surrogates (7%).	32
Figure 22. Main pathways of CO and CO ₂ formation via pyrolysis or oxidation of methyl ester compounds at high and/or low temperature as proposed by Coniglio et al. [4]. Dashed arrows mean several successive reactions.	34
Figure 23. Size distribution of “MD” soot aggregates with 7% and 30% of additives and of “real” soot.	35
Figure 24. a) Typical locations of soot formation in a diffusion flame [140]. c) Santoro burner used to obtain “model” soot, with a stable diffusion flame.	36
Figure 25. Raman spectrum of «B100-BM» soot sample.	39

Figure 26. HR-TEM images of «MD7», «MD30» and «Aref» soot samples.	40
Figure 27. HR-TEM images of «MB7», «MB30», «MO7» and «MO30» soot samples.....	42
Figure 28. HR-TEM images of soot collected on engine bench.....	42
Figure 29. Size distribution of soot spherules from the diesel surrogate «Aref» and surrogates biodiesel with 7 and 30% of additives.....	43
Figure 30. Size distribution of soot spherules from biodiesel surrogates with 7 and 30% of additives and from the combustion of a fuel on an engine bench (B7-BM and B100-BM).....	43
Figure 31. Common fatty acid methyl ester (FAME) found in biodiesel [149].	44
Figure 32. Experimental cumulative curve of «MD30» size distribution.	45
Figure 33. Theoretical and experimental cumulative curves of «MD30» size distribution.	46
Figure 34. Carbon fringe length distribution of soot produced by combustion of the diesel surrogate «Aref» and biodiesel surrogates with 7% of methyl ester-based additives.....	47
Figure 35. Carbon fringe length distribution of soot produced by combustion of «Aref», biodiesel surrogates with 7 and 30% of methyl decanoate and fuel on engine bench (7 and 100%).	48
Figure 36. Particle nanostructure parameters [158].	49
Figure 37. Carbon specific oxidation rate (mg/(s.g _{in})) of “model” and “real” soot (9% O ₂ /Ar).	52
Figure 38. Carbon specific oxidation rate (mg/(s.g _{in})) of “model” and “real” soot (400 ppmv NO ₂ +9% O ₂ /Ar).....	54
Figure 39. Carbon specific oxidation rate (mg/(s.g _{in})) of “model” and “real” soot in presence of MnO _x -CeO ₂ mixed oxides (9% O ₂ /Ar), in “loose” contact conditions.....	56
Figure 40. Carbon specific oxidation rate (mg/(s.g _{in})) of «MD30» soot in presence of MnO _x -CeO ₂ mixed oxides (9% O ₂ /Ar).	58
Figure 41. Carbon specific oxidation rate (mg/(s.g _{in})) of «B100-BM» soot in presence of MnO _x -CeO ₂ mixed oxides (9% O ₂ /Ar).	58
Figure 42. Carbon specific oxidation rate (mg/(s.g _{in})) of «MD30» and «B100-BM» soot samples in presence of MnO _x -CeO ₂ mixed oxides (400 ppmv NO ₂ + 9% O ₂ /Ar).	60
Figure 43. T _i and T _m values of soot oxidation.....	61
Figure 44. Santoro-type burner, at moderated pressure.....	65
Figure A- 1. Definition of the scale (conversion of pixels into nanometres).	a
Figure A- 2. Selection of the area of interest (blue square).	a
Figure A- 3. a) Zone of interest. b) Application of a filter and reduction of the noise. c) Filtered image. b	
Figure A- 4. Application of a threshold brightness value (conversion into a binary format).	b
Figure A- 5. Measurement of the length of parallel carbon fringes.	c
Figure B- 1. Cumulative curve of CO _x emissions in function of the temperature for «B100-BM» sample, under 9% O ₂ /Ar.....	c
Figure C- 1. Size distribution of “model” soot aggregates from the diesel surrogate and biodiesel surrogates (30%).	d

Figure C- 2. Size distribution of “model” soot aggregates from biodiesel surrogates with 7 and 30% of methyl butanoate.	d
Figure C- 3. Size distribution of “model” soot aggregates from biodiesel surrogates with 7 and 30% of methyl octanoate.	d
Figure D- 1. Thermogravimetric analysis under nitrogen (a) and under air (b) of “model” soot from biodiesel surrogates with 7% of methyl ester-based additives and from diesel surrogate «Aref».	e
Figure D- 2. Thermogravimetric analysis under nitrogen (a) and under air (b) of “model” soot from biodiesel surrogates with 30% of methyl ester-based additives and from diesel surrogate «Aref».	f
Figure F- 1. Theoretical and experimental cumulative curves of «Aref» size distribution.	h
Figure F- 2. Theoretical and experimental cumulative curves of «MB7» size distribution.	i
Figure F- 3. Theoretical and experimental cumulative curves of «MO7» size distribution.	i
Figure F- 4. Theoretical and experimental cumulative curves of «MD7» size distribution.	i
Figure F- 5. Theoretical and experimental cumulative curves of «MB30» size distribution.	j
Figure F- 6. Theoretical and experimental cumulative curves of «MO30» size distribution.	j
Figure F- 7. Theoretical and experimental cumulative curves of «B7-BM» size distribution.	j
Figure F- 8. Theoretical and experimental cumulative curves of «B100-BM» size distribution.	k
Figure F- 9. Carbon fringe length distribution of soot produced by combustion of «Aref» and biodiesel surrogates with 30% of methyl ester-based additives.	k
Figure F- 10. Carbon fringe length distribution of soot produced by combustion of «Aref» and biodiesel surrogates with 7 and 30% of methyl butanoate.	k
Figure F- 11. Carbon fringe length distribution of soot produced by combustion of «Aref» and biodiesel surrogates with 7 and 30% of methyl octanoate.	l
Figure H- 1. Carbon specific oxidation rate (mg/(s.g _{in})) of «MD7» soot, in loose, pressure and tight contact conditions, under 9%O ₂ and 91%Ar.	m
Figure H- 2. Carbon specific oxidation rate (mg/(s.g _{in})) of «B7-BM» soot, in loose, pressure and tight contact conditions, under 9%O ₂ and 91%Ar.	m

THIS PAGE WAS INTENTIONALLY LEFT BLANK

List of abbreviations

EIA – U.S. Energy Information Administration

GHG – Greenhouse Gases

HD – High-Duty

PM – Particulate Matter

IEA – International Energy Agency

FAME – Fatty Acid Methyl Ester

PAH – Polycyclic Aromatic Hydrocarbons

a.m.u – atomic mass unit

SOF – Soluble Organic Fraction

IOF – Insoluble Organic Fraction

VOF – Volatile Organic Fraction

HR-TEM – High Resolution Transmission Electron Microscopy

TGA – Thermogravimetric Analysis

TPO – Temperature Programmed Oxidation

DOC – Diesel Oxidation Catalyst

SCR – Selective Catalytic Reduction

DPF – Diesel Particulate Filter

CRT – Continuously Regenerating Trap

BM - Banc Moteur (Engine Bench)

SOC – Surface Oxygen Complex

THIS PAGE WAS INTENTIONALLY LEFT BLANK

1 Context and Objectives

Over the years, global energy consumption has been continuously increasing. According to the U.S. Energy Information Administration (EIA), a rise of 28% between 2015 and 2040 shall occur [1]. Renewables are expected to be the fastest-growing energy source, with a world consumption increase of 2,3% per year between 2015 and 2040 [1]. However, fossil fuels will still account for more than three-quarters of global energy use in this time gap [1].

Liquid fuels (especially petroleum-based) are the most widely used energy resource by world's population, exceeding natural gas, coal, nuclear energy and renewable materials. They achieved a global consumption of 33% in 2015, among all energy sources [1]. Unfortunately, this development has been accompanied by numerous issues from the environmental point of view, representing the major emissions source of greenhouse gases (GHG) in the automobile sector [2,3]. In fact, due to the worldwide extreme growth of this area, CO₂ emissions into the atmosphere have almost doubled over the last 30 years and are still expected to increase in the following ones [4]. Thus, innumerable improvements related to the emissions from engines have been carried out over the past 25 years. Air quality limits started to be controlled and some measures have been implemented at the local level to manage transport use, such as improvement transport planning and public transport incentives [2].

Despite the notorious break down of GHG emissions from all other main sectors in the last decades (Figure 1.a), emissions from transportation didn't experienced the same gradual decline. They just started to decrease in 2007 and remained higher than in 1990 (Figure 1.a) [5]. In particular, road transport accounts for almost 73% of the total emissions from the transport area (Figure 1.b) [5], contributing about 23% of the EU's total emissions of CO₂, 30% of NO_x and 12% of PM [2].

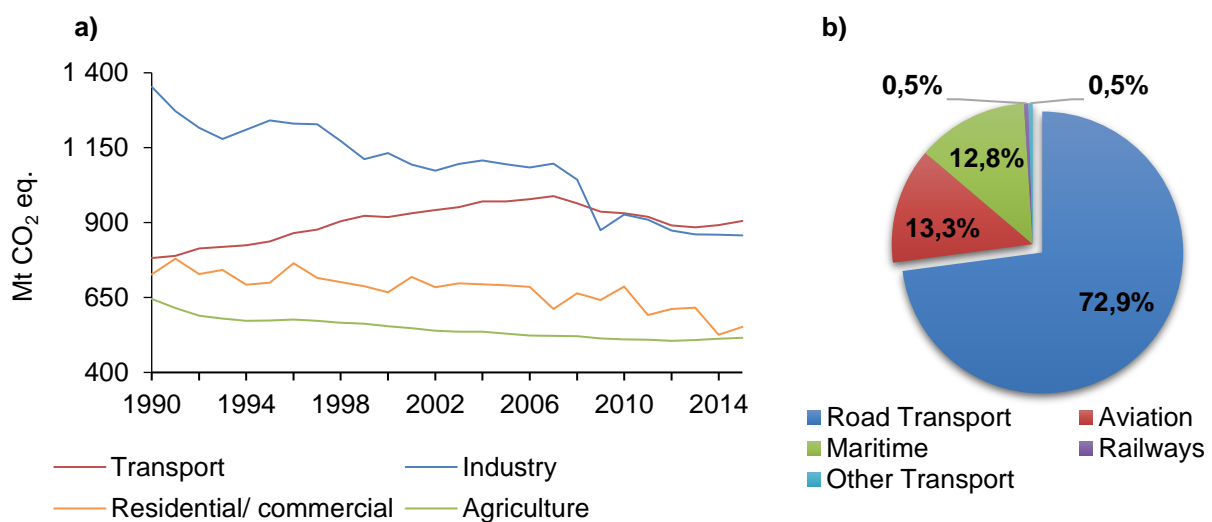


Figure 1. a) Evolution of GHG emissions between 1990 and 2015 in the EU-28 (emissions from transport include those from international aviation but exclude international shipping) [5]. b) Share of GHG emissions by transport mode, EU 28, 2017 [5].

Global warming and climatic changes have been such a sensitive and important issue that the European governments decided to implement new procedures to control the current situation. In 1992, the *Euro standards* were introduced. At the moment, the heavy-duty standards are numbered with Roman numerals (Euro I – Euro VI), whereas light-duty standards use Arabic numbers (Euro 1 – Euro 6) [6]. In [Table 1](#) and [Table 2](#) are summarised the limits of emission established in each *Euro standard* for passenger cars and heavy-duty (HD) vehicles, respectively [6].

Table 1. European Emission Standards for diesel passenger cars [6].

Standards	Date	CO (g/km)	NO _x (g/km)	HC (g/km)	NO _x + HC (g/km)	PM (g/km)	PN (#/km)
Euro 1	1992	2,72	-	-	0,97	0,14	-
Euro 2	1996 (IDI)	1,0	-	-	0,7	0,08	-
	1996 (DI)	1,0	-	-	0,9	0,10	-
Euro 3	2000	0,64	0,50	-	0,56	0,05	-
Euro 4	2005	0,50	0,25	-	0,30	0,025	-
Euro 5a	2009	0,50	0,18	-	0,23	0,005	-
Euro 5b	2011	0,50	0,18	-	0,23	0,005	6,0×10 ¹¹
Euro 6	2014	0,50	0,18	-	0,17	0,005	6,0×10 ¹¹

Table 2. European Emission Standards for Heavy-Duty diesel engines [6].

Standards	Date	CO (g/kWh)	NO _x (g/kWh)	HC (g/kWh)	PM (mass) (g/kWh)	PN (number) (#/kWh)
Euro I	1992 (<85kW)	4,5	8,0	1,1	0,612	-
	1992 (>85kW)	4,5	8,0	1,1	0,36	-
Euro II	1996	4,0	7,0	1,1	0,25	-
	1998	4,0	7,0	1,1	0,15	-
Euro III	2000	2,1	5,0	0,66	0,10	-
Euro IV	2005	1,5	3,5	0,46	0,02	-
Euro V	2008	1,5	2,0	0,46	0,02	-
Euro VI	2013	1,5	0,4	0,13	0,01	8,0×10 ¹¹

Among the regulated pollutants, particulate matter (PM) is one of the most important concerning combustion of hydrocarbon fuels. Their emissions from current diesel technologies are close to the limits permitted by regulations and will be even more stringent in the next future. Furthermore, the presence of such particles in urban air poses a serious public health problem even at low concentration. In fact, risks of cardiac arrest, pulmonary diseases, pregnancy complications and asthma are increased. Some studies also highlight their critical role in global warming due to the ability to absorb the incoming solar radiation [3]. Therefore, since *Euro 5b standard* for diesel passenger cars and *Euro VI* for HD vehicles, particulate emissions are not just considered in mass anymore, but also in number due to the hazardous effect of smaller ones (nanoparticles) [6].

An improved knowledge of the potential to reduce these types of emissions could help engine manufacturers to develop more ecologic systems and to adapt their engines, readjusting the compromise between efficiency, cost and emissions. Thus, some progresses in terms of motorisation and post-treatment systems have been accomplished [7]. Moreover, the scientific community has worked to find alternative sustainable and more efficient sources of energy, which generate reduced emissions. In this way, biofuels have emerged as one of the most strategically important fuel sources.

Obtained by natural resources, biofuels are renewable and can recycle carbon dioxide. In other words, emissions of CO₂ from combustion engines correspond to the amount that was already absorbed by plants through photosynthetic ways, representing a source of energy for biofuel growth [8]. Therefore, the use of biofuels becomes a solution to limit greenhouse gas emissions, improve air quality and prevent global warming. In fact, CO₂ emission can be reduced by 78%, CO by 46,7%, HCs by 45,2% and PM by 66,7% when compared with fossil fuel [8]. Additionally, they are more evenly distributed geographically than fossil fuels, providing to developed and developing nations energy supply independence and increased employment opportunities [9,10]. Finally, they can be blended with conventional fossil fuels, reducing emissions with any or little modifications in the vehicles and engines, unlike other renewable energy sources.

In 2009, the EU adopted the *Renewable Energy Directive* (RED – directive 2009/28/EC) [11], imposing to the Member States to provide 10% of renewable energy in transport by 2020. Additionally, the *Fuel Quality Directive* (FQD – Directive 2009/30/EC) [12] was adopted, obliging fuel suppliers to reduce greenhouse gas emissions by at least 6%, also by 2020, compared to the EU-average level of life cycle greenhouse gas emissions per unit of energy from fossil fuels in 2010.

Biofuels use has also some disadvantages. They rely mainly on agricultural crops (first-generation biofuels) and therefore compete with food production, promotes monocultures and use large quantities of fertilizers. Both RED and FQD directives did not consider the GHG emissions linked to *Indirect Land Use Change* (ILUC). Consequently, in October 2012, the European Commission published a proposal (COM (2012) 595) [13] to limit the use of agriculture-based biofuels to 5%, keeping the 10% renewable energy target of the RED. The remainder of the biofuel required to meet the 10% target would then have to come from wastes and other renewable sources. However, some heavy-duty vehicles (buses, trucks) can work exclusively with pure biodiesel.

At present, to produce liquid fuels, only first-generation biofuels are in commercial production and, despite several pilot-scale second-generation plants and plans for large-scale demonstration plants, it is generally recognised that second-generation biofuels (from biomass) are at least 10 years away from commercial-scale production. Furthermore, there are reasons to be concerned about the use of biomass to produce transport fuel. Second-generation biofuels, derived from the inedible or woody parts of plants have potential, but are limited by the amount of material that can be supplied sustainably as feedstock and by demand for material, for example straw and fodder. On the other hand, third-generation biofuels, using advanced biotechnology, for example to produce algae as feedstock, are a still longer-term prospect and there is much research to be done before they become viable [14].

To conclude, it seems that the major burden of providing biofuels for the EU 10% target in 2020 will fall on first-generation biofuels and for now, despite their disadvantages, first-generation biofuels are

still the most practical and realistic option. However, this transition to the renewable energy must be done progressively since the effect of intensive use of biofuels in emission of pollutants and post-treatment systems is still a subject of investigation.

The aim of this work is to widen the current knowledge about the reactivity of soot. It is focused on the comparison between particles produced with an academic burner of Santoro [15], which are classified as “models”, and particles resulting from the combustion of fuel in an engine bench, which is representative of an engine on a heavy-duty vehicle on road (Renault-Volvo Trucks). These last ones are classified as “real” soot. Given the fact that trucks operate with diesel fuel, use of biodiesel as an alternative to diesel is investigated. Along this study, the influence of different structures of ester molecules present in biodiesel and different concentrations of these compounds, on soot composition and structure is investigated. Then, soot properties are correlated with soot oxidative reactivity. Furthermore, with the aim to improve the efficiency of Diesel Particulate Filters and consequently to reduce soot emissions, the regeneration process is studied as well as the interaction between a catalyst (representative of a catalytic DPF) and soot.

2 State of the Art

2.1 Biodiesel

Biodiesel, composed by long carbonaceous chains highly saturated in alkyl esters, is produced from vegetable oils or animal fats. It is formed through a transesterification reaction between a triglyceride and an alcohol, yielding fatty acid methyl-esters (FAME) as biodiesel and glycerol as by-product. Globally, the stoichiometry of the reaction is 3:1 alcohols to triglycerides, which forms 3 moles of esters and 1 mole of glycerol (Figure 2). In practice, a higher molar ratio is used due to the reversibility of the reaction, while a catalyst is employed to increase the reaction rate and yield [16,17].

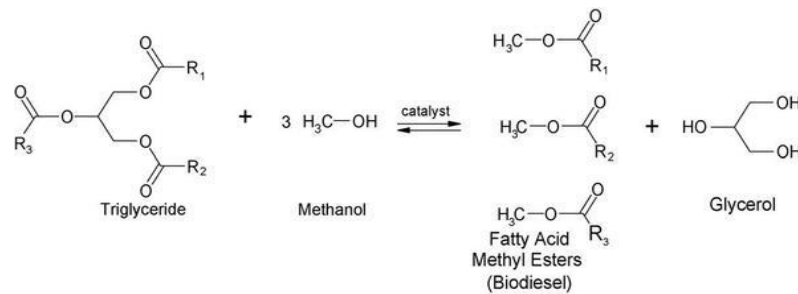


Figure 2. Transesterification reaction [17].

It must be kept in mind that the characteristics of biofuels depend on the raw-materials. Each plant leads to the formation of a different ester, with different properties. Currently, biodiesel is mainly prepared from soybean in USA, sunflower and rapeseed in Europe and palm in Southeast Asia [8].

In compression-ignition engines, biodiesel is mostly used in diesel blends with different proportions. The international practice led to the adoption of a single nomenclature to identify the concentration of biodiesel in blends, known as the “BX” nomenclature, where X is the percentage on volumetric basis of biodiesel in the blend. For instance, “B20” represents fuel with a concentration of 20% of biodiesel and 80% of pure diesel [8].

Concerning solid and gaseous pollutants, several investigations have been carried out to correlate their emission with the use of biodiesel. Table 3 shows some statistics about the effect of biodiesel on pollutant emissions compared with conventional fuel [18].

Table 3. Statistics of effect of pure biodiesel on engine emissions [18].

Emissions	Number of References	Increase		Similar		Decrease	
		Number	%	Number	%	Number	%
PM	73	7	9,6	2	2,7	64	87,7
NO _x	69	45	65,2	4	5,8	20	29,0
CO	66	7	10,6	2	3,0	57	84,4
HC	57	3	5,3	3	5,3	51	89,5

As it can be observed in [Table 3](#), most of the references disclose a decreasing tendency in PM, CO and HC emissions, when substituting diesel fuel by biodiesel. However, there are still some doubts relatively to NO_x emissions. Some authors observed that these emissions decreased with the percentage of biodiesel [19,20] while others have observed the opposite trend [21,22].

Due to the uncertainty about biodiesel effect on pollutant emissions, numerous studies have been carried out [23-26]. Among them, several works are focused on the impact of particulate matter, especially soot. Considered as one of the major emissions in diesel engines, significant insights into the understanding of soot formation, growth and reactivity are still required. This knowledge is the key to reduce or suppress soot emission.

The notorious reduction of soot emissions when using biodiesel or biodiesel blends instead of conventional diesel fuel, can be mainly explained by the oxygen content of biodiesel. In fact, it promotes a more complete combustion, even in combustion chamber areas with fuel-rich diffusion flames [27-29]. Furthermore, an increase in oxygen content is generally accompanied by an elevated flame temperature and higher particles residence time, which increases soot oxidation during the combustion process [30].

Schmidt and Van Gerpen [31] observed a decrease in aromatic content by blending petroleum diesel with a methyl ester-based biofuel. These aromatic molecules, considered as soot precursors, are absent in biofuels, lowering soot emissions. Results of Flynn *et al.* [32] investigations showed some decrease in the formation of soot precursors when increasing the oxygen content in the fuel. They justified this tendency explaining that large fractions of the fuel carbon were directly converted to CO/CO₂, leading to fewer carbons available for precursors formation.

Mueller *et al.* [33] concluded that oxidation rate of biodiesel soot was up to six times higher than the diesel soot one. They detected on biodiesel soot samples the presence of carbon-oxygen functional groups like C=O, C-O-C or C-OH, which promote soot oxidation. The slower oxidation rate of diesel soot was attributed to the oxidation of the remaining C-C bounds of the carbon atoms within the particles.

2.2 Mechanism of soot formation

Particulate matter consists of a combination of soot (~50%), and other liquid/ solid phase materials. It is classified according to the size (from PM_{2.5} to PM₁₀ for diameter smaller than 2.5µm and 10µm, respectively) and it is divided in ultrafine (<0.1µm), fine (<1µm) and coarse particles (≥ 1µm) [34].

In diesel engines, soot is obtained by a reaction of pyrolysis at elevated temperature and under high pressure (50-100 atm), from incomplete combustion of fuel [35]. In fact, as the reaction zone has a finite thickness and the reaction takes place in a finite amount of time, the combustion is usually incomplete, forming incomplete combustion products, such as soot.

Due of the way that fuel is injected and ignited, soot formation occurs more commonly in diesel than in gasoline engines. Unlike gasoline engines where the fuel/air mixture is ignited with a spark, fuel and air entering the diesel cylinder ignite almost spontaneously from the high pressure in the combustion chamber. The fuel and air mixture in diesel engines typically do not mix as thoroughly as they do in gasoline engines. This creates fuel-dense pockets that produce soot when ignited. Furthermore, fuel used for diesel has compounds with much longer carbon chains than for gasoline, which complicates the occurrence of a complete combustion reaction.

Even though soot production continues to be at the centre of many investigations, its formation is not yet completely understood due to high temperature and pressure conditions, as well as high complexity of fuel composition. Additionally, numerous elemental molecules undergo several simultaneous reactions, which makes the mechanism hardly traceable [36,37]. However, there is sufficient knowledge to assume that the conversion of liquid phase hydrocarbons to soot and finally to gas phase happens in five steps (Figure 3).

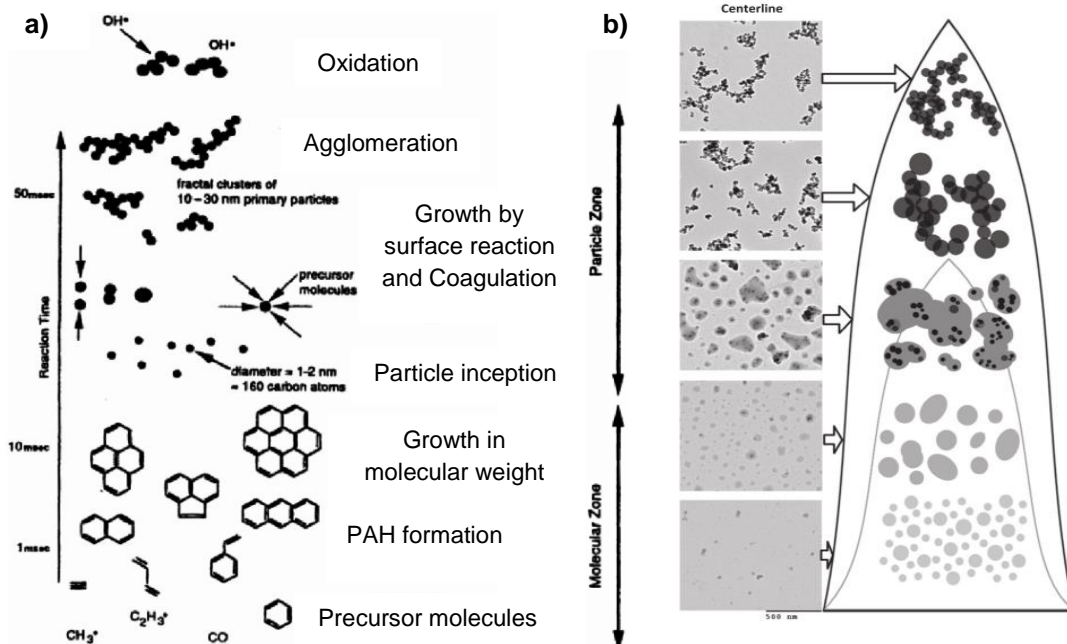


Figure 3. a) Chemical reactions and physical processes involved in soot formation [38].

b) Evolution of soot along the centreline of a co-flow diffusion flame [39].

1. Formation of molecular precursors of soot:

Pyrolysis of fuel leads to the formation of small molecular units, ionic species and radicals (ex.: C_4^* , $C_3H_3^*$, CH_3^*), which grow through reactions of addition and radical recombination. Then, first cycles are formed. They suffer mechanisms entitled HACA (Hydrogen-Abstraction/Carbon-Addition), leading to the formation of polycyclic aromatic hydrocarbons (molecular weight of 500-1000 *a.m.u.*), which are the most probable soot precursors [39,40].

2. Particles nucleation/ inception from heavy PAH molecules:

This step, which corresponds to the transition of a molecular system to a particulate system, occurs in the most reactive zone of the flame and it is promoted by the content in aromatic compounds present in the fuel. It leads to the production of a large number of very small particles, formed from gas phase reactants, via their oxidation and/or pyrolysis products, such as PAHs (polycyclic aromatic hydrocarbons). These soot precursors originate nascent soot particles with a molecular weight of approximately 2000 *a.m.u.* and a diameter in the range of 1,5-2 nm [41-43].

3. Surface growth:

After the formation of nascent soot particles, the mass increases due to the attachment of gas phase hydrocarbons, such as acetylene and PAHs, to the particles surface, with their incorporation into the particulate phase. It leads to a larger soot diameter and an increase of its mass fraction, but the number of particles remains untouched [41,43,44].

4. Coagulation and agglomeration:

Once particles have been formed, they can collide and merge (coagulation). After a certain point, several hundreds of spherical primary particles can agglomerate and form well defined chains. This phenomenon was suggested by Lahaye [45] as the main mechanism for soot formation. This leads to a decrease in the number of particles and an increase in their size, without changing the total mass of soot present. Mature particles are almost spherical with diameters of 50 nm or even larger [41-43].

5. Oxidation:

Carbon or hydrocarbon molecules are oxidized into products of combustion, such as CO and CO₂, decreasing the mass of PAHs and soot. The main oxidizing species are radicals such as OH^{*}, O^{*} and O₂. Particulate emissions from any combustion device depend on the balance between soot formation and oxidation [40].

2.3 Properties of diesel soot

2.3.1 Composition

Diesel soot is found to be in the form of agglomerates. These structures are composed by smaller particles, which are in turn a collection of smaller carbonaceous spherules [46]. These spherules present an onion structure, with an amorphous carbon core and a structured outer shell with graphitic crystallites, parallel to the spherule surface (Figure 4).

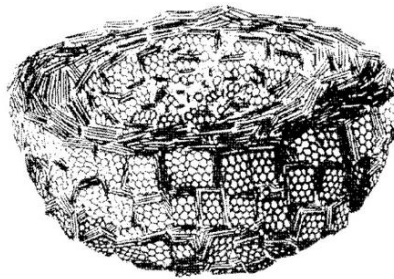


Figure 4. Elemental particle of soot produced in the combustion chamber of a diesel engine [47].

In a macroscopic point of view, each elementary particle can be represented by a carbon sphere (10-50 nm), which is the solid fraction of soot, and where the Soluble Organic Fraction (SOF) is adsorbed and condensed (Figure 5). Globally, aggregates are composed by three fractions. The IOF (Insoluble Organic Fraction) is composed by solid particles, mainly carbon compounds obtained by incomplete combustion inside the diesel engine. SOF results from fuel and/or the lubricating oil that was evaporated and then condensed after the combustion. It consists of unburned hydrocarbons, oxygenated compounds (ketones, esters, aldehydes, ethers...) and PAHs. Sulphate species (SO_2), metallic compounds, vapor phase hydrocarbons, water and nitrogen (from the introduction of nitrogen oxide into the carbonated chains) are also included. Finally, VOF (Volatile Organic Fraction) has the same compounds as SOF but these are vaporized without any thermic transformation [48-50].

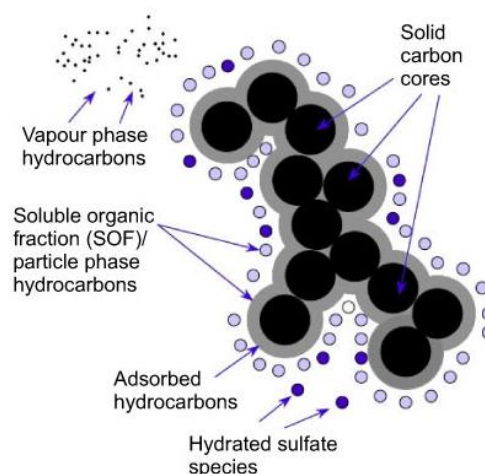


Figure 5. Schematic representation of diesel particulate matter (soot) [51].

2.3.2 Impact of biodiesel on soot nanostructure and reactivity

It is well known that characteristics such as composition, structure and morphology depend on the particles origin and production conditions. In turn, these properties, which are specific for each soot, can affect the aggregates reactivity. Several investigations have been conducted to determine the major factor responsible for the reactivity observed in diesel/biodiesel soot particles. Consequently, it was observed that their reactivity is influenced by the nanostructure.

Concerning soot internal structure, the spectrum of carbonaceous materials goes from graphite, with highly ordered carbons, to an amorphous material, with highly disordered carbons. Graphite is defined as a form of pure carbon consisting of parallel layers of hexagonally arranged carbon atoms in a plane (graphene layers), in a three-dimensional crystalline long-range order [52,53]. On the other hand, amorphous carbon is a material without long-range crystalline order. Graphitised carbons tend to have more orderly stacked crystalline layers and consequently fewer exposed active sites, which are characteristics of amorphous carbon.

Figure 6 demonstrates that reactivity of diesel particulate matter is to be expected somewhere in between graphite and amorphous carbon [54], which can be characterised by the degree of graphitisation.

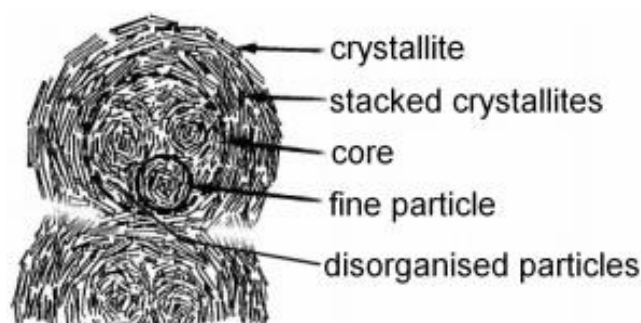


Figure 6. Internal structure of diesel soot [55].

Diverse research [56-58] evidenced the influence of the chemical structure on soot reactivity via number and location of carbon active sites, which seems to be the predominant factor determining the reactivity of carbon material. Indeed, reactivity has been found to be higher on carbon surfaces containing many exposed edge sites [57,59,60]. Carbon atoms in edge sites can form bonds with chemisorbed oxygen due to the availability of unpaired sp^2 electrons [54]. Similarly, Vander Wal and Tomasek [57,61] attributed the loss of reactivity in particles with higher degree of graphitisation to the fact that graphitised carbons have longer graphene layers and, therefore, a lower proportion of atoms in edge positions.

The interplanar spacing, which is defined as the distance between parallel layers, also influences soot reactivity. Liati *et al.* [62] examined, through HR-TEM analysis, primary particles from pure biodiesel (B100) and diesel fuel (B0). They observed that the space between layers was smaller for diesel soot. The increase of distance between layers makes it easier for the combination of oxygen to the edge sites, promoting soot oxidation. Such results prove that particles from biofuel are more prone to be oxidized.

Their investigations also led to the conclusion that soot from B100 have a higher percentage of short graphene layers in comparison with soot obtained by diesel fuel (Figure 7).

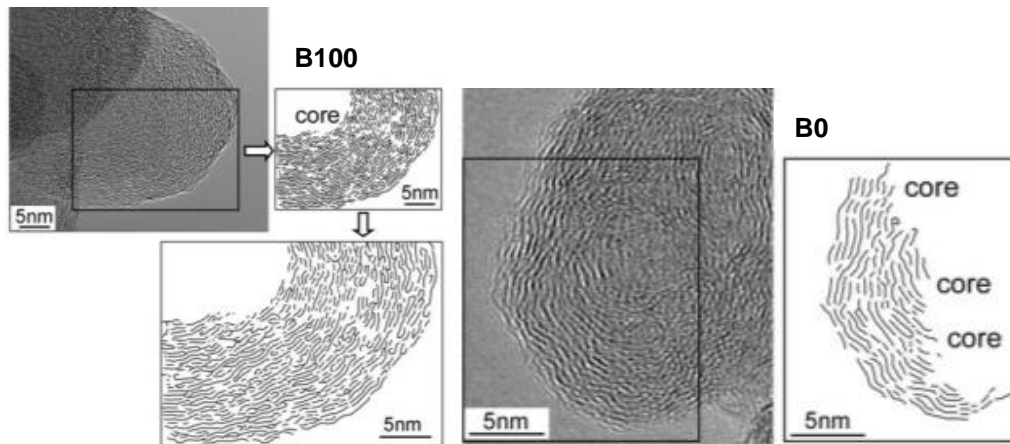


Figure 7. HRTEM images of soot from B100 and B0 [62].

Some researchers studied the impact of oxygenated compounds present in biofuels on soot reactivity. They found that the presence of oxygenated functional groups enhances soot oxidation, which can explain the better reactivity of soot from biofuel [48,60,63].

Barrientos *et al.* [64] studied by thermogravimetric analysis (TGA) and by Raman spectroscopy, model soot produced by the combustion of methyl-esters, n-alkanes, diesel and biodiesel in a non-premixed flame. It was found that ester compounds contained in biodiesel had an impact on soot oxidation reactivity and characteristics. Along the combustion of shorter alkyl chains of methyl esters, soot particles exhibited higher soot oxidation reactivity and lower structural order.

Recently, Ess *et al.* [65] analysed, by Raman spectroscopy, soot provided by B100, B7 and B0. The analysis showed similar spectra for the different samples, which implies that different soot particles have a similar graphitic structure, with exception of B100, which showed a structure slightly more organised. The analyse by temperature programmed oxidation (TPO) demonstrated that B100 presented the best reactivity, though.

It is therefore evident that detailed knowledge of the nature, physical and chemical properties of PM emissions related to the use of bio- and diesel-fuel can contribute to the improvement of engine performance and optimization of the operational characteristics of DPF systems. The results of this study are expected to be useful for improving post-treatment strategies and engine performance. Moreover, they can contribute to a better understanding of the impact of diesel PM on the environment.

2.3.3 Diesel soot oxidation

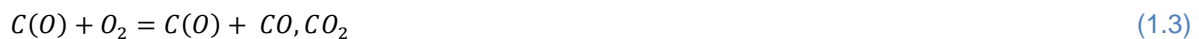
Several components of diesel exhaust gases are relevant for soot oxidation. The most prominent ones are O₂, NO₂, CO, H₂O and HCs due to their affinity for reaction with the particles. However, this work will focus on the strongest oxidizers, namely O₂ and NO₂.

2.3.3.1 Oxidation with oxygen (O₂)

Several studies were carried out to better understand the carbon oxidation mechanism in presence of oxygen [66-70]. Oxygenated complexes were proposed as intermediaries for CO and CO₂ production. In general, the reaction between oxygen and carbonaceous compounds, such as soot particles, occurs in two main steps. Firstly, the oxygen (reactive molecule) is transferred from the reaction gas to the soot surface, where it is adsorbed and form a complex in the solid phase. Subsequently, this complex is decomposed, and an atom of carbon is removed from the surface, leading to CO₂ and CO as products.

According to Haynes *et al.* [68], the soot oxidation mechanism is composed by three steps:

- Reaction between a free carbon site C(-) and O₂, in gaseous phase, to form an oxygenated site C(O) and CO (1.1)
- Production of another free carbon site and CO/CO₂, in gaseous phase, with the formed oxygenated site (1.2)
- The oxygenated site can also react with O₂ and produce an additional site, releasing CO and CO₂ (1.3)



Ahmed *et al.* [69] suggested a mechanism in which stable carbon complexes are produced. In fact, they explained that a free carbon site Cf should react with O₂ and form an adsorbed molecule C(O₂) before formation, at soot surface, of the stable complex (CO)_c (2.1-2.5).



Neef *et al.* [71] and Yezerets *et al.* [72] are among those who proposed the global reactions (3,4):



Different mechanisms are proposed in the literature to explain the reaction between the oxidant and carbonaceous compounds. According to Tighe *et al.* [73], there are two complementary stages. Initially, there is a transitory and fast reaction due to the pyrolysis of SOF before soot exposition to oxygen. The second stage, which is the slowest part of oxidation, is characterized by diffusion of O₂ into the internal pores of the spherules. Yezerets *et al.* [72] proved that any modification in the carbon reactivity could be due to an increase of the specific soot surface during the oxidation process and due to chemical phenomena linked to the complexes formed at the soot surface during adsorption of O₂.

2.3.3.2 Oxidation with nitrogen dioxide (NO₂)

In general, the oxidation mechanism promotes the formation of CO, CO₂ and NO with a concentration that depends on the oxidation temperature [74]. The mechanism of direct interaction between soot carbon and NO₂, established by Jeguirim *et al.* [75], is composed by equations (5.1-5.6). The following mechanism is valuable in the 300-450°C temperature range.



Where $-C^*$ represents an active carbon site. It was proved, by adsorption and desorption of NO₂, that two types of oxygenated complexes are present, $-C(O)$ and $-C(ONO_2)$, which are likely to form at the surface. Then, their decomposition leads to CO₂, CO and NO production. The global reactions of carbon oxidation in presence of NO₂ are (6,7).



Diverse research proved that NO₂ is a more active oxidant than O₂ at low temperatures (<450°C) and that it can react directly on the carbon surface [76-78]. It was also demonstrated that soot oxidation by NO₂ occurs at temperatures close to those from the exhaust of diesel engines (300-400°C). On the opposite, oxidation by O₂ occurs at temperatures higher than 450°C [76,79].

Many attempts were made to understand the effect of each oxidant in soot combustion. Results from high-resolution transmission electron microscopy (HR-TEM), Raman spectroscopy and from the evolution of specific surface area (BET) during the oxidation process, demonstrated that O₂ and NO₂ oxidized soot differently. In fact, molecular oxygen promotes an internal burning-out process. This model, called “core-shrinking model”, consists on the development of micropores on the surface, allowing O₂ to penetrate and oxidize the amorphous core (Figure 8). Consequently, particles show an

empty core and a more ordered crystalline structure in the periphery. On the opposite, NO_2 reacts immediately on soot surface through an external burning process [60].

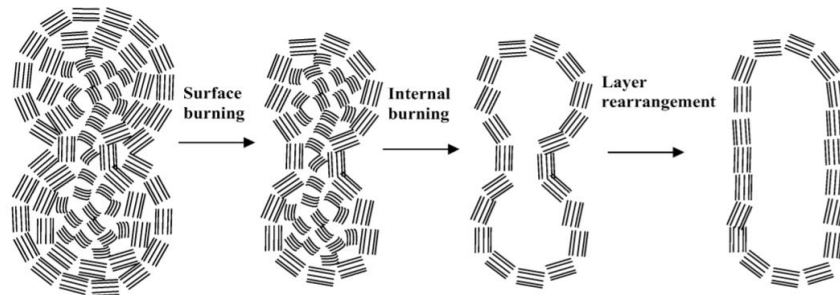


Figure 8. Internal combustion process of B100 soot with O_2 , proposed by Song. et al. [60].

2.4 Exhaust post-treatment system

To meet the increasingly stringent regulations on pollutant emissions, engine development alone is not sufficient. Instead, the combination of optimizing interior combustion and exhaust post-treatment has become the mainstream method for diesel emission control. Therefore, it becomes imperative to obtain a better knowledge about these systems to achieve the maximum of goals and to know which trade-offs must be done.

Nowadays, concerning treatment of gaseous emissions, a Diesel Oxidation Catalyst (DOC) and a Selective Catalytic Reduction (SCR) are commonly used (Figure 9). In the first one, unburned hydrocarbons, CO and volatile organic compounds are transformed into CO_2 and H_2O . It also contributes to the oxidation of NO to NO_2 . On the other hand, SCR reduces NO_x by injecting a liquid reducing agent (namely AdBlue®) into the exhaust stream. The reducing agent is usually urea, which enables a chemical reaction that converts NO_x into nitrogen, water and CO_2 . To manage particulate emissions (PM), a Diesel Particulate Filter (DPF) is adopted (Figure 9).

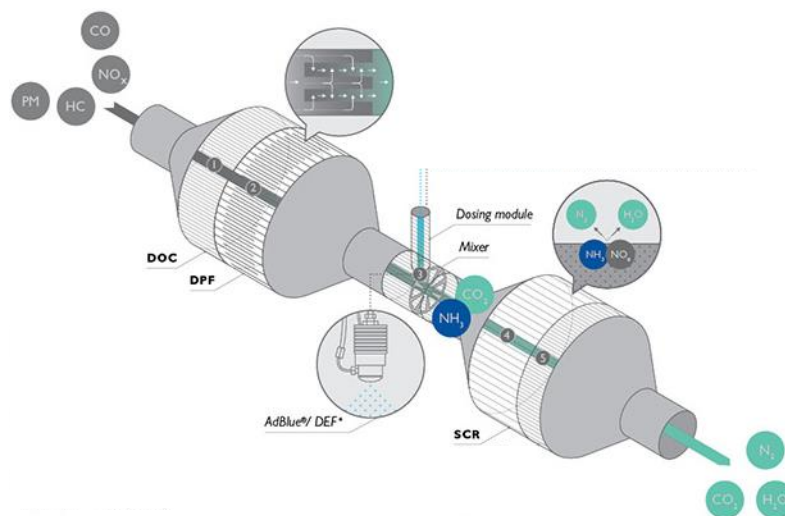


Figure 9. After-treatment system of exhaust emissions [80].

2.4.1 Diesel Particulate Filter (DPF)

Removal of soot from the exhaust stream of diesel engines is a long-standing goal, accomplished by means of different exhaust post-treatment methods. Diesel Particulate Filters have been applied in production vehicles since 2000. Some buses and trucks meeting the *Euro IV, V* and *EEV (Enhanced Environmentally-friendly Vehicle)* emissions standards were equipped with these filters. Now, all *Euro VI* HD vehicles have a DPF meeting the PM mass and particle number emissions requirements. This technology is the current and most efficient solution to reduce this type of emissions, with a filtration efficiency between 70% and 95% of total particulate matter. Higher efficiency, between 95% and 99% is reported in the literature for the solid particulate fraction, which involves elemental carbon and inorganic ash (mainly from trace metals in diesel fuel, engine wear and corrosion) [81].

A DPF is generally made of porous materials, such as Silicon Carbide (SiC) or cordierite (2MgO , $2\text{Al}_2\text{O}_3$, 5SiO_2) (Figure 10.a). These supports are currently used due to their low thermic dilatation coefficient and good resistance to high temperatures (1100°C) [82]. Among the different available configurations, *wall-flow* type filters (Figure 10.b) are the most common ones. They are honeycomb monoliths with parallel channels plugged alternatively at each end to force the exhaust gas to flow through the porous filter wall, where soot is retained (soot cake) [81-84].

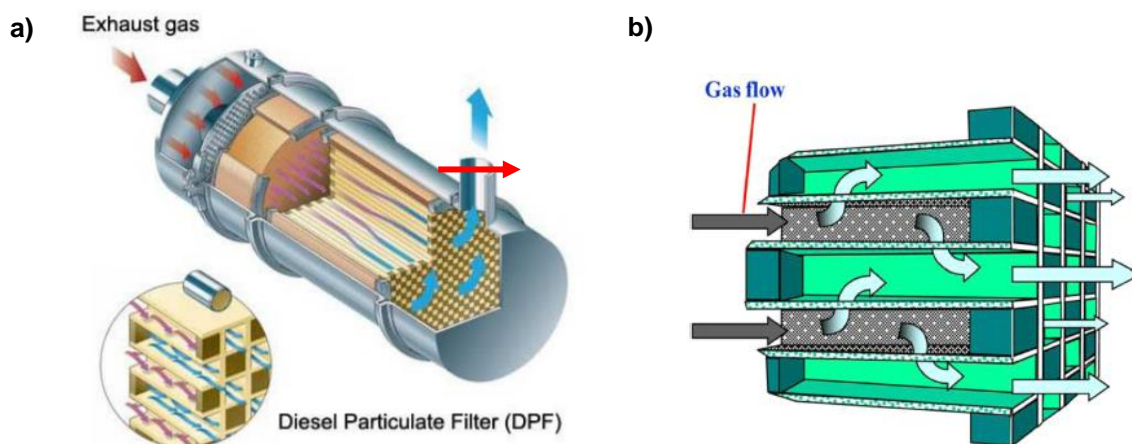


Figure 10. a) Cordierite honeycomb ceramic [85]. b) Schematic view of a wall-flow filter [81].

As the accumulated soot in the filter increases, the back pressure also increases, and it will progressively originate a decrease of engine power, penalizing the fuel consumption. In the end, the engine can stop if the soot is not frequently or constantly removed by combustion reactions. To restore the filter efficiency, it must be cleaned through a regeneration process, burning the particles [86-88]. Diesel particulate spontaneously burns in air at high temperatures ($500\text{-}600^\circ\text{C}$), in the diesel exhaust gas, and converts carbon and oxygen into CO and CO_2 with a significant rate. These conditions are required because of the high activation energy (E_a) for the direct oxidation of soot by oxygen ($100\text{-}210$ kJ/mol). Unfortunately, this temperature range is not regularly achieved in typical diesel vehicle applications for sufficient periods of time to enable self-regeneration. Usually, the exhaust temperature, during normal driving conditions, are in the $150^\circ\text{C}\text{-}240^\circ\text{C}$ range [84]. To overcome this limitation, two solutions are presented:

- **Thermic regeneration:** The exhaust gas temperature is raised up to the point that soot oxidation can be self-sustained in the filter until fast enough rates by external heating strategies: electric heating, additional burners, recirculation of the exhaust gas... Such approaches incur additional energy costs (high-energy consumption). In some cases, it can lead to sufficiently high local temperature excursions that might damage the DPF.
- **Catalytic regeneration:** The ignition temperature of accumulated soot is decreased with the impregnation of catalysts on the internal channels of the DPF. These catalysts can be permanently located inside the filter or periodically introduced injecting fuel in the exhaust.

2.4.1.1 Continuously Regeneration Trap (CRT) – Passive Regeneration

Particulate oxidation by NO₂ from diesel exhaust was first reported by Cooper and Thoss [89]. They reached the conclusion that nitrogen dioxide oxidized particles of soot more easily than the oxygen. However, it is difficult to achieve an optimal usage of NO₂ during DPF regeneration because of the lower emissions of this gas in modern engine combustion modes. Consequently, to obtain high enough reaction rates to consume considerable amounts of soot, the concentration of NO₂ must be increased by placing a DOC upstream of the particulate filter. This configuration, which is named CRT (*Continuously Regenerating Trap*), was developed and patented by Johnson Matthey [90]. This system showed an excellent performance in reducing the amounts of CO, HC and PM during a road test over 700 000 km in the presence of ultra-low sulphur diesel fuel [90]. Nitrogen dioxide emissions are used to continuously oxidize the particles deposited inside the filter at much lower temperatures than by O₂. CRT is made up of two parts [89]:

1. A DOC upstream of the filter is coated with a platinum-based catalyst (ex.: Pt/Al₂O₃) to induce the catalytic oxidation of NO into NO₂ (8), which becomes crucial nowadays for SCR systems, and of course the total oxidation of CO and unburned hydrocarbons to CO₂ (9) and to CO₂ and water (10), respectively.



2. A wall-flow filter (DPF) lets the exhaust gases pass through the pores, while soot is trapped inside the channels. Then, particles are removed by the NO₂ produced in the first chamber (11).



Despite many benefits, the system has also some restrictions. Andersson *et al.* [91] found that at temperatures of 300°C or below, the NO₂-particulate reactivity is very low, and even when NO₂

concentrations are increased, the oxidation rate is not still capable of being increased. To have a higher oxidation rate, the temperature needs to be at least greater than 300°C, which does not occur in normal driving conditions. Furthermore, the fuel can't have any trace of sulphur because it contributes to the inhibition of the catalyst activity. The catalyst can oxidize sulphur-dioxide (SO₂) present in the exhaust to sulphur-trioxide (SO₃) (12), which can be absorbed by the particles surface or combine with water vapour to produce sulfuric acid (H₂SO₄) (13). Formation of H₂SO₄ is undesirable due to its adverse impact on health, increase of nuclei-mode particles and total PM downstream of the DOC. Moreover, oxidation of SO₂ to SO₃ involves the use of catalytic sites, which decreases their availability for oxidation of HCs, CO and NO. Finally, as the time of the regeneration is relatively important, the technology is mainly used by HD engines, which are better adapted due to their working conditions (high load).



2.4.1.2 Active Regeneration

Sometimes the exhaust gas temperature can drop to a point where continuous regeneration can no longer be completely guaranteed. In this case, active regeneration is required.

To avoid the DPF to overload when operating for a long time, introduction of an additional thermal energy is required. This procedure can be performed by injecting fuel into the combustion chamber in one or more post injection sequences or by injecting fuel directly into the exhaust system. Through a thermic and periodic regeneration (~ each 850 km), the heat release is enough to raise the exhaust temperature of the particulate filter around 600°C. As a result, the deposited diesel soot oxidizes with the surplus oxygen present in the exhaust gas (14,15). The major disadvantage of this method is the necessity to evaluate the total soot load in the DPF at its conception time, to determine the regeneration frequency [92]. In general, it is always desirable to maximize the amount of passive regeneration that can be achieved since passive regeneration doesn't require additional energy.



2.4.1.3 DPF regeneration with additives

On May 2000, PSA Peugeot Citroën introduced additives in the DPF of high quality cars (607 Diesel 2,2L HDI) [92]. This type of technology is based on a catalytic regeneration with the combination of two strategies. It occurs each 1000 km and last just some minutes. However, an additional reservoir is needed in the vehicle for the additive.

1. Increase of the exhaust temperature in two steps: Firstly, a fuel post-combustion occurs, which rises the temperature from 200°C to 250°C. Then, HCs and CO are burned with an oxidation catalyst installed upstream the filter, which allows an additional increase of approximately 100°C.

2. Decrease of the activation energy of soot with the introduction of a catalyst (Eolys®, cerium-based additive) directly in the fuel. The natural combustion temperature of soot is lowered to 450°C.

2.4.1.4 Catalytic DPF

It is difficult to ensure that the soot collected in the DPF is completely burned at the low exhaust temperature. On the other hand, soot combustion at high temperature (>500°C) can lead to a large energy consumption [93-95]. Thus, the advanced catalysts [96-98] coated on DPF have been widely investigated to decrease the temperature of soot combustion [99,100]. A literature review finds that global activation energy values for catalytic combustion by O₂ are comprised between 13 and 209 kJ/mol, compared to the 100-210 kJ/mol for the non-catalytic reaction [101]. That means that much lower values of *E_a* are possible with a catalyst.

Many catalysts have been reported for soot oxidation [94,95,97]. Even if noble metal-based (ex.: Pt) catalyst exhibits higher activity in comparison to oxide catalysts, they are more expensive, and their thermal stability is not satisfactory even at low temperatures [102-104]. Consequently, use of oxide catalysts represents a more reasonable alternative. Among the tested single oxides in combustion, CeO₂ is one of the most studied. Ceria oxide exhibits excellent catalytic activities due to its special oxygen storage capacity [105,106]. It is able to store and release active oxygen species. This property of CeO₂ makes it highly effective in catalytic applications. On the other hand, manganese oxide also has been used in oxidation reactions due to its strong oxidative property. The high activity of Mn is attributed to the element's multivalent oxidation states (mainly Mn²⁺, Mn³⁺ and Mn⁴⁺) and to the high mobility of lattice oxygen. Therefore, catalysts containing such elements as manganese and cerium belong to the most promising ones [107-109].

Compared with pure CeO₂ and MnO_x, MnO_x-CeO₂ catalyst has showed higher efficiency owing to the strong synergetic effect between the bimetal oxides in the solid solution. The soot oxidation temperatures are much lower, and the oxidation rates are significantly higher on the mixed oxides than on the individual oxides. Tikhomirov *et al.* [110] observed that the MnO_x-CeO₂ mixed oxides with the Mn:Ce ratio of 1:3 exhibited a high activity for NO-assisted soot oxidation. This can be explained by the ability to store NO at low temperature in form of nitrates, followed by a release of NO₂ as a strong oxidizing agent, through the decomposition of those nitrates. In his investigation, Setiabudi [111] found that the decomposition of nitrates resulted in not only the production of NO₂ but also in the desorption of active oxygen during CeO₂ catalysed soot oxidation, which played a key role on the promotion of soot oxidation. [Figure 11](#) shows the soot combustion mechanism in presence of Ce-based catalysts.

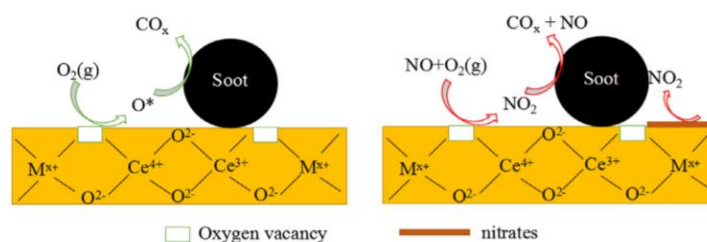


Figure 11. Schematic representation of the soot combustion mechanism of the Ce-based catalysts. a) active oxygen mechanism. b) NO_2 -assisted mechanism [112].

It was proved that the incorporation of Mn into the ceria lattice accelerated the active oxygen mobility and promoted soot oxidation. In fact, Mn is introduced into the CeO_2 lattice, replacing Ce ion. Thus, it causes the relocation of adjacent oxygen anion from its lattice position to an interstitial position, leaving a vacancy behind. Then, Mn^{n+} is reduced to $\text{Mn}^{(n-1)+}$ through the transfer of an electron from the interstitial oxygen. Due to the loss of one electron, the unstable interstitial oxygen escapes from the lattice and becomes an active oxygen (O^*). The escaped active oxygen will act on soot oxidation. Then, Ce^{4+} captures one electron from $\text{Mn}^{(n-1)+}$, leading to the formation of Ce^{3+} and Mn^{n+} . Finally, gas phase O_2 molecules act as oxygen storage cavern to supplement the consumed active oxygen, to re-oxidize the catalyst and guarantee the metal ions reduction-oxidation reaction cycle. Ce^{3+} is also oxidized to Ce^{4+} , back to the original chemical state [104] (Figure12).

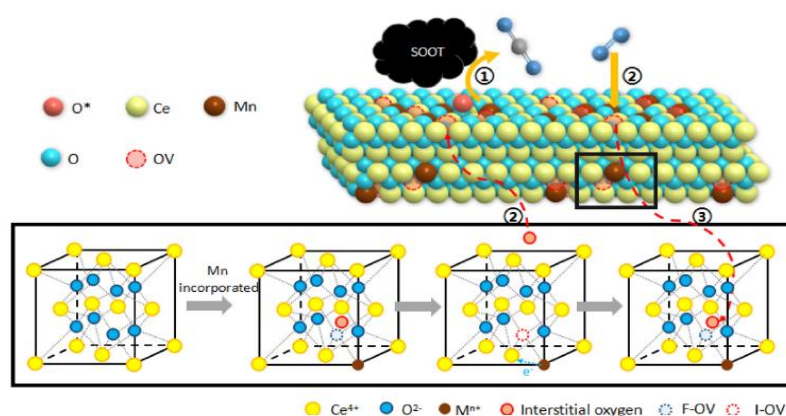


Figure 12. Introduction of Mn in the CeO_2 lattice and evolution of oxygen vacancies in soot oxidation [107].

In catalytic studies, particles of soot are usually physically mixed with a catalyst. The catalytic soot oxidation occurs at the soot-catalytic interface and the rate strongly depends on the intensity of contact between soot and catalyst. In turn, the type of contact depends on how the mixture is prepared. The main types of physical contact used are “loose” and “tight” contact. Mixing soot and catalyst powders with a spatula is defined as “loose” contact, while “tight” contact means that the powders are mixed in a mortar or through ball milling. It is well known that a soot-catalyst mixture obtained by “tight” contact shows lower activation energy and oxidation temperature than by “loose” contact due to the higher number of contact sites. Thus, the impact of the soot-catalyst contact on soot oxidation and therefore, on DPF regeneration, should be studied.

THIS PAGE WAS INTENTIONALLY LEFT BLANK

3 Experimental methodology

In the present study, different soot samples were analysed through different characterization techniques. Their size, composition and structure were determined and then correlated with particles oxidative reactivity, in presence or not of a catalyst. This approach also had the objective to demonstrate the similarity between “model” and “real” soot properties, which were generated in two different ways.

3.1 Soot generation

“Model” soot was produced through incomplete combustion in a previous work [113], in non-premixed diffusion flames over an axisymmetric co-flow burner (*Santoro burner* [114-116]) at atmospheric pressure. In this burner, the carrier gas was diluted with nitrogen (33,33% CH₄ (purity > 99,995%) / 66,67% N₂ (purity = 99,999%)) and then, it was doped with vapours of different surrogates (*Figure 13*). Soot particles were collected in the post-flame region on an isolated glass microfibre filter.

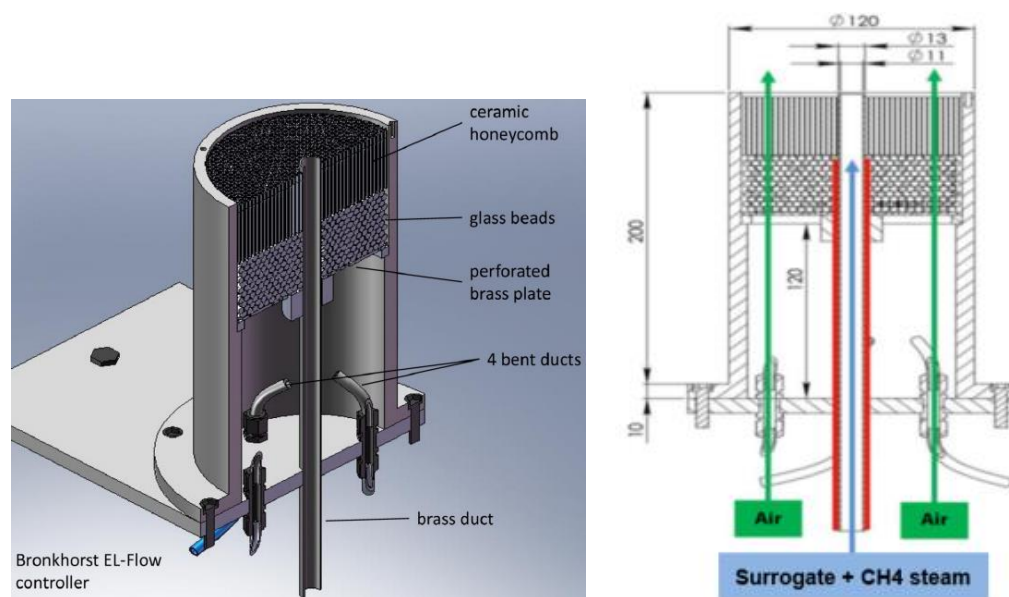


Figure 13. Configuration of the burner to establish a non-premixed flame as described by Santoro et al. [117].

Due to the complexity of diesel composition, a diesel surrogate «Aref», consisting of a binary mixture of 70% (mole%) of n-decan and 30% of α -methyl-naphthalene (α -MN), was used to produce “model” diesel soot. This surrogate was already used in many studies to simulate combustion in diesel engines and was tested to reproduce the soot formation process during the combustion of commercial diesel [118-120]. “Model” biodiesel was prepared by adding oxygenated additives to the reference surrogate «Aref», namely methyl butanoate (C₅H₁₀O₂), methyl octanoate (C₉H₁₈O₂) and methyl decanoate (C₁₁H₂₂O₂), in two different proportions (7 and 30 mole%). Obtained surrogates were named «MB7», «MB30», «MO7», «MO30», «MD7» and «MD30», respectively.

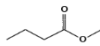
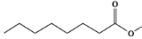
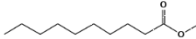
Simple compounds of high purity were used to produce biodiesel surrogates, which are representative of real biodiesel, to better understand the different factors affecting biodiesel combustion in diesel engines and consequently, their soot emission and reactivity.

Table 4 shows the produced surrogates with their correspondent chemical composition, while Table 5 exhibits the chemical formula and structure of the studied methyl ester-based additives that have been selected to formulate three types of biodiesel surrogate mixtures.

Table 4. Composition of diesel and biodiesel surrogates [113].

Surrogates	Composition (mole%)	Additive content (mole%)
Aref	70% n-decan + 30% α -methylnaphthalene	-
MB	Aref + methyl butanoate	
MO	Aref + methyl octanoate	7% and 30%
MD	Aref + methyl decanoate	

Table 5. Chemical formula and structure of methyl ester-based additives used for biodiesel surrogates [113].

Methyl ester	Chemical formula	Structure
Methyl butanoate	$C_5H_{10}O_2$	
Methyl octanoate	$C_9H_{18}O_2$	
Methyl decanoate	$C_{11}H_{22}O_2$	

“Real” soot was provided by Renault-Volvo Trucks. They were removed from the exhaust of an engine bench, blowing them out from the particulate filter with a pneumatic blower FSX[®] (*Trap Blaster*TM 7). Then, they were collected in a vacuum bag (~2/3 in mass of the total particles). The DPF was placed downstream of a Diesel Oxidation Catalyst (DOC) to ensure the removal of adsorbed hydrocarbons.

The system worked with a low loading cycle operating at low temperatures, which is representative of very severe cold real drive cycles. During this cycle, temperature of exhaust gases upstream the filter was 160°C. Particles of soot (B7-BM and B100-BM) were produced by combustion of fuel with 7% and 100% (volume), respectively, of methyl ester from rapeseed oil. The used diesel fuel was a standard Euro VI fuel (EN 590).

3.2 Laser particle size analysis

The size of particles emitted by the exhaust has different impacts on the environment and health. Furthermore, their influence on the post-treatment system performance, particularly on the DPF, has been demonstrated [121,122]. Since soot has different granulometries, laser diffraction spectroscopy is a useful tool to measure the size distribution of such particles [123,124].

Measurement of particle size distribution of soot aggregates was carried out fully automatically by a *ANALYSETTE22 FRITSCCH NanoTec*, under wet dispersion in which water was used as a suitable liquid. In this equipment, the sample is continuously recirculated and dispersed in a close circulatory system unit. For the support of the dispersion process, an integrated ultrasonic generator is used, and the intensity is adjustable via operating software (*MaS™ control*). The agglomerates are readily disaggregated into individual particles as far as possible by treatment in an ultrasound bath. The measurement is automatically launched since the quantity of soot is enough to have a value of adsorbed beam between 7% and 15%.

The total measuring range of 0,01-2100 μm can be detected without converting the optical elements: the distance between the detector and the measuring cell, which contains the sample particles, is adjusted automatically. For the smaller particles, the measuring cell is located only a few millimetres away from the detector whereas the coarse range is measured with a large distance from the measuring cell to the detector (Figure 14).

This type of analysis is based on the physical effect of diffusion and diffraction of electromagnetic waves by the particles. An infrared laser ($\lambda = 532 \text{ nm}$) is responsible for picking up the scattered light with a small scattering angle, and thus for measuring large particles (Figure 14.a). The measurement of smallest particles down into the nano-range is performed by a green laser ($\lambda = 850 \text{ nm}$) light for backward scattering (Figure 14.b).

Before each experiment, a sample was prepared to ensure a complete dispersion of the particles. Therefore, some milligrams of soot were mixed with a few drops of surfactant (*Dusazin 901*). Then, the mixture was diluted in water until complete dissolution.

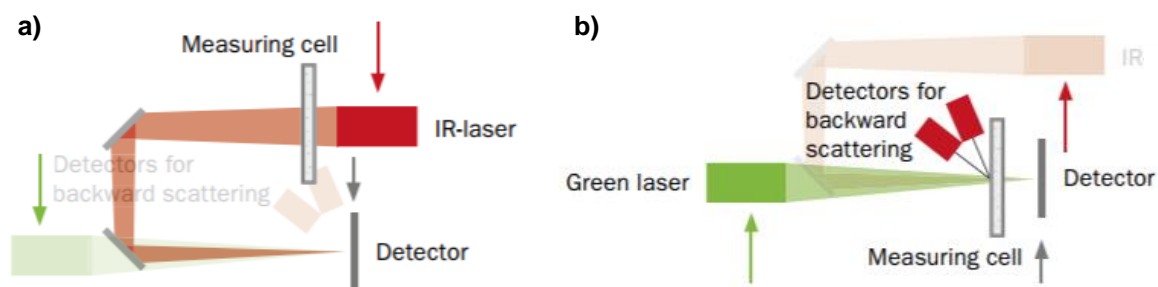


Figure 14. Optical structure of the *ANALYSETTE 22 FRITSCCH NanoTec*. a) IR laser active.
b) Green laser active.

3.3 Elemental Analysis: CHNS/O

This analysis was performed by the *Centre Commun de Mesures (CCM)* of Dunkerque, with a *Thermo Fisher Scientific Flash 2000* analyser (Figure 15). The elemental composition of soot samples was determined in terms of organic compounds: carbon (C), hydrogen (H), nitrogen (N), sulfur (S) and oxygen (O). For the CHNS analysis, samples were weighed in a tin capsule and introduced into the combustion reactor (950-1000°C) via a *Thermo Scientific MAS 200R Autosampler*. The resulted gases (CO₂, H₂O, N₂ and SO₂, respectively) were separated by a chromatographic column (GC) and detected by a thermal conductivity detector (TCD). The analytical method is based on the complete and instantaneous oxidation of the sample by “dynamic flash combustion”, which converts all substances into combustion products. For oxygen determination, the sample was weighed in a silver capsule and the system operated in pyrolysis mode. The reactor contained nickel coated carbon and was maintained at 1060°C. The oxygen present in the sample, combined with the carbon, formed carbon monoxide which was then separated from other products and detected.

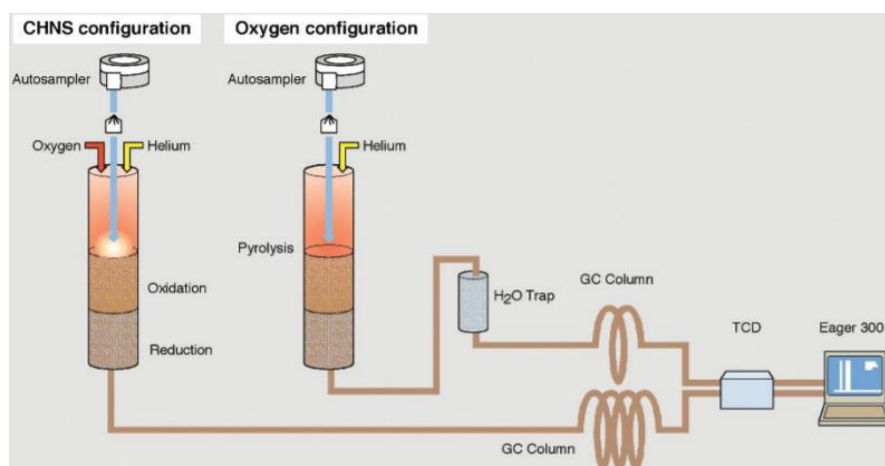


Figure 15. Layout for CHNS/O determination [125].

3.4 Thermogravimetric Analysis (TGA)

Thermogravimetric analysis is a thermic analysis technique, which consists on measuring the variation of mass of a sample in function of the temperature. An alumina crucible with a weighted amount of sample (~5 mg) was placed in a thermo-balance (*TA TGA Q500*) and heated until a targeted temperature with a 5°C/min ramp, under a gaseous mixture with a predefined concentration.

In order to measure the ash content in the soot samples, some tests were performed under air with a heating ramp up to 700°C. For the water as well as volatile and adsorbed organic compounds, an inert atmosphere (N₂) and a heating ramp up to 400°C were used.

The mass loss observed at temperatures lower than 110°C was assumed to be due to desorption of water and poorly chemisorbed compounds. This analysis was done by the Haute Alsace University.

3.5 Raman Spectroscopy

Raman spectroscopy is a technique based on inelastic scattering of monochromatic light from a laser source. Inelastic scattering means that the frequency of photons in the monochromatic light changes upon interaction with a sample. They are absorbed by the sample and then reemitted. Frequency of the reemitted photons is shifted up or down in comparison with original monochromatic frequency, which is called the Raman effect. This shift provides information about vibrational and other low frequency transitions in molecules.

The Raman effect is based on molecular deformations in electric field E determined by molecular polarizability α . The laser beam can be considered as an oscillating electromagnetic wave with electrical vector E . Upon interaction with the sample it induces electric dipole moment $P=\alpha E$, which deforms the molecules. Thus, molecules start vibrating with characteristic frequency ν_m . The monochromatic laser light with frequency ν_0 excites molecules and transforms them into oscillating dipoles. Such oscillating dipoles emit light of three different frequencies (Figure 16) when:

- A molecule with no Raman-active modes absorbs a photon with the frequency ν_0 . The excited molecule returns to the same basic vibrational state and emits light with the same frequency ν_0 as an excitation source. This type of interaction, which is the most common, is called an elastic Rayleigh scattering.
- Due to some interaction with the matter, photon with frequency ν_0 can be absorbed by Raman-active molecule which at the time of interaction is in the basic vibrational state. Part of the photon's energy is transferred to the Raman-active mode with frequency ν_m and the resulting frequency of scattered light is reduced to $\nu_0 - \nu_m$. This Raman frequency is called Stokes frequency.
- A photon with frequency ν_0 is absorbed by a Raman-active molecule, which at the time of interaction is already in the excited vibrational state. Excessive energy of excited Raman active mode is released, the molecule returns to the basic vibrational state and the resulting frequency of scattered light goes up to $\nu_0 + \nu_m$. This Raman frequency is called Anti-Stokes frequency.

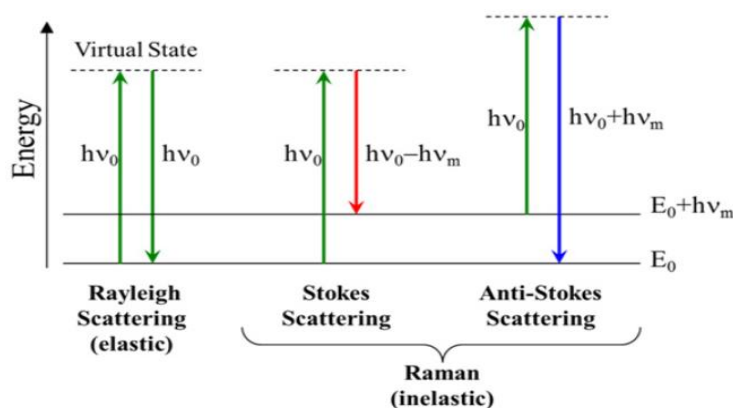


Figure 16. Jablonski Diagram representing the working principle of Raman spectroscopy [126].

Stokes shifted Raman bands involve the transition from lower to higher energy vibrational levels and therefore, they are more intense than Anti-Stokes bands and hence are measured in Raman spectroscopy. The obtained spectrum is presented as an intensity-versus-wavelength shift.

Raman spectroscopy can be applied to get detailed information about the reactivity of soot by determining the structure. This technique is sensible to molecular structures and to crystalline ones, allowing to find the structural order and graphitisation degree of soot. In this work, a quantitative spectral analysis was obtained through the five curves deconvolution model, proposed by Sadezky *et al.* [52]. This technique is based on the combination of four Lorentzian-shaped, G, D1, D2 and D4, bands at about 1580, 1350, 1620 and 1200 cm^{-1} , respectively, and one Gaussian-shaped D3 band at about 1500 cm^{-1} [127,128]. Figure 17 shows an example of Raman spectrum for a *EURO IV* soot, with the combination of the five bands and their adjustment.

- The G band is attributed to ideal graphitic lattice. The intensity of this band is related to the abundance of crystalline components.
- The D1 band arises from carbon atoms of a graphene layer in immediate vicinity of a lattice disturbance. It is associated with a vibration mode involving graphene layer edges.
- The D2 band is attributed to a vibration mode involving surface graphene layers.
- The D3 band is associated to the amorphous carbon content of soot (organic molecules, fragments, functional groups).
- The D4 band is assigned to vibration of disordered graphite lattices, sp^2 - and sp^3 - hybridized carbon bonds, C-C and C=C stretching vibrations of polyenes, and ionic impurities.

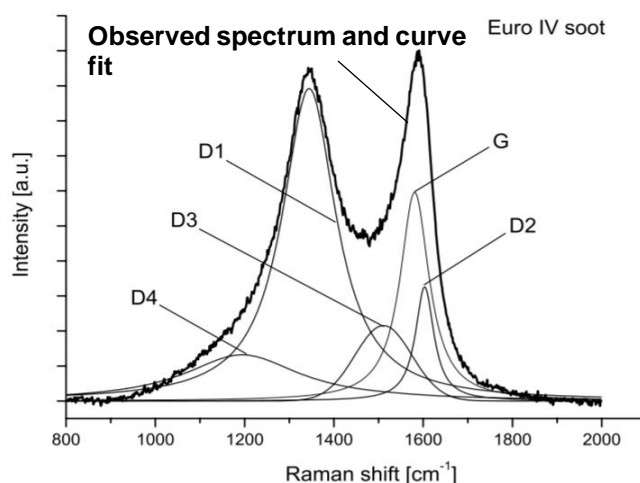


Figure 17. Example of the decomposition of a Raman Spectre ($\lambda_0=514 \text{ nm}$) of untreated *EURO VI* soot, in five Lorentzian bands [129].

The analysis and curve fitting were carried out by the solid characterization service of Carboquímica (Spain). Raman spectroscopy measurements were performed with a Raman Microsystem (*Horbina Jobin Yvon HR 800 UV*), operating with a green sourced laser excitation at 532 nm. The output power was fixed at 0,1 mW in the scanning range of 800-3500 cm^{-1} . The spectrometer included a grating with 600 $\text{grooves}\cdot\text{mm}^{-1}$ and a CCD detector with 50 \times magnification objective lens. To improve the confidence interval, 15 measures of the spectrum were done for “model” soot, and 10 for the “real” one.

3.6 Transmission Electron Microscopy (TEM)

A transmission electron microscope is a versatile analytical microscope for material characterization, providing valuable information about the morphology, aggregate form and internal structure of particles and materials. This type of microscopy uses electrons, which have much smaller wavelength than visible light, allowing the microscope to achieve a high resolution.

In TEM, electrons are produced at the top of the microscope and travel through vacuum in the column. Electromagnetic lenses are used to focus the electrons into a monochromatic beam of electrons, which is accelerated and transmitted through an extremely thin sample. Then, the beam interacts with the material when passing through it. Once the sample is crossed by the electron beam, some of the electrons are scattered and disappear from the beam. At the bottom of the microscope, the unscattered electrons hit a fluorescent screen, which will produce an image. The formation of these images can be explained by the diagram in [Figure 18.a](#).

The magnification depends on the adsorption of the electrons, which is primarily due to the thickness or composition of the material. Denser areas and areas containing heavier elements scatter more electrons and the respective image appears darker.

In order to obtain information about the internal structure of soot particles, a tungsten-filament 100kV transmission electron microscope (*JEOL JEM 100CX*), with a point resolution of 3 Å, was used to make high resolution bright field images ([Figure 18.b](#)). The images were acquired under 500,000 × magnification.

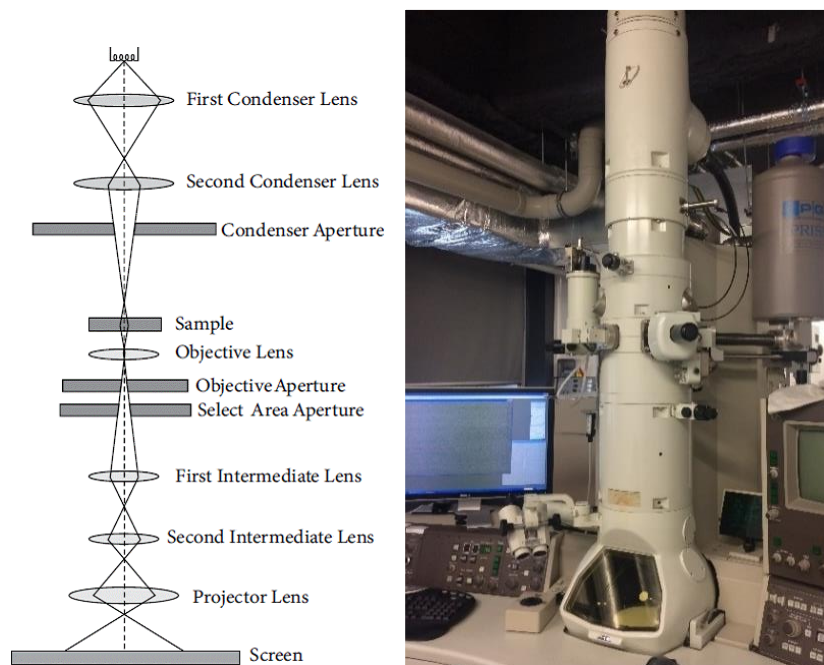


Figure 18. a) Diagram of the optical electron beam in a TEM microscope [130]. b) JEOL JEM 100CX transmission electron microscope.

The HR-TEM results were treated on *Image J*® (a free Java-based software), allowing the measurement of carbon fringes (projection of graphitic layer planes) length as well as the distance between parallel carbon planes. This software consists on several operations and transformations to optimize the images contrast and to facilitate TEM images observation (Appendix A).

3.7 Temperature Programmed Oxidation (TPO)

Soot reactivity was studied by performing temperature programmed oxidation experiments under different reaction gases:

- A mixture of 9% by volume O₂ diluted in argon
- A mixture of 400 ppmv of NO₂ and 9% by volume O₂ diluted in argon

3.7.1 Non-catalytic oxidation

After weighing the samples (2mg of soot + 80 mg of SiC), TPO experiments were performed in a U-shaped quartz reactor (internal diameter 8 mm) as shown in Figure 19.a, forming a fixed bed with a depth of approximately 2 mm, on a porous frit. Each sample was placed in the reactor and heated by a thermally isolated furnace (Figure 19.b) from room temperature until 800°C, with a 10°C/min ramp. The temperature was monitored by a K-type thermocouple located in a thermowell centred in the particle bed. The temperature program was regulated by a *EUROTHERM 2404* heating controller. Total flow rate through the reactor was maintained at 15 l/h by calibrated *Brooks 5850TR* mass flow controllers. Concentrations of CO and CO₂ (ppmv) present in the outlet gas stream were measured by an *Ultramat 6* analyser.

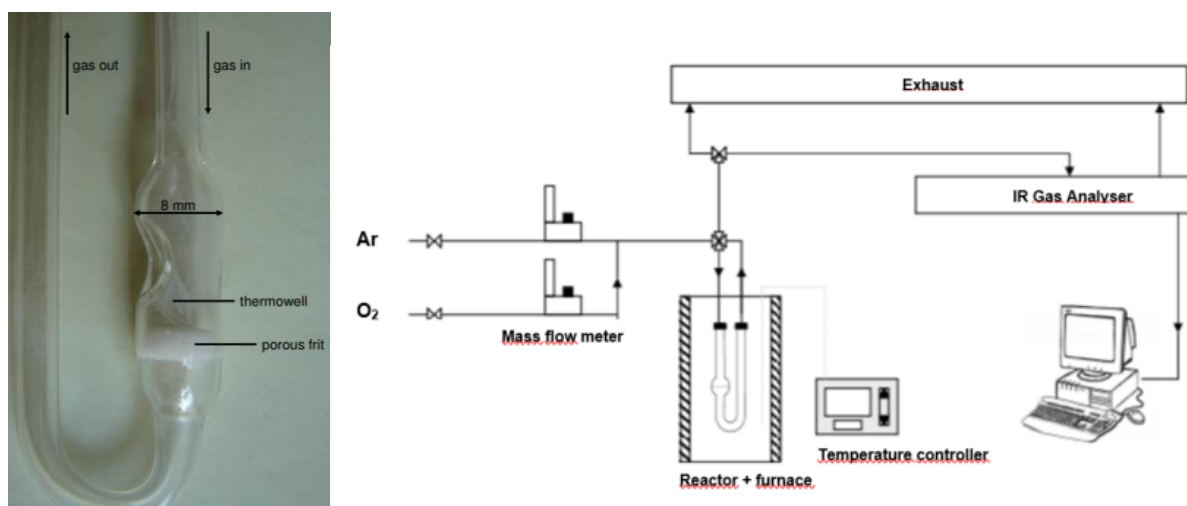


Figure 19. a) Quartz reactor. b) Installation diagram for TPO experiments under 9% O₂/Ar.

The aim of this analysis was to compare the oxidation behaviour of different “model” soot samples with “real” soot, in order to establish a reactivity order in function of the maximal oxidation temperature (T_m), which corresponds to the temperature of maximal CO and CO₂ emission [131]. Additionally, T_{10} , T_{50} and T_{90} were also determined. These values are the temperatures at which 10, 50 and 90% of carbon soot conversion is reached (Appendix B). Finally, ΔT was calculated ($\Delta T = T_{90} - T_{10}$), which means the oxidation interval between 10 and 90% of carbon conversion.

For each experiment, the carbon specific oxidation rate was normalized to the mass of soot initially introduced in the reactor (V_{spec} in mg/(s.g_{in})) and was calculated with CO and CO₂ emissions (X_{CO} and X_{CO_2} in ppmv) through equation (16). Moreover, the selectivity of CO₂ (S_{CO_2} in %) in soot oxidation was obtained through equation (17).

$$V_{spec} = \frac{(X_{CO} + X_{CO_2}) \times D \times M_C}{10^6 \times 3600 \times V_M \times m_{C,in}} \quad (16)$$

$$S_{CO_2} = \frac{X_{CO_2}}{X_{CO} + X_{CO_2}} \times 100 \quad (17)$$

Where X_{CO} : CO molar fraction (ppmv)

X_{CO_2} : CO₂ molar fraction (ppmv)

D : Flow rate (L/h)

M_C : Carbon molar mass (mg/mol)

V_M : Molar volume = 22,4 L/mol

$m_{C,in}$: initial mass of soot introduced in the reactor (g)

3.7.2 Catalytic oxidation

In an attempt to understand the interaction between soot and catalysts and its impact on particles reactivity, TPO experiments were carried out with MnO_x-CeO₂ mixed oxides (1:4 Mn/Ce molar ratio), which were synthesized via a co-precipitation method in a previous work [132,133]. Ce(NO₃)₃·6H₂O (solid, 95% pure) and Mn(NO₃)₂ (liquid, 50 wt.%) as the precursors were firstly dissolved in deionized water, then the dispersants PVA (*polyvinyl alcohol*) and PEG (*polyethylene glycol*) were added. Finally, the solution was mixed with the precipitant (pH>9,0) consisting of NH₃·H₂O and (NH₄)₂CO₃ (chemical reagents, Beijing). The obtained precipitants were filtered and dried by a spraying apparatus, then calcinated in static air at 500°C for 3h in a muffle furnace.

For temperature programmed oxidation experiments, soot and MnO_x-CeO₂ catalyst powder were mixed with a weight ratio of 1/10 (2,0 mg/20 mg) by “loose” and “tight” contact. The “loose” contact sample was obtained by mixing the solids with a spatula for 2 minutes. The “tight contact” sample was prepared with a pestle in an agate mortar grinding for 2 minutes too. To minimize the impact of hot spots and to prevent reaction runaway, the soot-catalyst mixture was diluted with 80 mg of SiC powder.

A third type of contact was tested to have an intermediate effect on soot oxidation, between “loose” and “tight” contact. Therefore, the sample was prepared with the same soot/catalyst ratio via using a spatula grinding for 2 minutes and loading about 60 bar pressure in a pneumatic press.

The TPO conditions were the same as for non-catalytic oxidation. For each experiment, the carbon specific oxidation rate was normalized to the mass of soot initially introduced (V_{spec} in $\text{mg}/(\text{s}\cdot\text{g}_{\text{in}})$) and was calculated with CO and CO₂ emissions (X_{CO} and X_{CO_2} in ppmv) through equation (16). T_m , T_{10} , T_{50} , T_{90} and ΔT were also determined, as well as the selectivity of CO₂ (η_{CO_2} in %) in soot oxidation.

4 Results and discussion

In this chapter, the effect of addition of oxygenated compounds in a diesel surrogate, on soot properties and oxidative reactivity is evaluated. Different structures of ester molecules with different concentrations are tested. Particles, called “model” soot, generated through the incomplete combustion of diesel and biodiesel surrogates, on a Santoro-type burner with a diffusion flame, are compared with those obtained on an engine bench (Renault-Volvo Trucks). Therefore, some physico-chemical techniques are employed. Laser diffraction analysis and transmission electron microscopy (TEM) are used to obtain the particle size at different scales. In addition to TEM analysis, Raman spectroscopy gives information about internal structure of soot. Thermogravimetric (TGA) and elemental analysis (CHNS/O) provide information about soot composition in terms of elemental compounds, ash and soluble organic fraction (SOF). This part of the study allows to better understand the process of soot formation and oxidation and to establish a link between particles properties and their oxidation in a Diesel Particulate Filter (DPF). Furthermore, through the comparison between “model” and “real” soot, the use of the Santoro academic burner in production of soot can be validated for future studies.

In a second step, the regeneration process of a DPF is simulated with temperature programmed oxidation (TPO) experiments, in presence of oxygen and nitrogen dioxide. Finally, the interaction between a catalyst and soot, under different atmospheres and different contact conditions, is analysed.

4.1 Soot structure and composition

4.1.1 Particles size distribution: Aggregates

Research has tended to focus on the size distribution of primary particles (nanometric scale), produced in the combustion chamber of diesel engines. However, a reduced number of experiments were carried out at the micrometric scale. Few attempts have been made to collect information about the size of soot agglomerates collected in the exhaust line output.

Particles size is an important feature on human health and urban pollution. Smallest ones have an increased residence time in the atmosphere. Biggest ones can lead to building soiling. On the other hand, smaller particles are more dangerous for the respiratory system because they can reach more critical area (pulmonary alveoli for the smallest ones). Therefore, the influence of biodiesel on soot size distribution has become the research focus in recent years. The laser diffraction analysis was used in the present work to determine the size distribution of “model” and “real” soot aggregates (Figure 20).

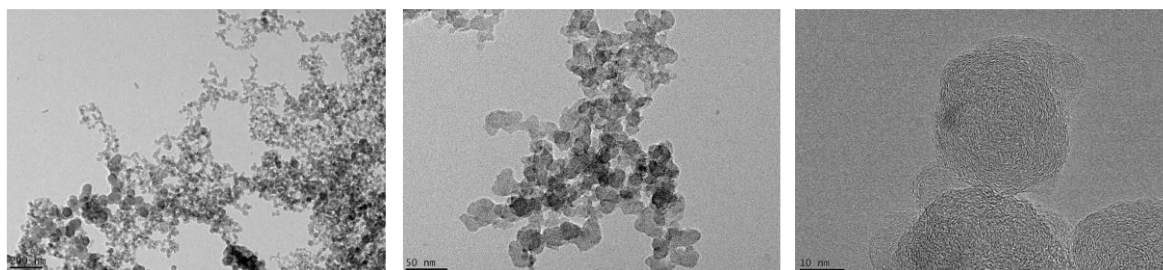


Figure 20. TEM images of «Aref» soot at 200, 50 and 10 nm, respectively.

The dimension of soot particles can be represented as a continuous distribution density curve ($dQ_3(x)$), in which the area below the curve corresponds to 100% of the population. Index 3 means that the mean diameter is pondered by volume. The Y-axis represents the percentage of total sample volume with a specific diameter (μm), identified on the X-axis. The particle size (geometrical dimension) is measured as an “equivalent diameter”, considering the particle as a sphere.

Figure 21 shows the size distribution of soot aggregates obtained through the combustion of biodiesel surrogates with 7% of methyl ester-based additives («MB7», «MO7» and «MD7»), as well as the diesel surrogate «Aref».

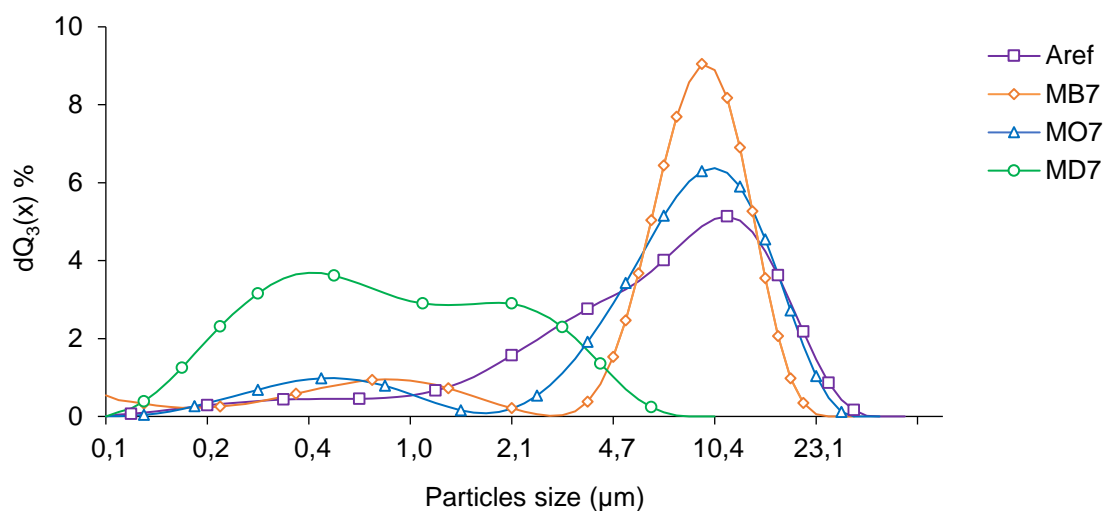


Figure 21. Size distribution of “model” soot aggregates from the diesel surrogate and biodiesel surrogates (7%).

According to Kittelson *et al.* [124], diesel particles can be divided in three size modes. The “Nuclei Mode” is composed by particles in the 0,003-0,03 μm diameter range. It usually consists of volatile organic and sulphur compounds formed during exhaust dilution and cooling, which may also contain solid carbon and metal compounds. This mode typically represents 1 to 20% of the particle mass and more than 90% of the particle number. In the “Accumulation Mode” (0,03-1 μm), carbonaceous agglomerates and associated adsorbed materials are found. Most of the particles mass is present in this mode. Finally, the “Coarse Mode” (>1 μm) is composed by accumulation mode particles that have been deposited on cylinder and exhaust system surfaces. It represents 5 to 20% of the particle mass.

Interestingly, it can be observed through [Figure 21](#) that soot samples present a bell shape distribution with two peaks – Bimodal distribution (each mode represents a different soot population). Tested model soot particles are between the “*Accumulation Mode*” and the “*Coarse Mode*” even though «MD7» soot has lower particles size than the other models.

The studied biodiesel surrogates are composed by molecules with the same functional group, and only differ on the carbon chain length in the following order: «MB7» < «MO7» < «MD7». According to the results, when a methyl ester-based additive is added to the diesel surrogate to form a blend with 7% of biodiesel surrogate, the combustion of the fuel produces smaller soot particles. However, this effect is far more relevant when the biodiesel surrogate is composed by molecules with longer carbon chains. In fact, the effect of decreasing particles size is greater when a «MD7» surrogate is used. «Aref» distribution has its principal mode at 11,5 µm, whereas for «MB7» and «MO7» it's at 10,5 µm. This difference can be considered as negligible. Concerning «MD7» soot, there is a first mode at 0,4 µm and another one at 2,1 µm.

The same comparison was made between “model” soot samples with 30% of methyl ester-based additives («MB30», «MO30» and «MD30» – see [Appendix C](#)). Several modes were observed in the distribution and an increase of the carbon chain length was associated to smaller particles.

Several works were developed to understand and explain the correlation between the particles size and the nature of the fuel. Coniglio *et al.* [4] proposed a mechanism, presented in [Figure 22](#), to explain the main reaction pathways of CO and CO₂ formation through the pyrolysis and/or oxidation of methyl esters. According to the scheme, CO and CO₂ formation derived from the decomposition of the fuel molecule, is divided in two main steps:

1. Consumption of the methyl ester through either unimolecular reaction (at high temperature) or bimolecular H-abstraction reactions (at high and/or low temperature). The unimolecular route leads to the formation of two radicals $\cdot\text{CH}_3$ and $\text{R}(\text{CH}_2)_3\text{C}(\text{O})\text{O}\cdot$ (P1). Regarding the bimolecular route, the reactions mainly occur at position 3 or 4 of the carbonyl group, leading to the formation of radicals (P3) and (P4) by successive β -scission reactions. These two radicals are key species responsible for CO and CO₂ production.
2. Unimolecular β -scission reactions of the already formed radicals (P1, P3 and P4). Radical (P4) may undergo two channels of decomposition, which lead to either CO₂ through various low-temperature routes (P7 and P8) or CO through successive β -scission reactions (P9). The (P3) radical can lead to CO (P5) or CO₂ (P6) and determines the extent of the ratio CO₂/CO produced, and therefore, the efficiency of the fuel to reduce soot precursor formation.

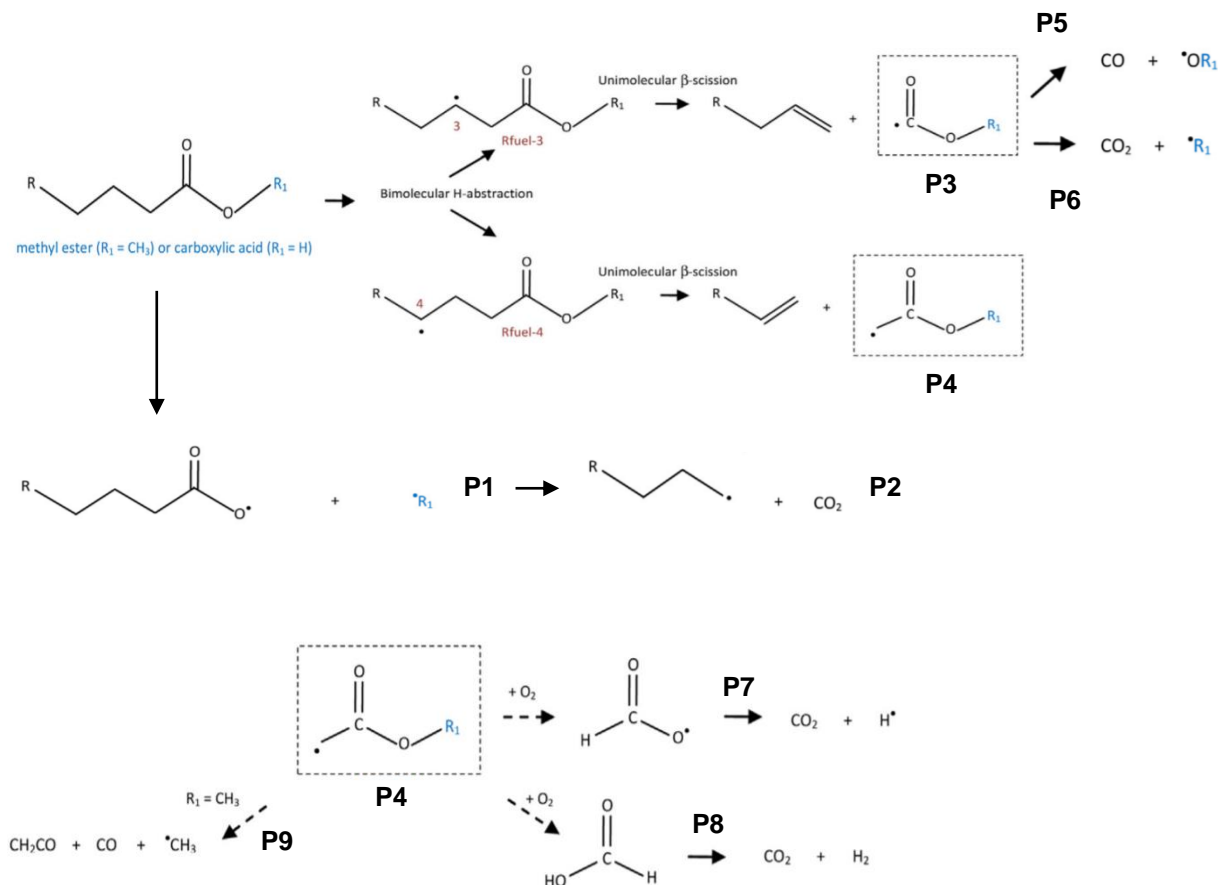


Figure 22. Main pathways of CO and CO₂ formation via pyrolysis or oxidation of methyl ester compounds at high and/or low temperature as proposed by Coniglio *et al.* [4]. Dashed arrows mean several successive reactions.

Emission of CO₂ implies that the oxygen is used to produce this gas instead of inhibiting the atoms of carbon, present in the ester structure, to be available to form soot precursors [134]. Consequently, a better effectiveness in reducing soot precursors and therefore, in reducing soot growth, is attained with the pathways leading to the formation of small amounts of CO₂ coming directly from the decomposition of the methyl ester-based compound. Oxygenated radicals will contribute thereafter to the oxidation of soot precursors and prevent the carbon atoms contained in the ester structure from becoming available to produce new ones.

Additionally, according to Szybist *et al.* [135,136], the decarboxylation process, which leads to CO₂ formation directly from the oxygenated fuel, just happens after the complete consumption of the aliphatic carbon chain of the methyl ester. Consequently, fuels with long carbon chains (such as «MD» ones) have the production of CO₂ delayed, keeping the oxygenated radicals available in the flame during a longer time and resulting on a more efficient reduction in soot production and growth.

This trend is in accordance with the results obtained by Pepiot-Desjardins *et al.* [137]. They studied the tendency of soot production and growth through the combustion of a diesel surrogate (n-heptane/toluene). They correlated the molecular structure of oxygenated compounds present in the surrogate with the concentration of aromatics, produced during the combustion process. For the same

oxygen mass fraction in the surrogate and the same functional groups, they found that oxygenated additives with longer carbon chains were more effective in reducing soot formation and growth.

Beside the carbon chain length, the concentration of oxygenated compounds in the Biodiesel and/or Biodiesel surrogate also plays an important role on the particles size. Figure 23 shows the size distribution of different soot samples, namely “models” from the combustion of surrogate with methyldecanoate («MD7», «MD30») and those obtained on engine bench.

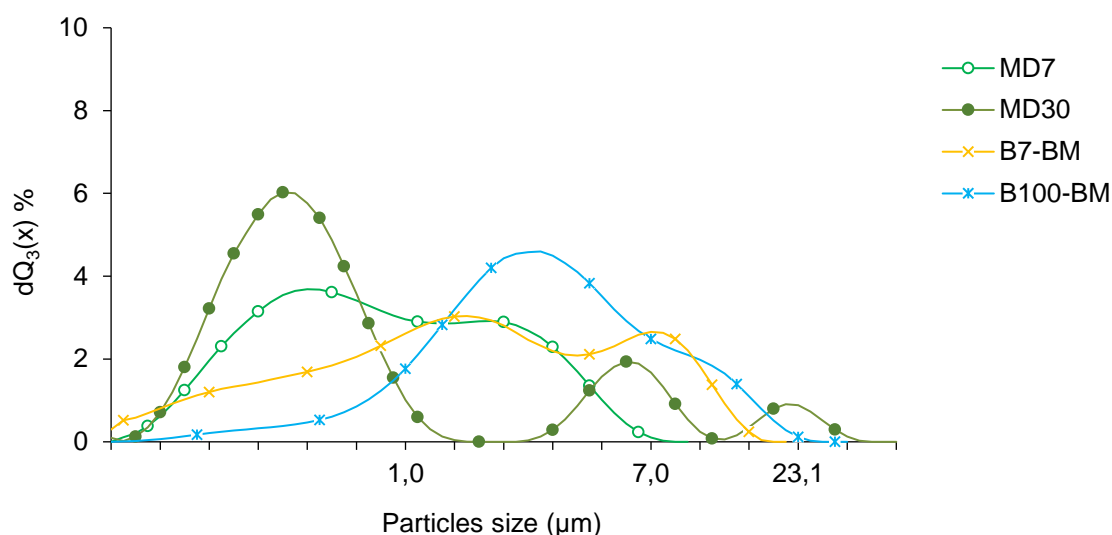


Figure 23. Size distribution of “MD” soot aggregates with 7% and 30% of additives and of “real” soot.

It can be visibly seen that the different soot samples show different size distribution profiles. «B7-BM» and «B100-BM» samples present a wide distribution and have also two modes. Concerning «B7-BM» soot, two peaks are separately centred at about 1,6 µm and 7 µm. For soot from pure biodiesel, the main peak is about 2,9 µm. In the overall, soot from engine bench seems to have smaller aggregates than “model” soot samples except for those obtained by a surrogate with methyl decanoate («MD7» and «MD30»). Moreover, it is clearly observed that the increase of oxygenated compounds percentage in the biodiesel surrogate leads to the production of smaller particles. Despite the presence of two modes for bigger particles, which is due to the unavoidable agglomeration effect, «MD30» soot aggregates are globally smaller than «MD7» ones. The same tendency was observed with «MB» and «MO» samples (Appendix C).

These results are consistent with those presented by Lin *et al.* [138], who analysed the impact of different biofuels on the size distribution of soot produced in a HD-vehicle engine. They also concluded that the addition of biodiesel to a diesel fuel promoted a decrease in particles size and an increase in the percentage of small particles. In fact, the pyrolysis of fuel with oxygenated compounds leads to the production of O* and OH* radicals, which promote higher oxidation of soot [63,139]. Therefore, the higher the additive content, the higher the oxygen content and consequently, the higher the oxidation process. Soot particles size also depends of different phenomena occurring inside the flame (Figure 24) and of different parameters, such as rate, burner diameter and nature of the combustible.

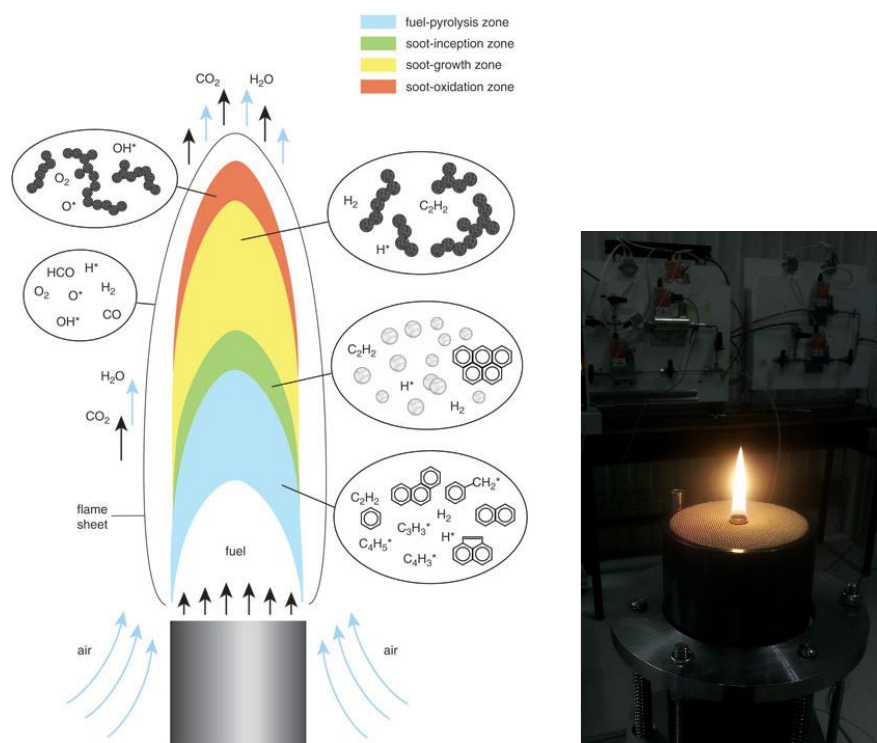


Figure 24. a) Typical locations of soot formation in a diffusion flame [140]. c) Santoro burner used to obtain “model” soot, with a stable diffusion flame.

Furthermore, the pyrolysis of fuel with oxygenated species leads to a high production of carbon monoxide. This gas, in which one atom of oxygen reacts with one atom of soot carbon [141], is a stable molecule that doesn't decompose during the pyrolysis step. In the case of carbon dioxide, two atoms of oxygen are required to form the molecule and consequently, the oxygen is mostly used to produce CO_2 and not soot precursors [141]. Consequently, it is expectable to produce smaller soot particles from surrogates with a higher content of oxygenated compounds.

In addition to the chemical effect, addition of oxygenated compounds to the diesel surrogate implies the substitution of aromatic compounds (α -MN) by others producing less soot precursors. Therefore, the dilution effect leads to the reduction of particles growth through coagulation and surface reactions, due to the low concentration of PAH and acetylene inside the flame [118,142].

Globally, these results illustrate that the combustion of biodiesel surrogate is beneficial to the formation of smaller soot particles aggregates. Furthermore, it can be assumed that the results concerning the size distribution of “model” and “real” soot aggregates are present on a comparable scale. However, pure biodiesel was expected to have smaller particles than the diesel fuel, but it can be observed that they are approximately in the same range. During soot particles emission through the exhaust line, agglomeration phenomena occur, which can't be controlled. Diverse compounds are adsorbed, such as gas phase hydrocarbons, sulphates, water and metallic compounds. Therefore, this study is considered as a comparative analysis. To go further in detail, soot composition and internal structure were investigated.

4.1.2 Soot composition

The composition of soot particles is a key factor that governs their reactivity. Soot composition was determined by elemental analysis (CHNS/O) and TGA under air and nitrogen for the ash, water and soluble organic fraction (SOF) content. Table 6 shows the composition of soot samples obtained through the combustion of surrogates, diesel and pure biodiesel. The evolution of mass loss (wt%), under air and under nitrogen, can be visualized in Appendix D.

Table 6. Composition of soot.

Sample	%C ¹	%H ¹	%O ¹	%ash ²	%H ₂ O ³	%SOF ⁴	% Sum
Aref	87,2	1,0	6,2	0,58	0,59	3,09	98,66
MB7	87,4	1,2	4,7	0,39	0,60	3,26	97,55
MO7	87,8	0,9	4,4	0,16	0,59	3,01	96,86
MD7	89,5	0,9	3,5	0,00	0,45	2,09	96,44
MB30	88,3	1,0	4,2	0,52	0,53	3,29	97,84
MO30	89,7	1,0	3,6	0,09	0,29	2,39	97,07
MD30	91,4	0,8	3,2	0,62	0,37	1,45	97,84
B7-BM	89,5	1,2	3,8	1,84	0,28	3,02	99,64
B100-BM	83,1	1,3	6,2	7,78	0,42	4,15	102,95

¹Elemental composition CHNS/O

²Determined from the mass loss between 30 and 700°C in TGA under air

³Determined from the mass loss between 30 and 110°C in TGA under nitrogen

⁴Determined from the mass loss between 110 and 400°C in TGA under nitrogen

The other elements weren't detected.

According to the results, it can be noted that all “model” soot samples have a similar elemental composition. Carbon content is comprised between 87,2 and 91,4 wt%, hydrogen content is around 1 wt% and for oxygen is between 3,2 and 6,2 wt%. A low quantity of water is adsorbed on the soot surface (< 1 wt%) and, in agreement with their production mode, all soot samples have a very low ash content (< 1 wt%). In fact, ash can come from different metallic elements, provided by the additives in the lubrication oil and fuel or by engine wear.

Concerning carbon, higher proportion of oxygenated compounds and/or longer carbon chain leads to higher carbon content. On the contrary, the content of oxygen decreases when the concentration and/or the carbon chain length of such additives increases. For instance, «MD7» soot has 3,5 wt%, while «MD30» one has 3,2 wt%. This means that during their formation, «MD30» particles were subjected to higher oxidation, leading to higher consumption of this gas. This phenomenon can be explained by the predominance of soot oxidation over the formation of soot precursors, due to the abundance of oxygenated radicals produced during the pyrolysis of biodiesel surrogate [59,63,141]. As complementary explanation, longer carbon chains and therefore, higher number of carbons in the surrogate, lead to a higher residence time of soot particles in the flame and consequently, to a higher consumption of oxygen.

Finally, the SOF content follows the same tendency as oxygen and seems to be linked to the additive content. In the overall, the content of soluble organic fraction decreases when increasing the concentration of oxygenated compounds and/or their carbon chain length. This fraction is mainly composed by heavy aromatics compounds that were not incorporated in the IOF fraction, aliphatic chains and oxygenated compounds. Thus, as already explained, addition of oxygenated additives to the diesel surrogate implies the substitution of aromatic compounds (α -MN) by others with less tendency to produce soot precursors (dilution effect) [118,142]. Consequently, the SOF content decreases with the addition of additives to the surrogate of reference. Concerning the evolution of this fraction in function of the carbon chain length, such occurrence is dependent of each type of molecule and the chemical reactions taking place in the laminar diffusion flame. However, it seems that the longer the carbon chain is, more complete is the combustion in the flame, resulting in a lower amount of SOF content. To obtain further information, a continuous monitoring of the soot composition and structure along the flame should be carried out.

Concerning “real” soot, particles from pure biodiesel have a higher oxygen content due to the higher presence of oxygen complexes in this fuel. Consequently, and due to the higher oxidation process, they have a lower carbon content. They also have higher SOF content because of the additives used in biodiesel. Additionally, the increase of biodiesel concentration leads to an increase of the ash content. In fact, «B7-BM» soot has 1,84 wt%, while «B100-BM» has 7,78 wt%. In general, soot from the engine bench has more ash content than the “model” one, due to the presence of additives and corrosion phenomena. On the other hand, an increased biodiesel concentration is generally accompanied by an increase of inorganic compounds content, which promote ash formation.

4.1.3 Raman Spectroscopy

In addition to the size and composition, soot nanostructure can also give valuable information about particles formation and oxidation. Therefore, Raman spectroscopy was used. This technique is sensitive to molecular structures and to crystalline ones. Thus, it generally informs about the abundance of amorphous and graphitized carbon and consequently, about the organization degree in the internal structure of soot. In [Appendix E](#), the main results for “model” soot with 7% and 30% of methyl ester-based additives, as well as “real” soot, can be analysed. The Raman spectrums show two overlapping peaks, as observed in [Figure 25](#). The graphitic G-peak of the graphite-like structures of soot occurs at around 1580 cm^{-1} and the D-peak for the disordered structures occurs at 1340 cm^{-1} .

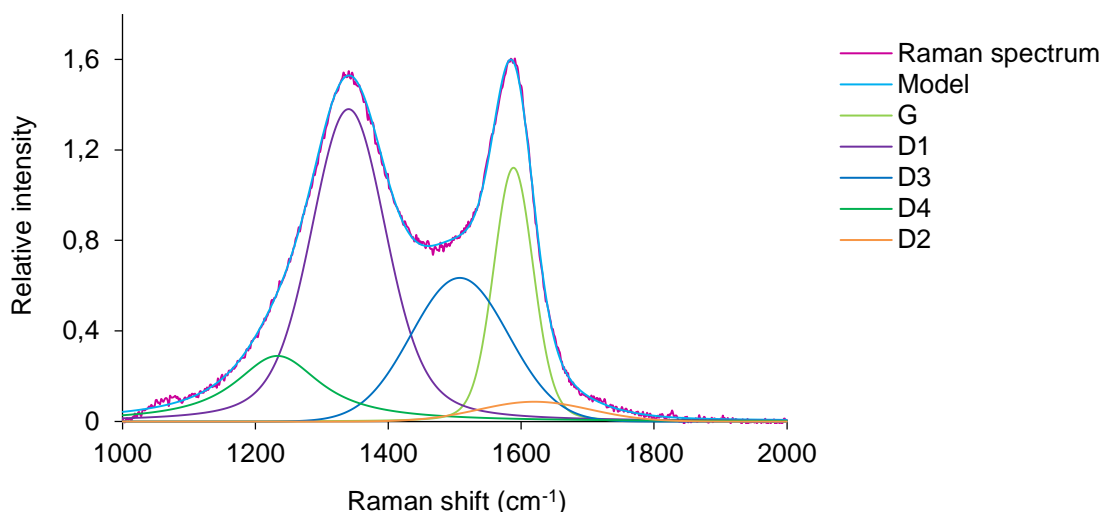


Figure 25. Raman spectrum of «B100-BM» soot sample.

In Raman spectroscopy, the ratio of intensity between D and G bands (I_D/I_G), the FWHM value (*Full Width at Half Maximum*), as well as the distance of G band from the band that represents ideal graphite (1580 cm^{-1}) provide information about structural defects on the basal plane of graphene layers and, consequently, about the carbon organisation degree in the internal soot structure. It has been shown that D1 FWHM and D3 band intensity are the spectroscopic parameters which give most information about the chemical structure and reactivity of different types of soot. A decrease of D1 FWHM indicates an increase of structural order. A high D3 peak intensity relatively to the G peak is related to a more amorphous soot internal structure. On the other hand, a bigger distance between the G band and the band that represents an ideal graphite is also related to a less graphitic structure [128,129,143,144].

These parameters can then be correlated with soot oxidative reactivity. It is known that a less organized and more amorphous structure allows to a better accessibility of oxygen to carbon active sites and consequently, to an easier soot oxidation [57,61]. Table 7 shows the main results from Raman Spectroscopy for all samples.

Table 7. FWHM (cm^{-1}) of D1 band, Raman shift (cm^{-1}) of G band and I_{D3}/I_G ratio obtained through Raman spectrums of the studied soot samples.

Soot	D1 FWHM (cm^{-1})	G Raman shift (cm^{-1})	I_{D3}/I_G
Aref	120	1589	0,59
MB7	130	1590	0,62
MO7	126	1590	0,54
MD7	118	1593	0,65
MB30	128	1587	0,59
MO30	121	1591	0,60
MD30	113	1585	0,54
B7-BM	141	1590	0,56
B100-BM	134	1588	0,57

According to the results in [Table 7](#), the different soot particles have similar structures. The major difference is observed for the D1 FWHM. Concerning “model” soot, it is observed that «MD» particles, and especially «MD30» ones, have the lowest FWHM for the D1 band, which demonstrates that their structure may be more ordered. About particles collected on engine bench, the Raman results are also very similar. The major difference is also the D1 FWHM, which suggest a higher structural order in «B100-BM» particles than in «B7-BM» ones. Globally, due to the similarity of results between the different samples, Raman spectroscopy is not enough to conclude about significant differences in soot structure and oxidation reactivity. Thus, further studies about the internal structure of soot particles must be carried out.

4.1.4 Nanostructure

A comparative study between different soot structures can be done by the observation of the morphology and surface carbon spherules. Internal structure (nanometric scale) can be correlated with the reactivity during the oxidation process. Indeed, soot reactivity is dependent on its nanostructure [67]. Therefore, images obtained by Transmission Electron Microscopy (TEM) were analysed. [Figure 26](#) shows HR-TEM images of «MD7» and «MD30» samples and soot from the surrogate diesel «Aref».

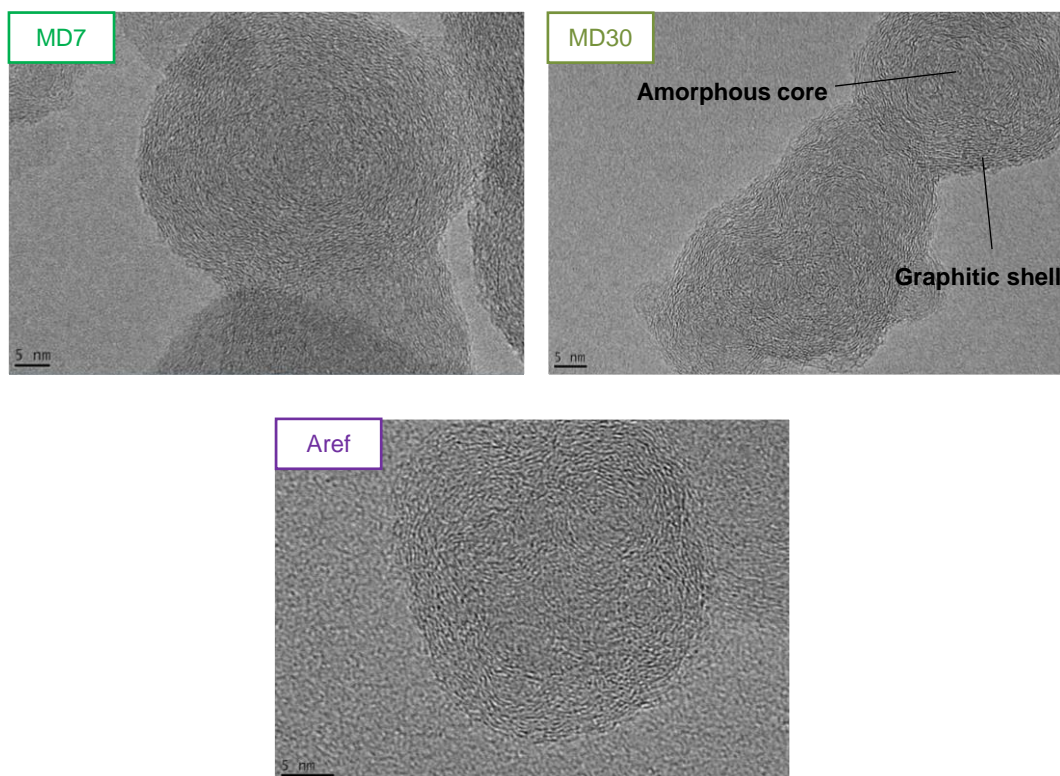
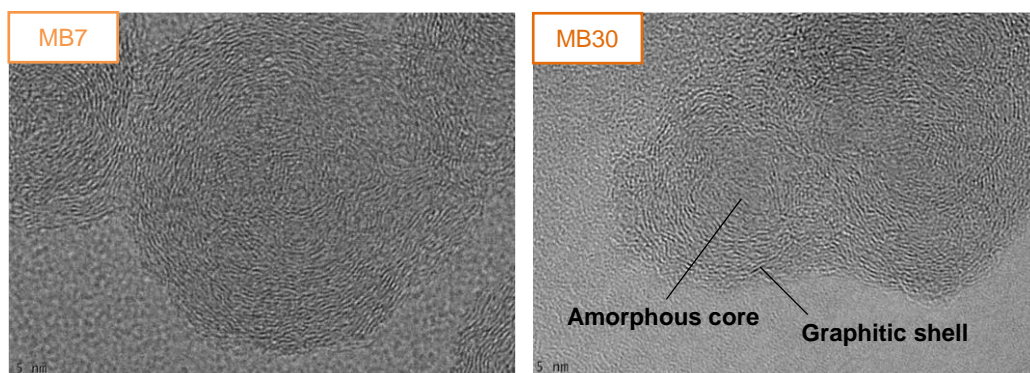


Figure 26. HR-TEM images of «MD7», «MD30» and «Aref» soot samples.

As other investigations have highlighted [60,145,146] through HR-TEM analyses, soot undergoes an internal combustion in presence of oxygen. Particles show an empty core and a more ordered crystalline structure on the periphery, with graphitic carbon layers parallel to soot surface. According to Song *et al.* [60], oxidation of soot is divided in three steps (Figure 8):

1. Firstly, the dominant process is surface burning, leading to a decrease of particle size and development of micropores. In fact, some organic compounds are adsorbed on the particle surface or filled in the gap between adjacent primary particles or in the defects of orifices due to phenomena of adsorption and condensation during soot formation. Volatilization and gasification of these species exposes the available internal surface of soot and the defects/orifices develop into micropores through further oxidation.
2. The second step corresponds to an internal oxidation of the amorphous carbon core, which is far more reactive than the graphitic carbon.
3. Then, a more ordered layer arrangement in the outer shell appears. Consequently, long layers oriented parallel to the external surface are observed at the periphery whereas in the central core region there are shorter layers randomly oriented. Furthermore, multiple particles start to coalesce.

Through Figure 26, it is observed that this process happens with «MD7» and «MD30» soot, especially with «MD30», where the core is amorphous due to a higher oxidation while the periphery has a graphitic structure. In the case of «MD7» and «Aref» samples, their oxidation in the flame were not enough to produce this type of structure. They have still a blurry and highly disordered surface. It is clear that the oxidation was more advanced for soot from a surrogate with 30% of oxygenate additives. This comparison is also available for «MB» and «MO» samples (Figure 27). These observations are in good agreement with the results obtained by Raman spectroscopy (Appendix E), where it is concluded that «MD30» soot as a more ordered structure than «MD7» one. They are also coherent with those obtained by thermogravimetric analysis (TGA) and by elemental analysis (CHNS/O) about the composition of soot particles, confirming the higher oxidation reactivity of soot from surrogates with higher oxygenated compounds content.



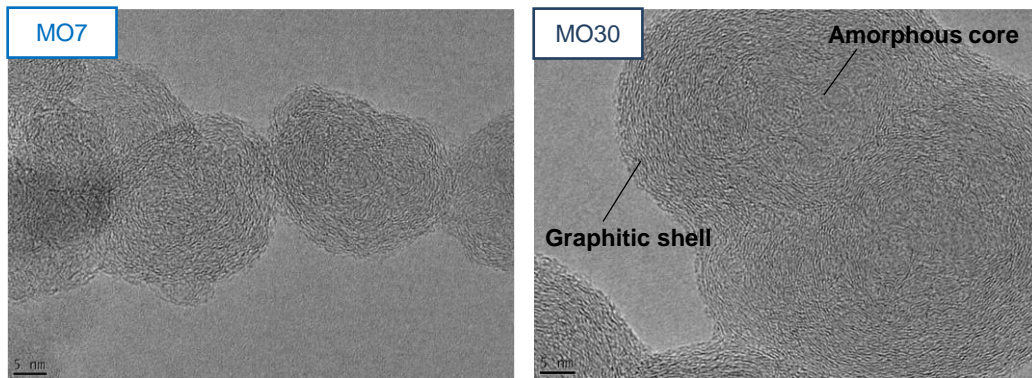


Figure 27. HR-TEM images of «MB7», «MB30», «MO7» and «MO30» soot samples.

Internal oxidation can also be observed in soot collected on engine bench. In Figure 28, well defined graphene layers are present in the outer part of the spherules, while amorphous carbon can be seen in the internal core. Comparing “model” and “real” soot micrographs, “real” ones seem to show a more ordered structure.

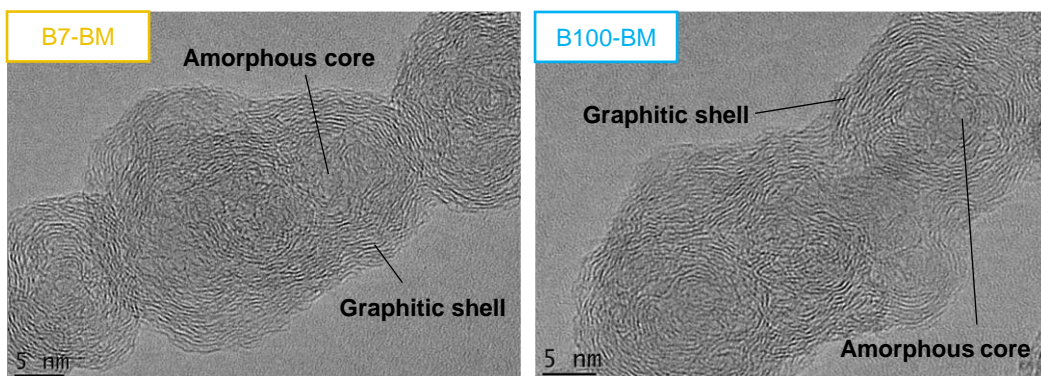


Figure 28. HR-TEM images of soot collected on engine bench.

4.1.4.1 Dimension of spherules

Aggregates are composed by smaller particles, called spherules (primary particles). As the name implies, most of these particles are almost spherical but a number of less regular shapes may be found. Figure 29 exhibits the size distribution of soot spherules from the diesel surrogate «Aref» and biodiesel surrogates with 7% and 30% of methyl ester-based additives. «MB», «MO» and «MD» soot spherules were joint together in the same category due to the low amount of collected data. Furthermore, due to the agglomeration effect of soot particles, some TEM micrographs couldn't be used for this measurement.

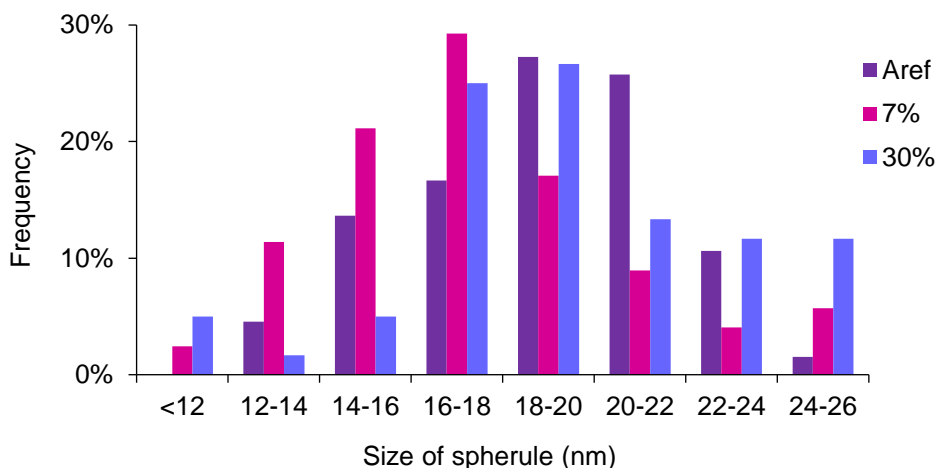


Figure 29. Size distribution of soot spherules from the diesel surrogate «Aref» and surrogates biodiesel with 7 and 30% of additives.

According to the results, the size of spherules seems to be mainly in the 16-22 nm range. Smaller spherules are expected when oxygenated additives are added to the diesel surrogate. As it was already mentioned, the addition of such additives increases the oxygen content and therefore, also increases the oxidation reactivity. However, the difference can be considered almost negligible.

There is some degree of uncertainty concerning interpretation of the results. TEM images are only projections of soot aggregates, therefore interpretation of the three-dimensional (3D) features from the two-dimensional (2D) TEM images is a nontrivial task and loss of information is unavoidable. Some spherules can be superimposed with others and/or agglomerated. Additionally, analysis of particle size from the micrographs is an operator-dependent task and therefore obtained results include user subjectivity. In Figure 30, the size of spherules from biodiesel surrogates, with 7 and 30% of methyl-ester based additives, is compared with those obtained on an engine bench.

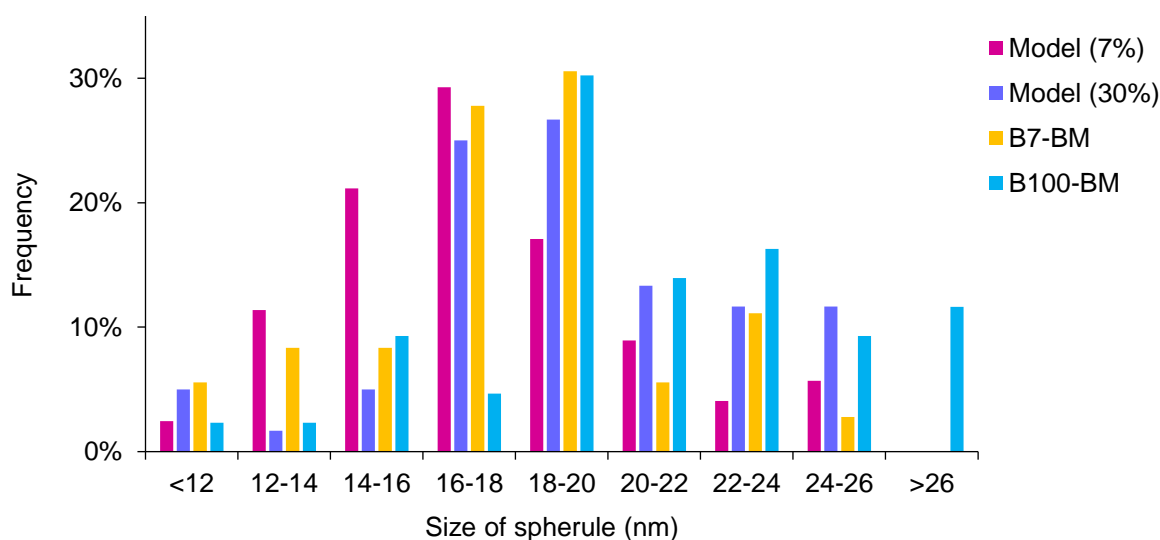


Figure 30. Size distribution of soot spherules from biodiesel surrogates with 7 and 30% of additives and from the combustion of a fuel on an engine bench (B7-BM and B100-BM).

Pure biodiesel has more surface oxygen functional groups and therefore, it should lead to a higher oxidation reactivity of soot [60,62,147,148], resulting in primary particles with smaller dimensions. However, the opposite trend is observed. According to Song et al. [60], oxidation of «B100» particles tend to coalesce during reorganization of the internal structure. This can explain the higher spherules size of biodiesel soot. Additionally, through the comparison between soot samples obtained on engine bench and “model” ones, it is deduced that “real” soots tend to have spherules with higher dimensions. Primary particles from surrogates with 7% of additives are clearly the smallest, while «B100-BM» are the biggest ones.

Conventional biodiesel is mainly composed by a complex mixture of long chain fatty acid methyl esters (FAMEs – Figure 31), which are produced through methanol-based transesterification [16,17].

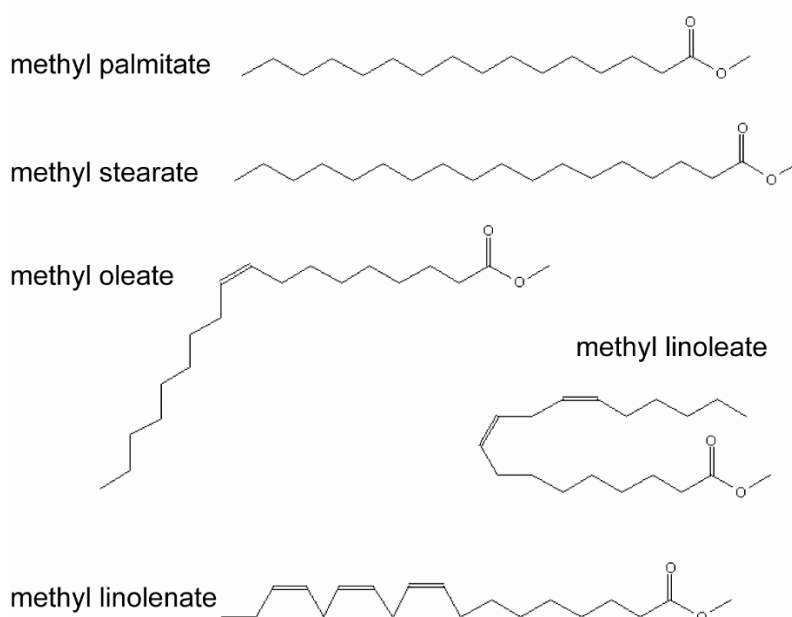


Figure 31. Common fatty acid methyl ester (FAME) found in biodiesel [149].

Biodiesel components have three unique characteristics compared to conventional diesel: absence of aromatics, presence of the ester moiety and possibly C=C double bonds in their alkyl chain. Concerning rapeseed oil, which is the raw material of «B7-BM» and «B100-BM», it is mainly composed by methyl oleate (18:1), and some considerable percentage of methyl linoleate (18:2) [150,151]. These molecules with C=C double bonds tend to produce higher levels of unsaturated hydrocarbons, which are important for soot formation and growth [152]. This can explain the higher dimension of particles from pure biodiesel.

Nevertheless, as it was already mentioned for the agglomerates size distribution, it must be kept in mind that results from TEM analysis are subjective and the measurement of spherules, which can be superimposed with others, is a difficult task. Furthermore, the number of measurements is not enough to do an accurate comparison.

4.1.4.2 Length of graphitic layer planes

To assess the reactivity of carbon towards oxidation, analysis of soot structure at the nanometric scale can be used. In turn, the number and accessibility of edge sites can be linked to soot nanostructure. Edge sites are those that are potentially accessible for H-atom abstraction followed by molecular (acetylene) addition (HACA mechanism) [153,154], potential rearrangement and/or bonding with adjacent layer planes (graphitization) [155] or for reaction with oxidizer gases. It is well known that in graphite oxidation, the reactivity of basal plane carbon atoms is far lower than that of edge site carbon atoms.

According to Levy and Wong [156], the increased activity of the edge site atoms is likely due to residual valence of those atoms and greater accessibility of edge positions. Geometrically, carbon atoms in edge sites can form bonds with chemisorbed oxygen due to the availability of unpaired sp^2 electrons. Carbon atoms in basal planes have only shared π electrons forming chemical bonds.

Vander Wal and Tomasek [58,61] used HR-TEM to show the difference in the nanostructure of soot generated under various growth conditions and fuels. They concluded that as the layer plane size decreases, the number of edge site carbon atoms necessarily increases in proportion to the number of basal plane carbon atoms, allowing the overall reactivity to increase.

The *Image J*® software was used to analyse and manipulate TEM images, in order to have a better contrast and to facilitate the detection and measurement of carbon fringes (2D projection of carbon layers). Each sample of soot can have different fringe lengths, so it is important to collect different measures from several images for the same sample. Then, the results can be exhibited as a distribution, in which the number of fringes is a function of its dimension. Furthermore, the law followed by the distribution of carbon fringe length must be known. Each law can be characterized by a group of statistic parameters, such as the mean value, standard deviation and variance.

Firstly, a cumulative curve was built with the experimental values. In other words, a curve was drawn with the cumulated number of fringes (%) as a function of its length. [Figure 32](#) represents the cumulative curve with the experimental results of carbon fringe length for the «MD30» soot.

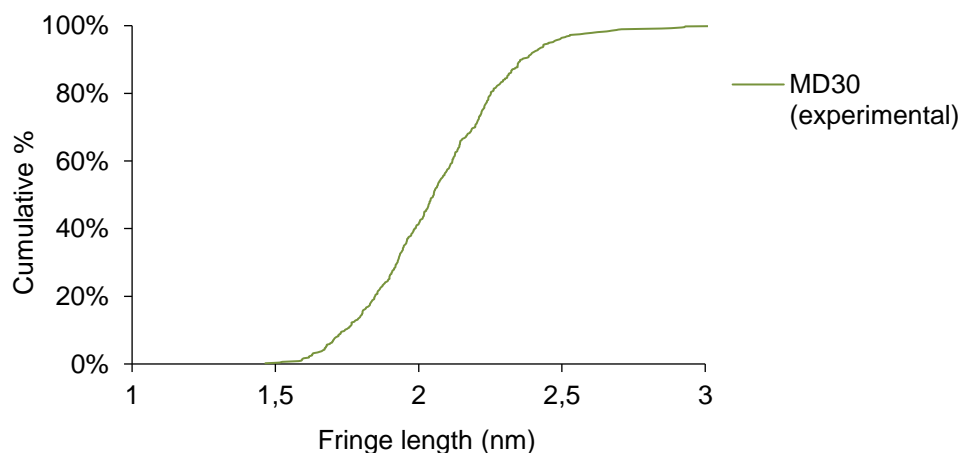


Figure 32. Experimental cumulative curve of «MD30» size distribution.

The second step consists in using a law for the distribution and then, verify if it correlates well with the experimental results. As first assumption, a normal distribution was tested for the soot fringe length. The cumulative function of the normal distribution, which is characterized by the mean value (μ), standard deviation (σ) and variance (σ^2), is represented by equation (18).

$$F(x) = \int_{-\infty}^x \frac{1}{\sigma\sqrt{2\pi}} e^{-\frac{(t-\mu)^2}{2\sigma^2}} dt, \sigma > 0 \quad (18)$$

Figure 33 shown the theoretical cumulative curve and the experimental one, based on the experimental results of carbon fringe length for the «MD30» soot. In Appendix F, the cumulative curves for the other samples can be observed.

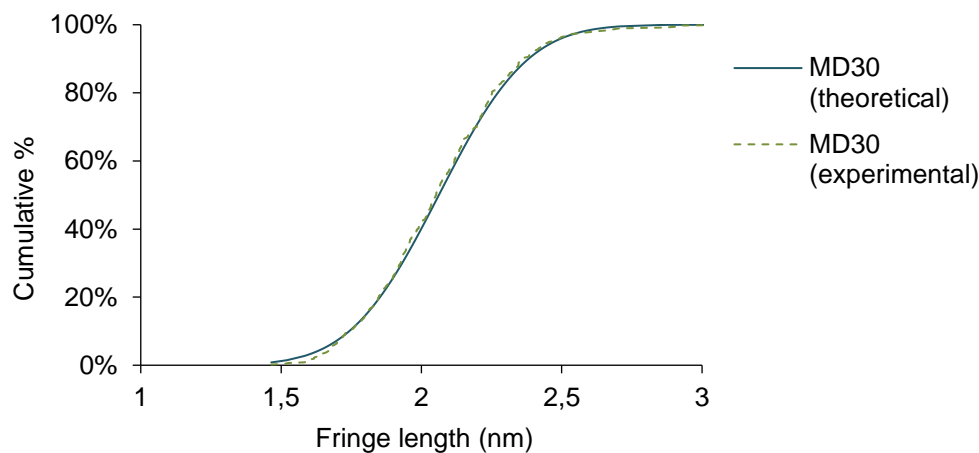


Figure 33. Theoretical and experimental cumulative curves of «MD30» size distribution.

As observed in Figure 33, the two curves are almost completely superposed. Therefore, the hypothesis of a normal distribution for the carbon fringe length of soot is validated. However, to compare the results from different types of soot, a cumulative curve is not the best option. Instead, a probability density function is more convenient. It depends on the same parameters as the cumulative curve and can be represented by equation (19).

$$f(x) = \frac{1}{\sigma\sqrt{2\pi}} e^{-\frac{(x-\mu)^2}{2\sigma^2}}, \sigma > 0 \quad (19)$$

Each numerical result is associated to a probability. In other words, it gives the probability for each value of a random variable in the form of a continue curve. This function, also called Gaussian distribution, describe a bell-shaped curve, which gives a probability of 68,3% of being within one standard deviation of the mean, which corresponds to the maximum of the curve.

Figure 34 represents the distribution of carbon fringe length of soot particles from different samples, namely from the diesel surrogate «Aref», and from biodiesel surrogates with 7% of methyl ester-based additives («MB7», «MO7» and «MD7»).

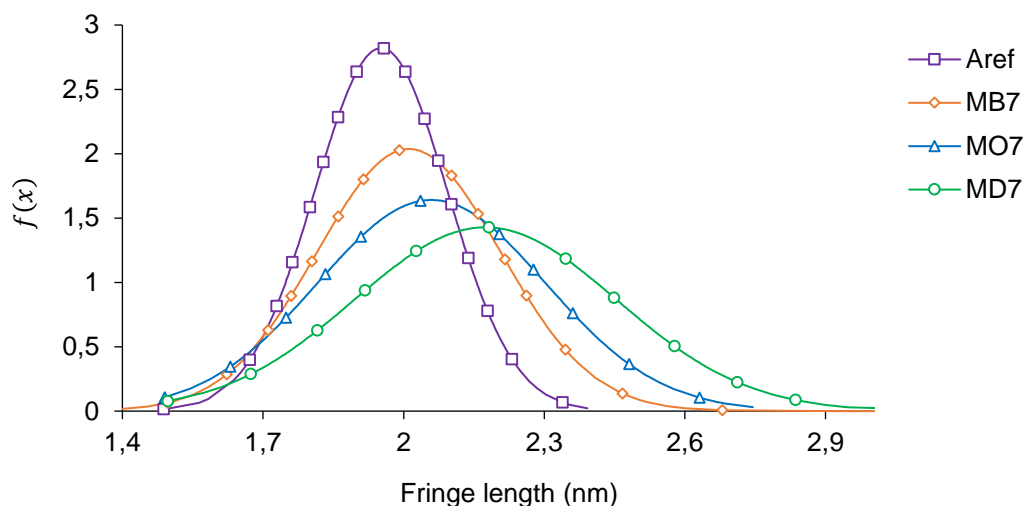


Figure 34. Carbon fringe length distribution of soot produced by combustion of the diesel surrogate «Aref» and biodiesel surrogates with 7% of methyl ester-based additives.

«Aref» soot, which comes from the combustion of a diesel surrogate without any trace of additives, has the narrowest fringe length distribution, with a mean value of 1,95 nm. On the other hand, soot particles obtained from biodiesel surrogates have a larger distribution and at the same time, they have higher mean values of fringe length than the soot of reference. Furthermore, comparing the different additives, an increase of the fringe length is observed when increasing the length of the carbon chain. The mean value and corresponding standard deviation are present in Table 8. The distribution is shifted to higher dimensions and the mean fringe length respects the following order:

$$L_{\text{«Aref»}} < L_{\text{«MB7»}} < L_{\text{«MO7»}} < L_{\text{«MD7»}}$$

Table 8. Mean value (nm) and standard deviation (σ) of the normal distribution of soot fringe length from diesel surrogate «Aref» and biodiesel surrogates «MB7», «MO7» and «MD7».

Sample	Mean value (nm)	Standard deviation (σ)
Aref	1,95	0,14
MB7	2,01	0,20
MO7	2,06	0,24
MD7	2,17	0,28

The same tendency is observed for samples obtained through the combustion of biodiesel surrogates with 30% of additives (Appendix F). However, with 30% of oxygenate compounds, the difference of fringe length is not so considerable. In fact, the mean value for «MB30» and «MO30» soot is almost the same. The mean value for fringe length has the following order:

$$L_{\text{«Aref»}} < L_{\text{«MB30»}} \sim L_{\text{«MO30»}} < L_{\text{«MD30»}}$$

It can be suggested that there is a correlation between the fringe length of soot and the length of the aliphatic carbon chain of additives present in the biodiesel surrogate. The longer the chain, the larger the distribution of fringe length and higher the mean value. Thus, it is supposed that an increase in the dimensions of the segments correspond to a lower number of edge sites, higher graphitization and a parallel decrease in oxidation reactivity. These results are coherent with Raman spectroscopy.

Figure 35 represents the carbon fringe length distribution of soot obtained from biodiesel surrogates with two different concentrations of oxygenate compounds («MD7» and «MD30») and the two “real” soot samples («B7-BM» and «B100-BM»).

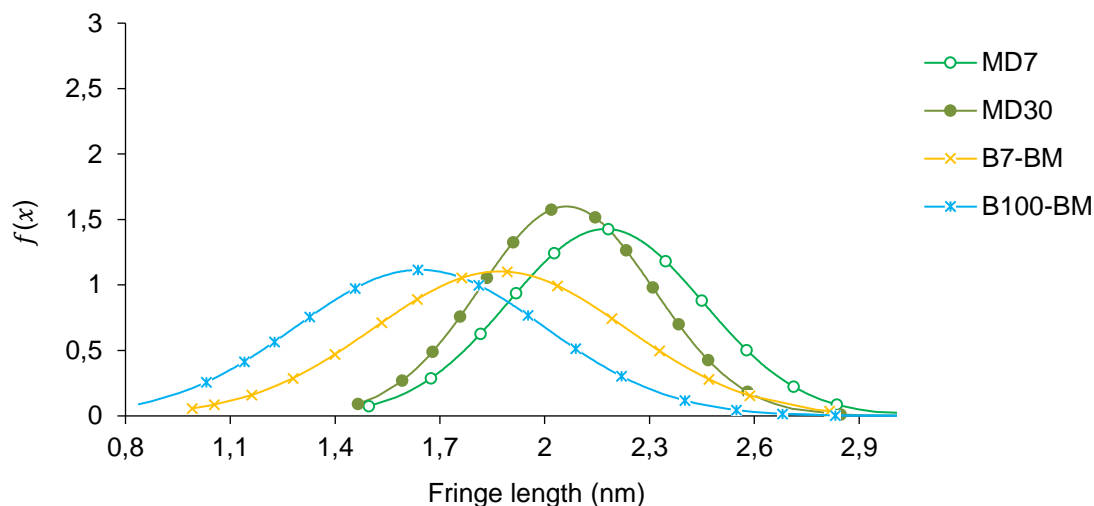


Figure 35. Carbon fringe length distribution of soot produced by combustion of «Aref», biodiesel surrogates with 7 and 30% of methyl decanoate and fuel on engine bench (7 and 100%).

«MD7» and «MD30» distributions belong to soot obtained by surrogates that only differ on the oxygenated additives content. As observed, when the concentration of such compounds is increased, the distribution is shifted to smaller fringe length. In fact, with a higher oxygen content, soot is more prone to be oxidized in the flame and consequently, fringes become smaller. In Appendix F the same tendency can be deduced between «MB7» and «MB30» soot as well as between «MO7» and «MO30».

Concerning soot particles obtained from the combustion of biodiesel on an engine bench, the same interpretation can be done. «B100-BM» is a pure biodiesel, with a higher oxygen content. Thus, it leads to the formation of soot with shorter fringes than the «B7-BM» one [157,118], which proves that biodiesel soot has higher oxidation reactivity. The mean value and corresponding standard deviation are present in Table 9.

Table 9. Mean value (nm) and standard deviation (σ) of the normal distribution of soot fringe length from diesel surrogate «Aref», biodiesel surrogates «MD», as well as “real” diesel and biodiesel.

Sample	Mean value (nm)	Standard deviation (σ)
Aref	1,95	0,14
MD7	2,17	0,28
MD30	2,06	0,25
B7-BM	1,87	0,36
B100-BM	1,64	0,36

Transmission Electron Microscopy was used as a qualitative analysis. The mean value of fringe length is obtained through a Gaussian function, which is based on probability calculations. Furthermore, some trends are found but, in fact, different molecules can't be directly compared. On the contrary, surrogates composed by the same molecules but with a different additive content can be objectively compared. In general, despite the larger distribution of “real” soot samples, “model” ones seem to present fringes length in the same range as those produced on a bench engine.

4.1.4.3 Interplanar space distribution

The distance between adjacent carbon layer planes (Figure 36) can also be correlated with the oxidation reactivity of soot. However, inter-fringe spacing is a function of the relative orientation between stacked carbon layers, the presence of interstitial atoms, hetero-elements and cross-links between adjacent layers [39]. The same procedure was followed as with fringe length.

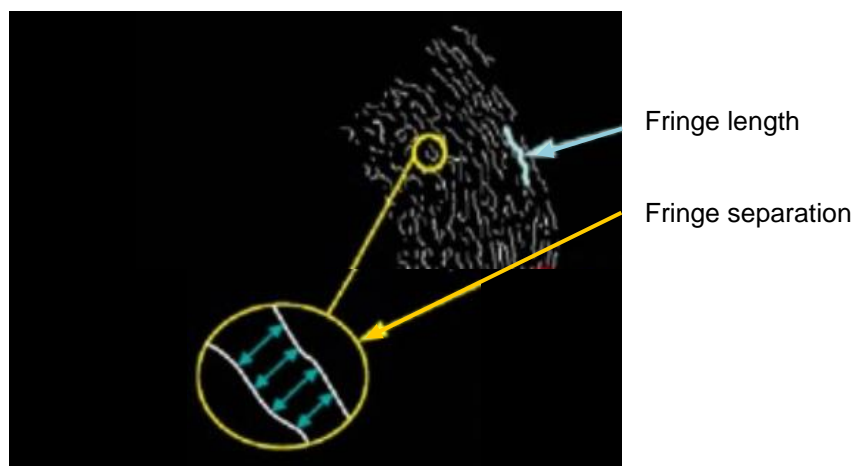


Figure 36. Particle nanostructure parameters [158].

In the literature [62,118], a higher mean fringe separation distance was observed for particles from biodiesel, in comparison with diesel. Other researchers found the opposite tendency [87]. Finally, Alfè *et al.* [53] observed that the mean interlayer spacing was almost the same for all types of investigated soot. Thus, no consensus was already achieved concerning this parameter. In theory, a higher space

between parallel fringes should allow to a better attack of oxygen to the soot, contributing to an easier and faster oxidation. All those investigations found values in the 0,3-0,5 nm range for this parameter [147,159,160]. In the present work, for both “model” and “real” soot samples, the mean value was comprised between 0,3 and 0,4 nm. Therefore, according to the results, it’s taken as assumption that this parameter doesn’t depend on the fuel composition or structure and the most reliable factor is the length of carbon layer planes.

With the different types of characterization, despite some differences, it was proved that with the system of production and recuperation of soot on a Santoro burner, it is possible de produce “model” soot with physico-chemical properties (composition, structure and size distribution) close to those of soot collected on a DPF of an engine bench with the same working conditions as on a HD-vehicle on road. After analysis and validation of soot properties, it is of great interest to study the oxidation reactivity of these samples and to simulate their behaviour inside a Diesel Particulate Filter. Finally, a correlation between soot properties and oxidative reactivity can be established. For this purpose, elemental composition, thermogravimetric analysis, Raman spectroscopy and TEM analysis were used to do this comparison. Due to the agglomeration effect and low amount of collected data, particles size was not used.

4.2 Soot oxidation reactivity

After the physico-chemical characterization of soot particles, their oxidation reactivity and therefore, the ease of the DPF regeneration was assessed. The impact of the methyl ester-based oxygenated compounds concentration on “model” soot reactivity was investigated. Furthermore, the oxidation behaviour of “real” and “model” soot was compared. Thus, several tests through Temperature Programmed Oxidation (TPO), under different oxidizing gases (O_2 , NO_2), were performed. O_2 and NO_2 were selected to represent the main exhaust gases present in the post-treatment system during DPF active and passive regeneration. Additionally, interaction between the samples and a catalyst was evaluated to describe the regeneration process in a catalysed DPF.

The comparison was made in terms of maximum oxidation temperature (T_m), which also represents the temperature of maximal CO_x emission. The reaction performance was also assessed by the values of T_{10} , T_{50} and T_{90} , which were defined as the temperature at 10, 50 and 90% of soot carbon conversion, respectively. The temperature range of combustion process, between 10 and 90% of conversion (ΔT), as well as the selectivity of CO_2 at the maximal oxidation rate were also determined. It must be kept in mind that soot of high reactivity is preferable because the regeneration of the filter can be performed at lower temperatures and therefore with small energy demand.

«MD7» and «MD30» samples were used to represent soot from biodiesel surrogates with 7% and 30% of methyl ester-based additives, respectively. “Real” soot, produced on an engine bench, under real driving conditions, were represented by «B7-BM» and «B100-BM» ones.

4.2.1 Non-catalytic soot oxidation

4.2.1.1 TPO in 9% by volume O_2/Ar

A temperature programmed oxidation was carried out with an oxidizing mixture of 9% O_2/Ar , to simulate a non-catalysed DPF active regeneration. [Figure 37](#) shows the evolution of the carbon specific oxidation rate in function of the temperature.

[Table 10](#) exhibits the main results of the TPO analysis, such as temperature at 10, 50 and 90% of carbon conversion, temperature of maximal oxidation rate, ΔT between 10% and 90% of conversion and selectivity to CO_2 formation in the outlet gas during soot oxidation process.

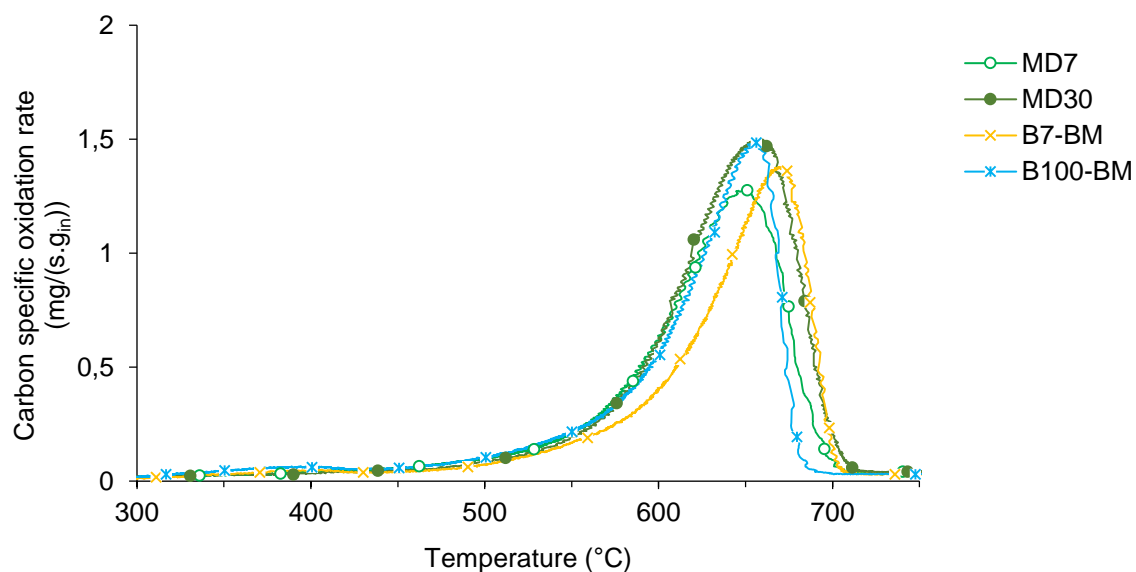


Figure 37. Carbon specific oxidation rate (mg/(s.g_{in})) of “model” and “real” soot (9% O₂/Ar).

Table 10. Temperature programmed oxidation results in 9% O₂/Ar.

	T _m (°C)	T ₁₀ (°C)	T ₅₀ (°C)	T ₉₀ (°C)	ΔT	S _{CO₂} (%) ¹
MD7	650	498	631	674	176	49
MD30	657	528	640	686	158	47
B7-BM	669	517	647	683	166	55
B100-BM	656	490	631	667	177	69

¹CO₂ selectivity at T_m

Figure 37 and Table 10 illustrate the oxidative performance of the different soot samples under 9% O₂/Ar. It can be observed that all oxidation reactions start at more than 450°C. In the case of “model” soot, the maximum specific oxidation rate for the «MD7» sample occurs at 650°C, while 657°C is attained for the «MD30» one.

In general, reactivity of soot particles decreases when the concentration of oxygenated compounds in the surrogate is increased. These results are coherent with the soot composition obtained through elemental and thermogravimetric analysis. Indeed, «MD7» particles contain a higher oxygen and SOF content than the «MD30» ones. The soluble organic fraction, which consists of unburned hydrocarbons, oxygenated compounds, sulphate species, metallic compounds, vapor phase hydrocarbons, water and nitrogen, provides an easier ignition of soot oxidation, by increasing the internal soot surface with opening and developing of micropores [159-161]. Moreover, previous studies [48,63,162-164] showed that the incorporation of oxygen in soot particles allowed the formation of oxygenated complexes (-C(O)) at the soot surface. Thus, the oxygen content present in soot composition provides a higher oxidation reactivity of these particles. About soot internal structure, Raman spectroscopy proved that «MD30» soot has a more ordered structure, which complicates particles oxidation. In TEM micrographs, it was observed that an increase of oxygenated compounds concentration in the biodiesel surrogate leads to the production of soot particles with a graphitic shell and a less ordered core. It is well known than

oxygen reacts easily with the amorphous structure than with the more graphitic one. However, the external structure of «MD30» particles complicates their oxidation.

Concerning the samples produced on engine bench, soot obtained through the combustion of pure biodiesel shows higher oxidation reactivity than soot obtained with conventional diesel. The maximum carbon specific oxidation rate of «B100-BM» is attained at 656°C, while 669°C is obtained for «B7-BM». Furthermore, «B100-BM» samples have a lower ignition temperature (T_{10}) than the «B7-BM» ones. These results are in good agreement with previous works, where was concluded the higher reactivity of biodiesel soot in comparison with diesel soot [48,60,63,65]. This is supported by previous results, such as TEM, Raman and elemental analysis.

Concerning CO and CO₂ emissions, “model” soot was able to produce more carbon monoxide than carbon dioxide, which shows that “model” soot oxidation leads to a less complete oxidation than the “real” one. In terms of “real” soot, a higher biodiesel content leads to a higher CO₂ formation and a more complete reaction. At the maximum emission temperature (T_m), selectivity of CO₂ for pure biodiesel soot is about 69%, while 55% is found for soot from conventional diesel. The selectivity of CO₂ formation can be explained by the oxygen present in the elemental composition of soot. Indeed, the order of soot oxygen content is the following one: «MD30» < «MD7» < «B7-BM» < «B100-BM», which corresponds to the same order of carbon dioxide selectivity.

Consequently, oxidation reactivity can be correlated with the composition and nanostructure of soot. It must be kept in mind that different properties influence particles oxidation. Concerning soot composition, oxygen, ash and SOF content play an important role. Internal structure is also a determinant factor. However, the process of particles formation and engine work conditions must be considered too. In sum, soot oxidation reactivity doesn't depend on just one property. It is based on a set of factors.

4.2.1.2 TPO in 400 ppmv NO₂ + 9% O₂/Ar

As explained in previous studies [60,73,145], an internal soot combustion is favoured in presence of O₂, while NO₂ reacts immediately at the soot surface. Thus, different oxidizing gases lead to different oxidation processes, resulting in a shift of the maximal oxidation temperature. In presence of only O₂, diffusion of the gas in solid-phase (carbon core) through the pores can difficult the soot oxidation. In the case of NO₂, a faster reaction can take place at lower temperatures.

In soot-NO₂-O₂ reaction systems, a cooperative reaction of the two gases with soot carbon allows to a better soot oxidation [73-75]. Indeed, there is a consensus on the fact that soot oxidation with NO₂ is enhanced by the presence of O₂. Thus, different C-NO₂-O₂ reaction mechanisms have been proposed so far and the specific role of the two gases in combustion of soot is still discussed.

In order to observe this cooperative action, a temperature programmed oxidation was carried out with an oxidizing mixture of 400 ppmv NO₂ + 9% O₂/Ar. [Figure 38](#) shows the evolution of the carbon specific oxidation rate in function of the temperature. Results of TPO profiles are resumed in [Table 11](#).

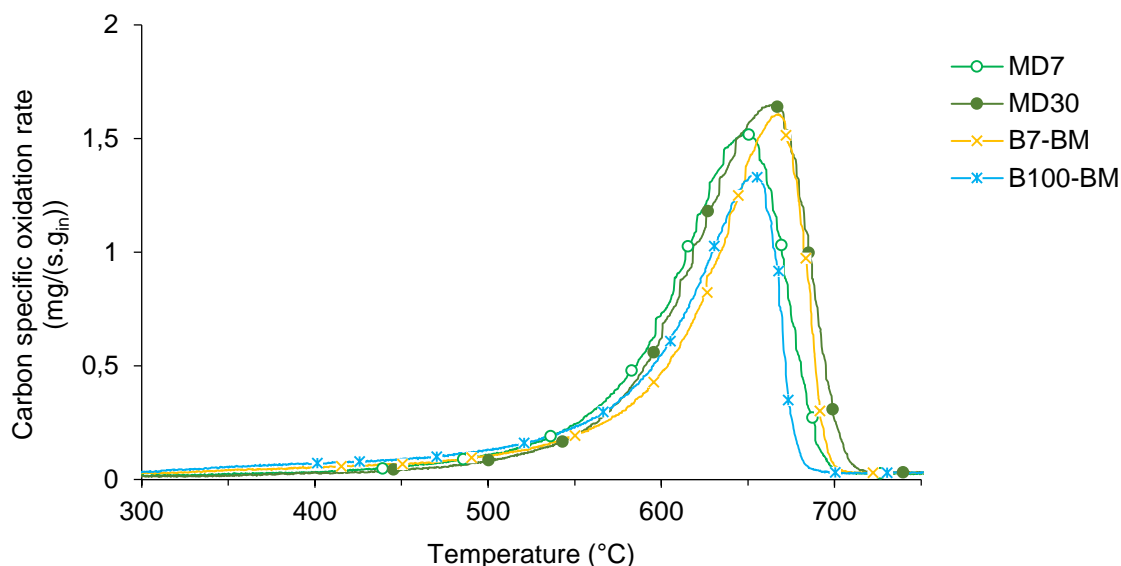


Figure 38. Carbon specific oxidation rate (mg/(s.g_{in})) of “model” and “real” soot (400 ppmv NO₂ + 9% O₂/Ar).

Table 11. Temperature programmed oxidation results in 400 ppmv NO₂ + 9% O₂/Ar.

	T _m (°C)	T ₁₀ (°C)	T ₅₀ (°C)	T ₉₀ (°C)	ΔT	S _{CO₂} (%) ¹
MD7	648	528	631	671	143	35
MD30	664	551	643	683	132	35
B7-BM	667	509	644	681	172	51
B100-BM	654	457	626	666	209	64

¹CO₂ selectivity at T_m

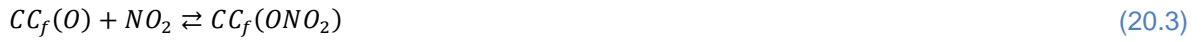
As observed during TPO experiments under O₂, soot particles reactivity decreases when the concentration of oxygenated compounds increases in the Biodiesel surrogate. T_m was attained at 648°C for «MD7» sample, while 664 °C was obtained for the «MD30» one. This reaction order was also observed in terms of T₁₀. Moreover, «B100-BM» soot seems to be more reactive than the «B7-BM» one.

Through the analysis of Figure 38 and Table 11, it can be seen that the TPO profiles and CO₂ selectivity are similar to those under O₂. In fact, no significant decrease of the maximal soot oxidation temperature (T_m) was promoted by the presence of NO₂ in the reaction gas. However, the temperature to obtain 10% of carbon conversion showed considerable modifications. For “model” soot «MD7» and «MD30», a visible increase of T₁₀ can be observed. On the contrary, “real” soot samples present lower values.

Such results reveal that NO₂ more easily promotes the oxidation of soot generated on engine bench. This behaviour can be attributed to the oxidation of the soluble organic fraction (SOF) by this gas. Mainly due to the presence of lube oils and unburned fuel, soot produced through engine combustion processes («B7-BM» and «B100-BM») contain a higher SOF content, formed on the soot particle surface, than the soot produced with the Santoro burner.

These findings are in good agreement with previous investigations. Several studies demonstrated the stronger oxidation power of NO₂ in comparison with O₂ at low temperatures (<450°C). However, high temperatures lead to the decomposition of NO₂ into NO and thereby make NO₂ lose its promoting role [76,79,86,165]. This phenomenon can explain the absence of decrease of T_m with addition of NO₂ in the reaction gas.

According to previous studies [166,167] and considering the reactivity of NO₂, it can be suggested that soot oxidation is initiated at low temperatures by NO₂ via formation of oxygen complexes on the carbon surface (20.1-20.4). In fact, although diesel soot normally contains oxygen complexes, the soot-O₂ reaction is extremely low in comparison to the soot-NO₂ one, in the normal exhaust temperature range. Thus, NO₂ initiates the creation of O-containing sites intermediates at lower temperatures, which are more reactive than the complexes that have already existed. Then, O₂ is able to react with them.



Where, CC_f represents a free carbon atom, while $CC_f(O)$ and $C(O)C_f(O)$ both are SOCs (surface oxygen complexes). Then, due to the abundance of O₂ in comparison to NO₂, this gas is expected to further react with the surface oxygen complexes originated by NO₂, yielding less stable intermediates (20.5):



$C(O)C_f(O)$ complexes, considered relatively unstable, lead to the production of CO and CO₂. They can decompose, or by thermic dissociation (20.6-20.8) or by reaction with O₂ and NO₂ (20.9-20.12). Oxygen is always in excess in a diesel exhaust, so equations 20.9 and 20.10 are predominant.



4.2.2 Catalytic soot oxidation

Diesel particulate filters are the most popular and efficient technology for soot elimination. However, the main problem resides in the reliability of the regeneration process. The high working temperatures, which are far beyond the normal diesel exhaust temperature range, represent one of the principal issues. Thus, the use of oxidative catalysts to lower the combustion temperature for soot abatement is believed to be a feasible and promising method in reducing soot emission. They lower the active regeneration temperature and allow to a certain degree of passive regeneration at suitable engine points characterized by high exhaust gas temperatures. In the present work, MnO_x-CeO_2 was selected to be investigated in soot oxidation. In [Appendix G](#), some information about these mixed oxides can be found.

4.2.2.1 TPO in 9% by volume O_2/Ar

In general, the main variables that influence the catalytic performance in soot oxidation are the soot composition, soot/catalyst ratio, type of soot-catalyst contact and the oxygen content in the feed gas [168]. An increase of the soot-catalyst ratio beyond a certain value, at which the catalyst is no longer available to meet the soot particles, results in soot oxidation at higher temperatures. More precisely, soot-catalyst ratios below 1/10 ratio do not generally influence the oxidation rate, while negative effects can be observed on catalytic activity for values above 1/5 ratio [168]. Thus, a ratio of 1/10 was chosen for the contact between soot particles and the MnO_x-CeO_2 catalyst.

The feed composition also affects the catalytic activity. Oxygen was used as reaction gas to simulate a DPF active regeneration. The oxygen concentration in the gas mixture generally varies from 5% to 21% [169-172]. Thus, a temperature programmed oxidation was carried out with an oxidizing mixture of 9% O_2/Ar , in “loose contact” conditions. [Figure 39](#) shows the evolution of the carbon specific oxidation rate in function of the temperature. [Table 12](#) displays the main results of the TPO analysis.

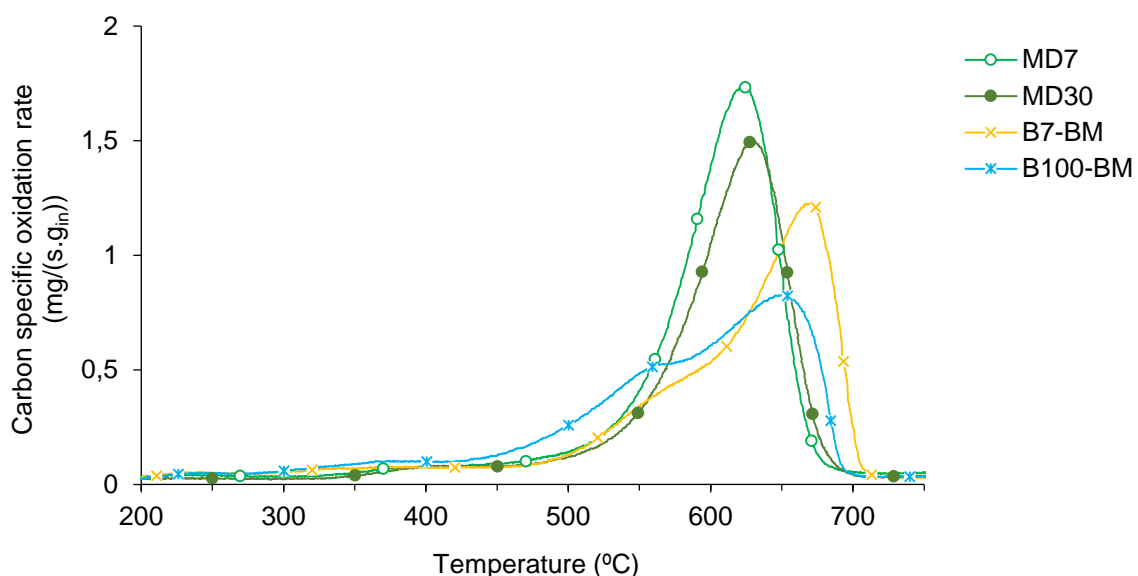


Figure 39. Carbon specific oxidation rate ($mg/(s.g_{in})$) of “model” and “real” soot in presence of MnO_x-CeO_2 mixed oxides (9% O_2/Ar), in “loose” contact conditions.

Table 12. Temperature programmed oxidation results in 9% O₂/Ar, in “loose” contact conditions.

	T _m (°C)	T ₁₀ (°C)	T ₅₀ (°C)	T ₉₀ (°C)	ΔT	S _{CO₂} (%) ¹
MD7	621	405	606	651	246	99
MD30	631	457	614	658	201	99
B7-BM	672	407	629	683	276	99
B100-BM	652	383	592	667	284	99

¹ CO₂ selectivity at T_m

The introduction of mixed oxides catalysts in the reaction bed allowed to a significant decrease of T₁₀. Furthermore, it can be observed that there is a shoulder peak at around 550°C in TPO profiles of “real” soot. This can be attributed to the oxidation of soot particles with a better contact and/or more amorphous carbon. However, the temperature of maximal oxidation rate didn’t decreased as much as expected, even if these oxides are considered good oxygen carriers.

Soot oxidation under oxygen strongly depends of soot/catalyst contact. “Loose contact” conditions are characterized by a low number of contact points between soot particles and MnO_x-CeO₂ mixed oxides. Consequently, it is expectable to have a reduced catalytic performance [173,174].

Regarding CO_x emissions, the introduction of a catalyst into the reaction bed promoted CO₂ formation from carbon oxidation instead of CO, leading to a complete reaction. Indeed, for all soot samples, a CO₂ selectivity of 99% was obtained.

Due to the low catalytic activity in soot oxidation under “loose” contact between MnO_x-CeO₂ mixed oxides and soot samples, the effect of soot-catalyst contact was evaluated through the comparison between three different contact degrees.

4.2.2.2 Effect of soot-catalyst contact

In 1996, Neeft *et al.* [175] found that the intensity of contact between soot and catalyst represents one of the major parameters that determine the soot oxidation rate. Indeed, it plays a key role in solid-solid reactions since the catalytic activity depends on the interaction between the two solids and the gas. In the literature [170,174], two types of soot-catalyst contact conditions have been reported for laboratory-scale studies. A “loose” contact is obtained by mixing the soot and the catalyst with a spatula. This procedure is sufficient to homogenize the mixture, but still allows a poor contact between the two solid phases. In fact, good contact conditions are very difficult to be reached due to the different soot and catalyst particles sizes, which clearly hinders the overall activity of the catalyst. A “tight” contact is usually prepared in a mortar to obtain, by maximizing the number of contact points, a closer contact between the two solids [172].

In a real catalytic DPF, the formation of a soot cake leads to the increase of flow pressure, which promotes the interface contact between soot and catalyst. The problem of “tight” contact is that temperatures of oxidation are usually much lower than those in a commercial diesel particulate filter. Under practical conditions, loose contact rather than tight contact is encountered [175].

In the present study, the impact of the soot-catalyst contact on soot reactivity is evaluated through the comparison of the maximal oxidation rate temperature in “loose”, “pressure” and “tight” contact

conditions. “Pressure” contact was tested to have an intermediate effect on soot oxidation, between “loose” and “tight” contact, which is believed to be closer to real conditions.

Figure 40 and Figure 41 show the evolution of the carbon specific oxidation rate in function of the temperature, for «MD30» and «B100-BM» samples, respectively. Table 13 exhibits the main results of the TPO analysis for all tested soot samples and for the three contact conditions. The results for «MD7» and «B7-BM» samples are present in Appendix H.

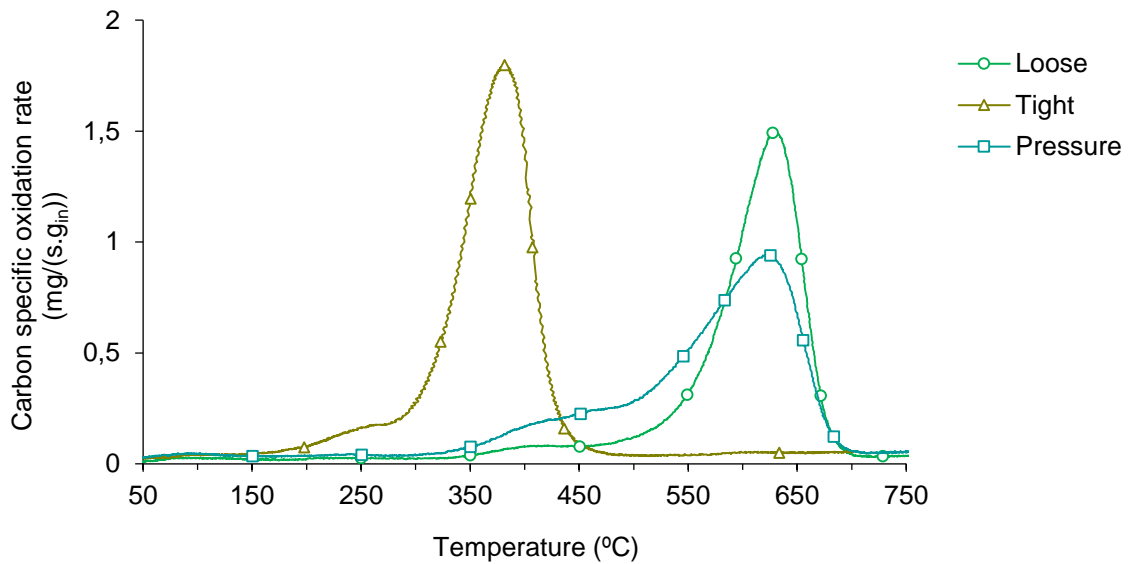


Figure 40. Carbon specific oxidation rate (mg/(s.g.in)) of «MD30» soot in presence of MnO_x-CeO_2 mixed oxides (9% O_2/Ar).

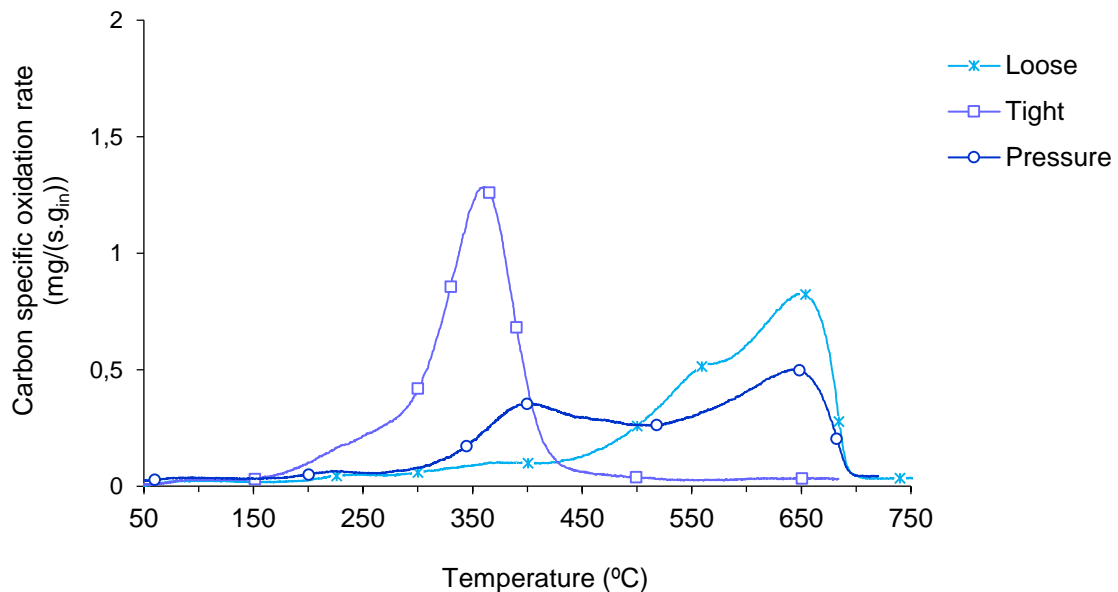


Figure 41. Carbon specific oxidation rate (mg/(s.g.in)) of «B100-BM» soot in presence of MnO_x-CeO_2 mixed oxides (9% O_2/Ar).

Table 13. Temperature programmed oxidation results in 9% O₂/Ar in presence of mixed oxides, under “loose”, “pressure” and “tight” conditions.

	Contact condition	T _m (°C)	T ₁₀ (°C)	T ₅₀ (°C)	T ₉₀ (°C)	ΔT	S _{CO₂} (%) ¹
MD7	Loose	621	405	606	651	246	99
	Pressure	592	325	566	648	323	98
	Tight	363	283	363	417	134	99
MD30	Loose	631	457	614	658	201	99
	Pressure	623	362	580	655	293	98
	Tight	382	259	372	425	166	99
B7-BM	Loose	672	407	629	683	276	99
	Pressure	662	320	505	667	347	98
	Tight	364	258	354	400	142	99
B100-BM	Loose	652	383	592	667	284	99
	Pressure	645	296	516	655	359	98
	Tight	361	246	349	408	162	99

¹ CO₂ selectivity at T_m

According to the results, it can be observed that soot oxidation temperatures are shift to much lower values and the TPO curves become narrower in “tight” contact conditions. Concerning experiments under “pressure” contact, a wider temperature window is present, with a lower reaction rate. As expected, it represents an intermediate contact condition. The two peaks shape is probably due to the heterogeneity of the soot-catalyst mixture.

An order of reactivity can be established in function of the contact conditions between soot samples and MnO_x-CeO₂ mixed oxides: “Loose” contact < “Pressure” contact < “Tight” contact. The tightness of the contact between the two solids and therefore, the number of contact points, is a critical factor for the enhancement of catalytic soot oxidation. From “loose” contact to “tight” contact conditions, the temperature of maximal soot oxidation rate is decreased of, at least, 250°C.

The interface between the two solids is limited by the contact points between larger soot particles and larger clusters of catalyst particles [176,177]. Since the action of the catalyst on carbon oxidation is mainly linked to the proximity of the carbon active sites to those of the catalyst and to the number of active sites accessible for the reaction gas, “loose” contact conditions provide a higher interfacial area between the two solids and a reduced catalytic activity.

Regarding CO_x emissions, the presence of a catalyst, independently of the contact conditions, leads to a residual emission of carbon monoxide. For all soot samples and for all contact conditions, the selectivity of CO₂ is between 98 and 99%.

4.2.2.3 TPO in 400 ppmv NO₂ + 9% O₂/Ar

In order to observe both catalytic and NO₂ effect on soot oxidation, TPO experiments were carried out under 400 ppmv NO₂ + 9% O₂/Ar, where “loose” contact was promoted between soot particles and MnO_x-CeO₂ mixed oxides. Figure 42 shows the evolution of carbon specific oxidation rate in function of the temperature, for «MD30» and «B100-BM» samples. In Table 14, the main results of TPO profiles are resumed.

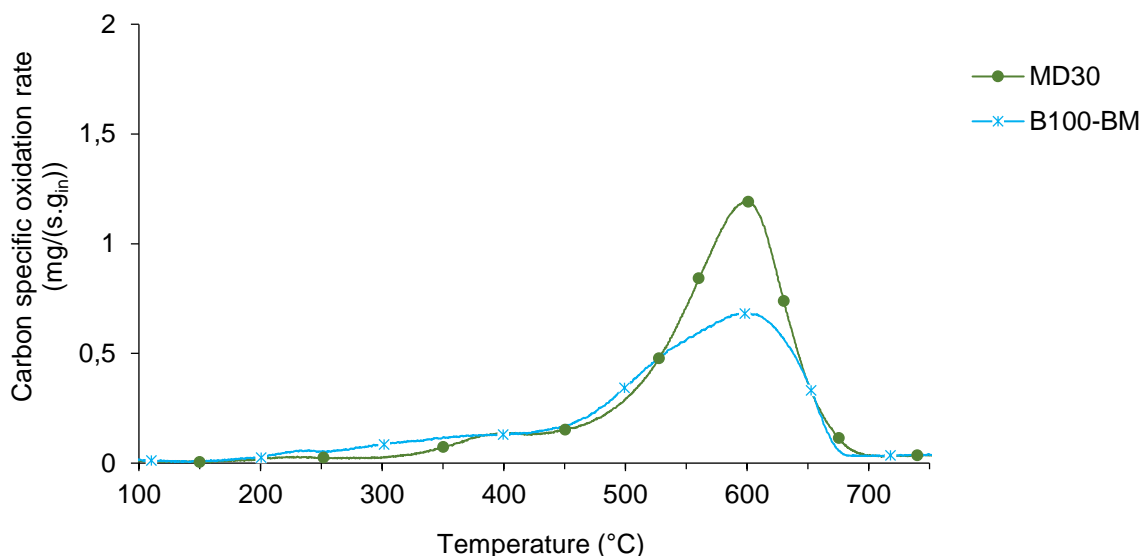


Figure 42. Carbon specific oxidation rate (mg/(s.g.in)) of «MD30» and «B100-BM» soot samples in presence of MnO_x-CeO₂ mixed oxides (400 ppmv NO₂ + 9% O₂/Ar).

Table 14. Temperature programmed oxidation results in 400 ppmv NO₂ + 9% O₂/Ar, in “loose” contact conditions.

	T _m (°C)	T ₁₀ (°C)	T ₅₀ (°C)	T ₉₀ (°C)	ΔT	S _{CO₂} (%) ¹
MD30	598	433	580	641	208	99
B100-BM	599	349	558	642	293	98

¹CO₂ selectivity at T_m

An obvious decrease of oxidation temperatures can be observed, in comparison with the results obtained without the presence of NO₂. As already mentioned, nitrogen dioxide represents a stronger oxidizing gas than O₂. However, it was found that without a catalyst, the introduction of NO₂ into the gaseous mixture didn't cause a significative decrease of soot oxidation temperature. In fact, soot particles oxidation strongly depends on NO₂ concentration. Consequently, in absence of a catalyst, 400 ppmv of this gas are not able to make the whole TPO profiles shift considerably to lower temperatures.

These results prove that the presence of MnO_x-CeO₂ mixed oxides in the reaction bed effectively enhances the oxidation reactivity of soot under both O₂ and NO₂+O₂. It has been reported that MnO_x-CeO₂ mixed oxides are excellent oxygen storage materials. They can transfer oxygen in gas phase into active species (O_{cat}^{*}) and then use them for soot oxidation.

To better visualize the advantage of using NO₂ and/or a catalyst, Figure 43 shows T₁₀ and T_m values of catalytic and non-catalytic soot oxidation, under O₂ and O₂+NO₂.

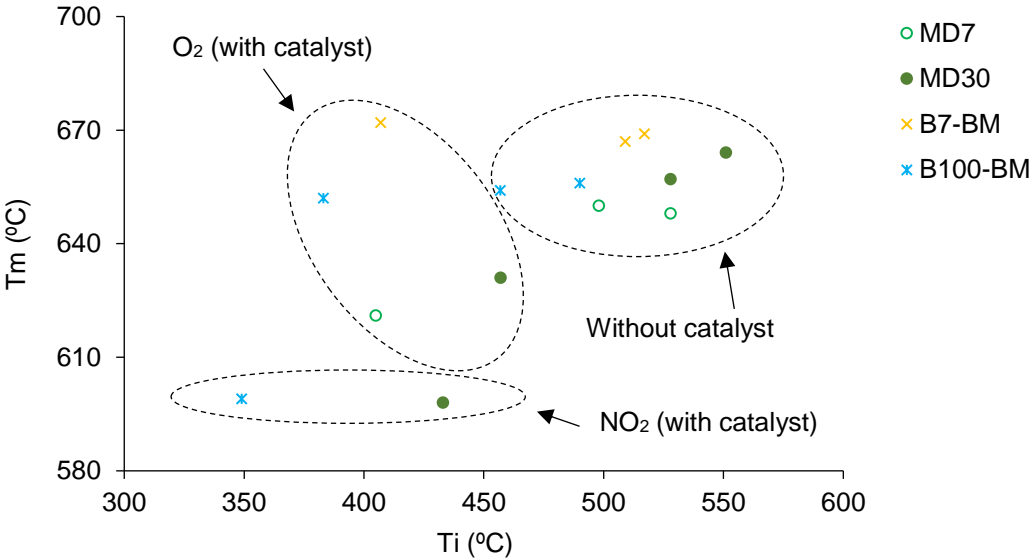


Figure 43. T₁₀ and T_m values of soot oxidation.

THIS PAGE WAS INTENTIONALLY LEFT BLANK

5 Conclusion

The aim of this study was to widen the current knowledge about soot. Therefore, the physico-chemical characteristics of different soot samples and their oxidation reactivity, under different reaction gases, and in presence or not of a catalyst, were determined. The samples were collected from two different systems. One of them consisted on an academic burner (Santoro-type), under atmospheric pressure, with a diffusion flame. The other one was an engine bench (from Renault-Volvo Trucks), working with a low loading cycle, at low temperatures, which is representative of very severe cold real drive cycles. The first class was classified as “model” soot, obtained through the combustion of diesel and biodiesel surrogates. The second one was called “real” soot, from diesel and biodiesel fuel.

The first part of this study consisted on the characterization of the different studied soot samples. The tested oxygenated compounds were methyl butanoate, methyl octanoate and methyl decanoate. The surrogates contained 7% or 30% of these additives. The properties and reactivity of “model” particles were compared with those of “real” ones. The impact of methyl ester-based oxygenated compounds concentration and the length of their carbon chain on soot characteristics was evaluated.

The laser diffraction analysis allowed to measure the particles mean granulometry. It was deduced that the presence of oxygenated compounds with a higher concentration and/or carbon chain length leads to the production of smaller particles. Indeed, «MD30» particles presented the smaller mean size. Furthermore, elemental and Raman analyses proved that «MD30» soot had the smallest oxygen and SOF content and a more ordered structure. TEM measurements showed that the mean carbon fringe length increases with the ester chain length but decreases with the biodiesel content. In sum, all these tests showed that the structure and composition of soot depend on the fuel nature.

The DPF regeneration performance was also assessed in terms of concentration of such compounds. Therefore, the second part consisted in oxidation experiments (TPO) under O_2 and O_2+NO_2 . «MD7» and «MD30» samples were used to represent the “model” soot. In general, it was deduced that the reactivity of soot particles decreases when the concentration of oxygenated compounds in the surrogate increases. Furthermore, in terms of “real” soot, biodiesel particles were more reactive than the diesel ones.

The impact of the reaction gas on soot oxidation was also determined. No significant decrease of the maximal soot oxidation temperature was promoted by the presence of NO_2 , due to the degradation of this gas into NO at elevated temperatures. However, the temperature to obtain 10% of carbon conversion showed considerable modifications. This temperature decreased in the case of “real” soot, probably due to the oxidation of the soluble organic fraction (SOF) by this gas.

Finally, the interaction between mixed oxides and soot, under different reaction gases and different contact conditions was tested. The presence of MnO_x-CeO_2 mixed oxides facilitated the reaction at lower temperatures and led to a complete soot oxidation, with a CO_2 selectivity of almost 100%. In addition, three contact conditions were tested and compared. As expected, due to the tightness of the contact between soot and the catalyst, oxidation under “tight” contact conditions allowed to a decrease of the temperature of maximal soot oxidation rate about, at least, 250°C.

To conclude, it was proved that the properties and characteristics of soot can give some information and be correlated with the oxidation reactivity. Furthermore, despite some differences, it can be considered that with the experimental installation used to produce “model” soot, it is possible to generate particles with properties close to those of “real” ones. Thus, “model” soot can be considered as representative of soot produced under real driving conditions and be used for further studies. However, numerous improvements should be made to better understand to soot formation and oxidation process.

6 Future perspectives

Based on the results and conclusions achieved through this work, there are some aspects which future study may be of interest.

1. X-ray diffraction (XRD) analysis, to obtain a quantitative analysis of the graphitization degree and therefore, to better correlate soot structure with oxidation reactivity.
2. TPO experiments under pure NO_2 , in presence or not of catalyst.
3. TPO experiments under $\text{NO}+\text{O}_2$, in presence of catalyst, to understand the interaction between NO and the catalyst surface.
4. DRIFT spectroscopy analysis, to identify the intermediates formed during soot oxidation. Thus, role of NO_2 , NO and O_2 in soot oxidation can be identified and the mechanism can be confirmed.
5. BET experiments, to do a surface area analysis and to do a correlation between the oxidation reactivity and surface area.
6. Improvement of the experimental device used to produce and collect the tested “model” soot, to work under moderated pressure (1-10 bar). It would allow to get closer to the real process of soot production and therefore, to evaluate the impact of pressure on the formation, physico-chemical properties and reactivity of particles. In fact, this device is currently being improved. [Figure 44](#) shows the general view of the combustion chamber, built for non-premixed diffusion flames studies, under pressure.



Figure 44. Santoro-type burner, at moderated pressure.

7. Improvement of the experimental device with collection of soot samples at different heights of the flame and analysis of samples composition and structure.
8. Impregnation of alkali metals (Na , K , ...) on “model” soot, in order to study their impact on soot properties and oxidation reactivity. In real conditions, such inorganic compounds can come from

NaOH and KOH catalysts, used during the production of biodiesel. Furthermore, soot can also contain other elements, coming from lubricant oils in diesel engines, such as Ca, Zn, Fe and Mg. It should be interesting to evaluate the impact of each compound on soot reactivity.

9. X-ray photoelectron spectroscopy (XPS), to identify and quantify trace elements and carbon oxidation state (oxygen functional groups, to identify the degree of oxidation).
10. Impregnation of platinum or palladium in the mixed oxides structure, to observe its promotion on NO oxidation activity. The main oxidation function of such metals is indirect by converting NO to NO₂.

7 References

- [1] EIA, "International Energy Outlook 2017 Overview", *U. S. Energy Inf. Adm.*, **2017**, IEO2017: pp. 143.
- [2] *Explaining road transport emission*, European Environment Agency, Copenhagen, **2016**.
- [3] P. T. O. Shaughnessy, "Occupational health risk to nanoparticulate exposure", *Environ. Sci. : Processes Impacts*, **2013**,15, pp. 49-62.
- [4] L. Coniglio, H. Bennadji, P. A. Glaude, O. Herbinet, and F. Billaud, "Combustion chemical kinetics of biodiesel and related compounds (methyl and ethyl esters): Experiments and modeling e Advances and future refinements," *Prog. Energy Combust. Sci.*, **2013**, 39(4), pp. 340–382.
- [5] National emissions reported to the UNFCCC and to the EU Greenhouse Gas Monitoring Mechanism provided by European Environment Agency (EEA), **2017** - *European Environment Agency*, February 2018, www.eea.europa.eu
- [6] Heavy-Duty Emissions, February 2018, <https://www.transportpolicy.net/topic/emissions-standards/>
- [7] M. Lapuerta, O. Armas and J. Rodríguez-Fernández, "Effect of biodiesel fuels on diesel engine emissions," *Progress in Energy and Combustion Science*, **2008**, 34(2), pp. 198-223.
- [8] C. Escobar, E. S. Lora, O. J. Venturini, E. E. Yáñez, E. F. Castillo and O. Almazan, "Biofuels : Environment , technology and food security," *Renewable and Sustainable Energy Reviews*, **2009**, 13(6-7), pp. 1275-1287.
- [9] A. K. Agarwal, "Biofuels (alcohols and biodiesel) applications as fuels for internal combustion engines," *Prog. Energy Combust. Sci.*, **2007**, 33(3), pp. 233-271.
- [10] A. Demirbas, "Progress and recent trends in biofuels," *Prog. Energy Combust. Sci.*, **2007**, 33(1), pp. 1-18.
- [11] "DIRECTIVE 2009/28/EC OF THE EUROPEAN PARLIAMENT AND OF THE COUNCIL of 23 April 2009", *Official Journal of the European Union*, <https://eur-lex.europa.eu/legal-content/EN/TXT/PDF/?uri=CELEX:32009L0028&from=EN>
- [12] "DIRECTIVE 2009/30/EC OF THE EUROPEAN PARLIAMENT AND OF THE COUNCIL of 23 April 2009", *Official Journal of the European Union*, <http://eur-lex.europa.eu/legal-content/EN/TXT/PDF/?uri=CELEX:32009L0030&from=EN>
- [13] "Proposal for a DIRECTIVE OF THE EUROPEAN PARLIAMENT AND OF THE COUNCIL amending Directive 98/70/EC relating to the quality of petrol and diesel fuels and amending Directive 2009/28/EC on the promotion of the use of energy from renewable sources", <http://eur-lex.europa.eu/LexUriServ/LexUriServ.do?uri=COM:2012:0595:FIN:En:PDF>
- [14] "The current status of biofuels in the European Union, their environmental impacts and future prospects", European Academies – Science Advisory Council, 2012, Germany, https://www.easac.eu/fileadmin/PDF_s/reports_statements/Easac_12_Biofuels_Complete.pdf
- [15] R. J. Santoro, H. G. Semerjian, and R. A. Dobbins, "Soot Particle Formation in Diffusion Flames," *Combust. Flame*, **1987**, pp. 513-523.

- [16] U. Schuchardt, R. Sercheli, and R. M. Vargas, "Transesterification of Vegetable Oils : a Review General Aspects of Transesterification Transesterification of Vegetable Oils Acid-Catalyzed Processes Base-Catalyzed Processes," *J. Braz. Chem. Soc.*, **1998**, 9(1), pp. 199-210.
- [17] J. M. N. Van Kasteren and A. P. Nisworo, "A process model to estimate the cost of industrial scale biodiesel production from waste cooking oil by supercritical transesterification," *Resour. Conserv. Recycl.*, **2007**, 50(4), pp. 442-458.
- [18] J. Xue, T. E. Grift, and A. C. Hansen, "Effect of biodiesel on engine performances and emissions," *Renewable and Sustainable Energy Reviews*, **2011**, 15(2), pp. 1098-1116.
- [19] H. Aydin and H. Bayindir, "Performance and emission analysis of cottonseed oil methyl ester in a diesel engine", *Renewable Energy*, **2010**, 35(3), pp. 588-592.
- [20] O. Armas, K. Yehliu and A. L. Boehman, "Effect of alternative fuels on exhaust emissions during diesel engine operation with matched combustion phasing", *Fuel*, **2010**, 89(2), pp. 438-456.
- [21] H. Hazar, "Effects of biodiesel on a low heat loss diesel engine", *Renewable Energy*, **2009**, 34(6), pp. 1533-1537.
- [22] S. Murillo, J. L. Míguez, J. Porteiro, E. Granada, J. C. Mórán, "Performance and exhaust emissions in the use of biodiesel in outboard diesel engines", *Fuel*, **2007**, 86(12-13), pp. 1765-1771.
- [23] S. Kent Hoekman, Curtis Robbins, "Review of the effects of biodiesel on NOx emissions", *Fuel Processing Technology*, **2012**, 96, pp. 237-249.
- [24] C.D. Rakopoulos, D.C. Rakopoulos, D.T. Hountalas, E.G. Giakoumis, E.C. Andritsakis, "Performance and emissions of bus engine using blends of diesel fuel with bio-diesel of sunflower or cottonseed oils derived from Greek feedstock", *Fuel*, **2008**, 87(2), pp.147-157.
- [25] A. L. Boehman, J. Song, and M. Alam, "Impact of Biodiesel Blending on Diesel Soot and the Regeneration of Particulate Filters", *Energy & Fuels*, **2005**, 19, pp. 1857-1864.
- [26] W. G. Wang, D. W. Lyons, N. N. Clark, and M. Gautam, "Emissions from Nine Heavy Trucks Fueled by Diesel and Biodiesel Blend without Engine Modification", *Environmental Science & Technology*, **2000**, 34, pp. 933-939.
- [27] M. S. Graboski and R. L. McCormick, "Combustion of fat and vegetable oil derived fuels in diesel engines", *Progress in Energy and Combustion Science*, **1998**, 24(2), pp. 125-164.
- [28] C. Y. Choi and R. D. Reitz, "Experimental study on the effects of oxygenated fuel blends and multiple injection strategies on DI diesel engine emissions," *Fuel*, **1999**, 78(11), pp. 1303-1317.
- [29] C. D. Rakopoulos, D. C. Rakopoulos, D. T. Hountalas, E. G. Giakoumis, and E. C. Andritsakis, "Performance and emissions of bus engine using blends of diesel fuel with bio-diesel of sunflower or cottonseed oils derived from Greek feedstock," *Fuel*, **2008**, 87(2), pp. 147-157.
- [30] M. Cardone, M. V. Prati, V. Rocco, M. Seggiani, A. Senatore, and S. Vitolo, "Brassica carinata as an alternative oil crop for the production of biodiesel in Italy: Engine performance and regulated and unregulated exhaust emissions," *Environmental Science & Technology*, **2002**, 36(21), pp. 4656-4662.
- [31] K. Schmidt, J. Van Gerpen, "The Effect of Biodiesel Fuel Composition on Diesel Combustion and Emissions", *SAE Technical Paper*, **1996**.
- [32] P. F. Flynn *et al.*, "Diesel Combustion: An Integrated View Combining Laser Diagnostics, Chemical Kinetics, And Empirical Validation," *SAE Technical Paper*, **1999**.

- [33] C. Mueller, W. Pitz, L. Pickett, G. Martin et al., “ Effects of Oxygenates on Soot Processes in DI Diesel Engines: Experiments and Numerical Simulations”, *SAE Technical Paper*, **2003**.
- [34] M. Kampa and E. Castanas, “Human health effects of air pollution,” *Environmental Pollution*, **2008**, 151(2), pp. 362-367.
- [35] I. Glassman, “Sooting laminar diffusion flames: Effect of dilution, additives, pressure, and microgravity”, *Symposium (International) on Combustion*, **1998**, 27(1), pp. 1589-1596.
- [36] W. Kim, C. M. Sorensen, D. Fry, A. Chakrabarti, “Soot aggregates, superaggregates and gel-like networks in laminar diffusion flames”, *Journal of Aerosol Science*, **2006**, 37(3), pp. 386-401.
- [37] I. M. Kennedy, “Models of soot formation and oxidation”, *Progress in Energy and Combustion Science*, **1997**, 23(2), pp. 95-132.
- [38] J. Pagels, “Fine and Ultrafine Particles from Combustion Sources - Investigations with In-situ Techniques”, PhD Thesis, Lund Institut of Technology, **2015**.
- [39] M. Kholghy, M. Saffaripour, C. Yip, M. J. Thomson, “The evolution of soot morphology in a laminar coflow diffusion flame of a surrogate for Jet A-1”, *Combustion and Flame*, **2013**, 160(10), pp. 2119-2130.
- [40] H. Richter, J.B. Howard,” Formation of polycyclic aromatic hydrocarbons and their growth to soot—a review of chemical reaction pathways”, *Progress in Energy and Combustion Science*, **2000**, 26(4-6), pp. 565-608.
- [41] H. GG. Wagner, “Soot formation in combustion”, *Symposium (International) on Combustion*, **1979**, 17(1), pp.3-19.
- [42] I. Glassman, “Soot formation in combustion processes”, *Symposium (International) on Combustion*, **1989**, 22(1), pp. 295-311.
- [43] S. Mohankumara, P. Senthilkumarb, “Particulate matter formation and its control methodologies for diesel engine: A comprehensive review”, *Renewable and Sustainable Energy Reviews*, **2017**, 80, pp. 1227-238.
- [44] S. J. Harris and A. M. Weiner, “Surface growth of soot particles in premixed Ethylene/ Air Flames”, *Combustion Science and Technology*, **1983**, 31(3-4), pp. 155-167.
- [45] J. Lahaye, “Particulate carbon from the gas phase”, *Carbon*, **1992**, 30(3), pp. 309-314.
- [46] H. Bockhorn, “Soot formation in combustion, mechanisms and models”, Springer-Verlag, Berlin, **1994**.
- [47] Th. Henning and F. Salama, “Carbon in the Universe”, *Science ´s Compass – Review: Carbon*, **1998**, 282.
- [48] J. Song, M. Alam, A. Boehman, “Impact of alternative fuels on soot properties and DPF regeneration”, *Combustion Science and Technology*, **2007**, 179(9), pp. 1991-2037.
- [49] S. Collura, N. Chaoui, B. Azambre, G. Fingueneisel, O. Heintz, A. Krzton et al., “Influence of the soluble organic fraction on the thermal behaviour, texture and surface chemistry of diesel exhaust soot”, *Carbon*, **2005**, 43(3), pp.605-613.
- [50] E. Bocci and L. Rambaldi, “Soot Emission Modelization of a Diesel Engine from Experimental Data”, *International Conference on Computational Science and Its Applications (ICCSA 2011), Part IV, LNCS 6785*, **2011**, pp. 316-327.

- [51] M.V. Twigg and P. R. Phillips, "Cleaning the Air We Breathe – controlling Diesel Particulate Emissions from Passenger Cars", *Platinum Metals Review*, **2009**, 53(1), pp.27-34.
- [52] A. Sadezky, H. Muckenhuber, H. Grothe, R. Niessner, and U. Poschl, "Raman microspectroscopy of soot and related carbonaceous materials: Spectral analysis and structural information", *Carbon*, **2005**, 43(8), pp. 1731-1742.
- [53] M. Alfè, B. Apicella, R. Barbella, J.-N. Rouzaud, A. Tregrossi, and A. Ciajolo, "Structure-property relationship in nanostructures of young and mature soot in premixed flames," *Proceedings of the Combustion Institute*, **2009**, 32(1), pp. 697-704.
- [54] T. Ishiguro, N. Suzuki, Y. Fujitani, and H. Morimoto, "Microstructural Changes of Diesel Soot During Oxidation," *Combustion and Flame*, **1991**, 85(1-2), pp. 1-6.
- [55] H. Omidvarborna, A. Kumar and D-S. Kim, "Recent studies on soot modeling for diesel combustion", *Renewable and Sustainable Energy Reviews*, **2015**, 48, pp. 635-647.
- [56] N. M. Laurendeau, "Heterogeneous kinetics of coal char gasification and combustion," *Progress in Energy and Combustion Science*, **1978**, 4(4), pp. 221-270.
- [57] R.L. Vander Wal, A. J. Tomasek, "Soot oxidation: dependence upon initial nanostructure", *Combustion and Flame*, **2003**, 134(1-2), pp. 1-9.
- [58] J.-O. Müller, D. S. Su, R. E. Jentoft, U. Wild, and R. Schlögl, "Diesel Engine Exhaust Emission: Oxidative Behavior and Microstructure of Black Smoke Soot Particulate", *Environmental Science and Technology*, **2006**, 40(4), pp.1231-1236.
- [59] Z. Du, "Kinetic Modeling of Carbon Oxidation", PhD Thesis, Massachusetts Institute of Technology, **1990**.
- [60] J. Song, M. Alam, A. L. Boehman, U. Kim, "Examination of the oxidation behavior of biodiesel soot", *Combustion and Flame*, **2006**, 146(4), pp.589-604.
- [61] R.L. Vander Wal, A. J. Tomasek, "Soot nanostructure: dependence upon synthesis conditions", *Combustion and Flame*, **2004**, 136(1-2), pp.129-140.
- [62] A. Liati, A. Spiteri, P. D. Eggenschwiler, N. Vogel- Schäuble, "Microscopic investigation of soot and ash particulate matter derived from biofuel and diesel: implications for the reactivity of soot", *Journal of Nanoparticle Research*, **2012**, 14, pp. 1224-1242.
- [63] H. J. Seong, A. L. Boehman, "Studies of soot oxidative reactivity using a diffusion flame burner", *Combust and Flame*, **2012**, 159(5), pp.1864-1875.
- [64] E. J. Barrientos, M. M. Maricq, J. E. Anderson, "Impact of ester structures on the soot characteristics and soot oxidative reactivity of biodiesel", *SAE Technical Paper*, **2015**.
- [65] M. N. Ess, H. Bladt, W. Mühlbauer, S. I. Seher, C. Zöllner, S. Lorenz et al., "Reactivity and structure of soot generated at varying biofuel content end engine operating parameters", *Combustion and Flame*, **2016**, 163, pp. 157-159.
- [66] A. Cavaliere, R. Barbella, A. Ciajolo, A. D'anna, R. Ragucci, "Fuel and soot oxidation in diesel-like conditions", *Symposium (International) on Combustion*, **1994**, 25(1), pp. 167-174.
- [67] P. Roth, T. Eckhardt, B. Franz and J. Patschull, "H₂O₂-Assisted Regeneration of Diesel Particulate Traps at Typical Exhaust Gas Temperatures", *Combustion and Flame*, **1998**, 115, pp. 28-37.

- [68] B. S. Haynes, "A turnover model for carbon reactivity I. Development", *Combustion and Flame*, **2001**, 126, pp. 1421-1432.
- [69] S. Ahmed and M. H. Back, "A Kinetic Model for the Low Temperature Oxidation of Carbon: I", *Combustion and Flame*, **1987**, 70, pp. 1-16.
- [70] P. Campbell and R. Mitchell, "The impact of the distributions of surface oxides and their migration on characterization of the heterogeneous carbon-oxygen reaction," *Combustion and Flame*, **2008**, 154, pp. 47-66.
- [71] J. P. Neeft, X. Nijhuis, E. Smakman, M. Makkee, and J. A. Moulijn, "Kinetics of the oxidation of diesel soot," *Fuel*, **1997**, 76(12), pp. 1129-1136.
- [72] A. Yezerets, N. W. Currier, H. A. Eadler, A. Suresh, P. F. Madden, and M. A. Branigin, "Investigation of the oxidation behavior of diesel particulate matter," *Catalysis Today*, **2003**, 88(1-2), pp. 17-25.
- [73] C. J. Tighe, M. V. Twigg, A. N. Hayhurst, J. S. Dennis, "The kinetics of oxidation of Diesel soots and a carbon black (Printex U) by O₂ with reference to changes in both size and internal structure of the spherules during burnout", *Carbon*, **2016**, 107, pp. 20-35.
- [74] F. Jacquot, V. Logie, J. F. Brilhac and P. Gilot, "Kinetics of the oxidation of carbon black by NO₂: Influence of the presence of water and oxygen ", *Carbon*, **2002**, 40(3), pp.335-343.
- [75] M. Jeguirim, V. Tschamber, J.F. Brilhac and P. Ehrburger, "Oxidation mechanism of carbon black by NO₂: Effect of water vapour", *Fuel*, **2005**, 84, pp. 1949-1956.
- [76] A. Setiabudi, BAAL. van Setten, M. Makkee, J. A. Moulijn, "The influence of NO_x on soot oxidation rate: molten salt versus platinum", *Applied Catalysis B: Environmental*, **2002**, 35(3), pp.159-166.
- [77] B. R. Stanmore, J-F. Brilhac, P. Gilot, "The oxidation of soot: a review of experiments, mechanisms and models", *Carbon*, **2001**, 39(15), pp.2247-2268.
- [78] P. Ciambelli, V. Palma, P. Russo, S. Vaccaro, "The role of NO in the regeneration of catalytic ceramic filters for soot removal from exhaust gases", *Catalysis Today*, **2000**, 60(1-2), pp.43-49.
- [79] K.-Y. Choi, N. W. Cant, and D. L. Trimm, "Gasification of carbonaceous particulates," *Journal of Chemical Technology & Biotechnology*, **1998**, 71(1), pp. 57-60.
- [80] FPT Powertrain Technologies, April 2018,
<http://www.fptindustrial.com/global/fr/technologies/euro-vi-hi-escr>
- [81] V. Palma, P. Ciambelli, E. Meloni, A. Sin, "Study of the catalyst load for a microwave susceptible catalytic DPF", *Catalysis Today*, **2013**, 216, pp.185-193.
- [82] C. Benaqqa, M. Gomina, A. Beurotte, M. Boussuge et al., "Morphology, physical, thermal and mechanical properties of the constitutive materials of diesel particulate filters", *Applied Thermal Engineering*, **2014**, 62(2), pp.599-606.
- [83] J. Rodríguez-Fernandez, M. Lapuerta, J. Sanchez-Valdepenas, "Regeneration of diesel particulate filters: Effect of renewable fuels", *Renewable Energy*, **2017**, 104, pp. 30-39.
- [84] D. Fino, V. Specchia, "Open issues in oxidative catalysis for diesel particulate abatement", *Powder Technology*, **2008**, 180, pp. 64-73.

- [85] M. J. Lázaro, M. E. Gálvez, A. Boyano, S. Ascaso, I. Suelves, R. Moliner, I. Pieta, C. Herrera, M. A. Larrubia, L. J. Alemany, "Catalytic Technologies for Diesel Engines Exhaust Gas Cleaning", *Catalysis: Principles, Types and Applications*, **2011**, Chapter 6.
- [86] B. A. A. L. Van Setten, M. Makkee and J. A. Moulijn, "Science and technology of catalytic diesel particulate filters", *Catalysis Reviews – Science and Engineering*, **2001**, 43(4), pp.489-564.
- [87] A-M. Stamatellou, A. Stamatelos, "Overview of Diesel particulate filter systems sizing approaches", *Applied Thermal Engineering*, **2017**, 121, pp. 537-546.
- [88] M. Lapuerta, J. Rodríguez-Fernández, F. Oliva, "Effect of soot accumulation in a diesel particle filter on the combustion process and gaseous emissions", *Energy*, **2012**, 47(1), pp.543-552.
- [89] B. J. Cooper, and J. E. Thoss, "Role of NO in diesel particulate emission control", *SAE Technical paper*, **1989**.
- [90] R. Allansson, P. Blakeman, B. Cooper, H. Hess *et al.*, "Optimizing the Low Temperature Performance and Regeneration Efficiency of the Continuously Regenerating Diesel Particulate Filter (CR-DPF) System", *SAE Technical Paper*, **2002**.
- [91] S. Andersson, C. Akerlund, M. Blomquist, "Low pressure EGR calibration strategies for reliable diesel particulate filter regeneration on HDD engines", *SAE Technical Paper*, **2002**.
- [92] O. Salvat, P. Marez, G. Belot, "Passenger car serial application of a particulate system on a common rail direct injection diesel engine", *SAE Technical Paper*, **2000**.
- [93] K. Chen, K.S. Martirosyan, D. Luss, "Transient temperature rise during regeneration of diesel particulate filters", *Chemical Engineering Journal*, **2011**, 176-177, pp.144-150.
- [94] M.A. Mokhri, N.R. Abdullah, S.A. Abdullah, S. Kasalong, R. Mamat, "Soot filtration recent simulation analysis in diesel particulate filter", *Procedia Engineering*, **2012**, 41, pp. 1750-1755.
- [95] V. Palma, P. Ciambelli, E. Meloni, A. Sin, "Catalytic DPF microwave assisted active regeneration", *Fuel*, **2015**, 140, pp. 50-61.
- [96] H. Muroyama, S. Hano, T. Matsui, K. Eguchi, "Catalytic soot combustion over CeO₂-based oxides", *Catalysis Today*, **2010**, 153(3-4), pp. 133-135.
- [97] F. Lin, X.D. Wu, S. Liu, D. Weng, Y.Y. Huang, "Preparation of MnO_x-CeO_x-Al₂O₃ mixed oxides for NO_x-assisted soot oxidation: Activity, structure and thermal stability", *Chemical Engineering Journal*, **2013**, 226, pp.105-112.
- [98] H.L. Zhang, Y. Zhu, S.D. Wang, M. Zhao, M.C. Gong, Y.Q. Chen, "Activity and thermal stability of Pt/Ce_{0.64}Mn_{0.16}R_{0.2}O_x (R = Al, Zr, La, or Y) for soot and NO oxidation", *Fuel Processing Technology*, **2015**, 137, pp. 38-47.
- [99] A. Bueno-López, K. Krishna, M. Makkee and J.A. Moulijn, "Active oxygen from CeO₂ and its role in catalysed soot oxidation", *Catalysis Letters*, **2005**, 99(3-4), pp. 203-205.
- [100] D. Devaiah, T. Tsuzuki, C.U. Aniz, B.M. Reddy, "Enhanced CO and soot oxidation activity over Y-doped ceria-zirconia and ceria-lanthana solid solutions", *Catalysis Letters*, **2015**, 145(5), pp. 1206-1216.
- [101] P. Darcy, "Modélisation du fonctionnement d'un filtre à particules catalysé", PhD Thesis, Université Pierre et Marie Curie (Paris VI), **2005**.

- [102] T. V. Choudhary, S. Banerjee, V. R. Choudhary, "Catalysts for combustion of methane and lower alkanes", *Applied Catalysis A: General*, **2002**, 234(1-2), pp. 1-23.
- [103] G. Pecchi, P. Reyes, T- López and R. Gómez, « Pd-CeO₂ and Pd-La₂O₃/alumina-supported catalysts: their effect on the catalytic combustion of methane", *Journal of Non-Crystalline Solids*, **2004**, 345-346, pp.624-627.
- [104] P. Gélin, M. Primet, "Complete oxidation of methane at low temperature over noble metal based catalysts: a review", *Applied Catalysis B: Environmental*, **2002**, 39(1), pp.1-37.
- [105] W.J. Shan, N. Ma, J.L. Yang, X.D. Wu, C. Liu, L.L. Wei, "Catalytic oxidation of soot particulates over MnO_x-CeO₂ oxides prepared by complexation-combustion method", *Journal of Natural Gas Chemistry*, **2010**, 19(1), pp. 86-90.
- [106] X.D. Wu, F. Lin, H.B. Xu, D. Weng, "Effects of absorbed and gaseous NO_x species on catalytic oxidation of diesel soot with MnO_x-CeO₂ mixed oxides", *Applied Catalysis B: Environmental*, **2010**, 96(1-2), pp. 101-109.
- [107] L. Xueting, L. Shujun, H. Hui, W. Zeng, W. Junliang, C. Limin, Y. Daiqi, F. Mingli, "Evolution of oxygen vacancies in MnO_x-CeO₂ mixed oxides for soot oxidation", *Applied Catalysis B: Environmental*, **2018**, 223, pp. 91-102.
- [108] X. Wu, F. Lin, H. Xu, D. Weng, "Effects of adsorbed and gaseous NO_x species on catalytic oxidation of diesel soot with MnO_x-CeO₂ mixed oxides", *Applied Catalysis B: Environmental*, **2010**, 96(1-2), pp. 101-109.
- [109] M. M. Fiuk, A. Adamski, "Activity of MnO_x-CeO₂ catalysts in combustion of low concentrated methane", *Catalysis Today*, **2015**, 257(1), pp. 131-135.
- [110] K. Tikhomirov, O. Kröcher, M. Elsener, AA. Wokaun, "MnO_x-CeO₂ mixed oxides for the low-temperature oxidation of diesel soot", *Applied Catalysis B: Environmental*, **2006**, 64(1-2), pp. 72-78.
- [111] A. Setiabudi, J.L. Chen, G. Mul, M. Makkee, J.A. Moulijn, "CeO₂ catalysed soot oxidation. The role of active oxygen to accelerate the oxidation conversion", *Applied Catalysis B: Environmental*, **2004**, 51(1), pp. 9-19.
- [112] H. Zhu, J. Xu, Y. Yichuan, Z. Wang, Y. Gao, W. Liu and H. Yin, "Catalytic oxidation of soot on mesoporous ceria-based mixed oxides with cetyltrimethyl ammonium bromide (CTAB)-assisted synthesis", *Journal of Colloid and Interface Science*, **2017**, 508, pp. 1-13.
- [113] J. Abboud, J. Schobing, G. Legros, J. Bonnetty, V. Tschamber, A. Brillard, G. Leyssens, V. Lauga, E. E. Iojoiu, P. Da Costa, "Impacts of oxygenated compounds concentration on sooting propensities and soot oxidative reactivity: Application to Diesel and Biodiesel surrogates", *Fuel*, **2017**, 193, pp. 241-253.
- [114] C. S. McEnally, L. D. Pfefferle, "Sooting tendencies of oxygenated hydrocarbons in laboratory-scale flames", *Environmental Science and Technology*, **2011**, 45(6), pp.2498-2503.
- [115] S. McEnally, L. D. Pfefferle, "Improved sooting tendency measurements for aromatic hydrocarbons and their implications for naphthalene formation pathways", *Combustion and Flame*, **2007**, 148(4), pp. 210-22.

- [116] M. Kashif, P. Guibert, J. Bonnetty, G. Legros, "Sooting tendencies of primary reference fuels in atmospheric laminar diffusion flames burning into vitiated air", *Combustion and Flame*, **2014**, 161(6), pp. 1575-1586.
- [117] R. J. Santoro, H. G. Semerjian, R. A. Dobbins, "Soot particle measurements in diffusion Flames", *Combustion and Flame*, **1983**, 51, pp. 203-218.
- [118] R. Lemaire, D. Lapalme and P. Seers, "Analysis of the sooting propensity of C-4 and C-5 oxygenates: Comparison of sooting indexes issued from laser-based experiments and group additivity approaches", *Combustion and Flame*, **2015**, 162, pp.3140-3155.
- [119] H. P. Ramirez, K. Hadj-Ali, P. Diévar, G. Moréac and P. Dagaut, "Kinetics of Oxidation of Commercial and Surrogate Diesel Fuels in a Jet-Stirred Reactor: Experimental and Modeling Studies", *Energy Fuels*, **2010**, 24(3), pp. 1668-1676.
- [120] H. P. Ramirez, K. Hadj-Ali, P. Diévar, G. Dayma, C. Togbé, G. Moréac and P. Dagaut, "Oxidation of commercial and surrogate bio-Diesel fuels (B30) in a jet-stirred reactor at elevated pressure: Experimental and modeling kinetic study", *Proceedings of the Combustion Institute*, **2011**, 33(1), pp. 375-382.
- [121] A. Mayer, H. Egli, H. Burtscher, J. Czerwinski et al., "Particle Size Distribution Downstream Traps of Different Design", *SAE Technical Paper*, **1995**.
- [122] A. Mayer, J. Czerwinski and P. Scheidegger, "Trapping Efficiency Depending on Particulate Size", *SAE Technical Paper*, **1996**.
- [123] L. L. N. Guarieiro and A. L. N. Guarieiro, "Impact of the Biofuels Burning on Particle Emissions from the Vehicular Exhaust", *INTECH, Biofuels-Status and Perspective*, **2015**, chapter 11.
- [124] D. B. Kittelson, "Engines and nanoparticles: a review", *Journal of Aerosol Science*, **1998**, 29(5-6), pp. 575-588.
- [125] "Biomass and Bio-fuels characterization using the Thermo Scientific FLASH 2000 CHNS/O Analyzer", Thermo Fisher Scientific, Milan, http://spectro-lab.pl/katalogisl/FLASH/FLASH_11.pdf
- [126] K. Ismail, "Fabrication and characterization of surface-enhanced Raman scattering substrates through photo-deposition of gold nanoparticles", Master Thesis, **2015**.
- [127] N. P. Ivleva, U. McKeon, R. Niessner and U. Pöschl, "Raman Microspectroscopic Analysis of Size Resolved Atmospheric Aerosol Particle Samples Collected with an ELPI: Soot, Humic-Like Substances, and Inorganic Compounds", *Aerosol Science and Technology*, **2007**, 41(7), pp. 655-671.
- [128] M. Knauer, M. E. Schuster, D. Su, R. Schlogl, R. Niessner and N. P. Ivleva, "Soot Structure and Reactivity Analysis by Raman Microspectroscopy, Temperature-Programmed Oxidation, and High-Resolution Transmission Electron Microscopy", *The Journal of Physical Chemistry A*, **2009**, 113(50), pp. 13871-13880
- [129] M. Knauer, M. Carrara, D. Rothe, R. Niessner and N. P. Ivleva, "Changes in Structure and Reactivity of Soot during Oxidation and Gasification by Oxygen, Studied by Micro-Raman Spectroscopy and Temperature Programmed Oxidation", *Aerosol Science and Technology*, **2009**, 43(1), pp. 1-8.
- [130] "Transmission electron Microscope: TEM electron Microscope", *Encyclopedia of Engineering, Ultimate core concepts of "Engineering"*, 2017, <http://www.mechscience.com/transmission-electron-microscope-temelectron-microscope/>.

- [131] J. Schmid, B. Grob, R. Niessner and N. P. Ivleva, "Multiwavelength Raman Microspectroscopy for Rapid Prediction of Soot Oxidation Reactivity", *Analytical Chemistry*, **2011**, 83(4), pp. 1173-1179.
- [132] H. Zhang, J. Wang, Y. Cao, Y. Wang, M. Gong and Y. Chen, "Effect of Y on improving the thermal stability of MnO_x-CeO₂ catalysts for diesel soot oxidation", *Chinese Journal of Catalysis*, **2015**, 36, pp. 1333-1341.
- [133] H.L. Zhang, S. Yuan, J. L. Wang, M. C. Gong and Y.Q. Chen, "Effects of contact model and NO_x on soot oxidation activity over Pt/MnO_x-CeO₂ and the reaction mechanisms", *Chemical Engineering Journal*, **2017**, 327, pp. 1066-1076.
- [134] C. K. Westbrook, W. J. Pitz and H. J. Curran, "Chemical Kinetic Modeling Study of the Effects of Oxygenated Hydrocarbons on Soot Emissions from Diesel Engines", *The Journal of Physical Chemistry*, **2006**, 110(21), pp. 6912-6922.
- [135] J. P. Szybist, A. L. Boehman, D. C. Haworth and H. Koga, "Premixed ignition behaviour of alternative diesel fuel-relevant compounds in a motored engine experiment", *Combust Flame*, vol.149, no.1-2, pp.112-128, 2007.
- [136] J. P. Szybist, J. Song, M. Alam and A. L. Boehman, "Biodiesel combustion, emissions and emission control", *Fuel Processing Technology*, **2007**, 88(7), pp.679-691.
- [137] P. Pepiot-Desjardins, H. Pitsch, R. Malhotra, S.R. Kirby and A.L. Boehman, "Structural group analysis for soot reduction tendency of oxygenated fuels", *Combustion and Flame*, **2008**, 154, 191-205.
- [138] Y-C. Lin, C-F. Lee and T. Fang, "Characterization of particle size distribution from diesel engines fueled with palm-biodiesel blends and paraffinic fuel blends", *Atmospheric Environment*, **2008**, 42, pp.1133-1143.
- [139] A. Puzun, S. Wanchen, L. Guoliang, T. Manzhi, L. Chunjie and C. Shibao, "Characteristics of Particle Size Distributions About Emissions in A Common-rail Diesel Engine with Biodiesel Blends", *Procedia Environmental Sciences*, **2011**, 11, pp.1371-1378.
- [140] American Scientist Magazine, February 2018, www.americanscientist.org
- [141] K. C. Lin, J. Y. W. Lai and A. Violi, "The role of the methyl ester moiety in biodiesel combustion: A kinetic modelling comparison of methyl butanoate and n-butane", *Fuel*, **2012**, 92(1), pp.16-26.
- [142] P. Pepiot-Desjardins, H. Pitsch, R. Malhotra, S.R. Kirby and A.L. Boehman, "Structural group analysis for soot reduction tendency of oxygenated fuels", *Combustion and Flame*, **2008**, 154, pp.191-205.
- [143] M. Lapuerta, F. Olivia, J. R. Agudelo and A. L. Boehman, "Effect of fuel on the soot nanostructure and consequences on loading and regeneration of diesel particulate filters", *Combustion and Flame*, **2012**, 159(2), pp.844-853.
- [144] M. N. Ess, H. Bladt, W. Mühlbauer, S. I. Seher, C. Zöllner, S. Lorenz, D. Brüggemann, U. Niekenc, N. P. Ivleva and R. Niessner, "Reactivity and structure of soot generated at varying biofuel content and engine operating parameters", *Combustion and Flame*, **2016**, 163, pp.157-169.
- [145] R. L. Vander Wal, A. Yezerets, N. W. Currier, D. H. Kim, C. M. Wang, "HRTEM Study of diesel soot collected from diesel particulate filters", *Carbon*, **2007**, 45(1), pp.70-77.
- [146] A. Strzelec, R. L. Vander Wal, T. N. Thompson, T. J. Toops and C. S. Daw, "NO₂ Oxidation Reactivity and Burning Mode of Diesel Particulates", *Topics in Catalysis*, **2016**, 59(8-9), pp.686-694.

- [147] N. Savic, M. M. Rahman, B. Miljevic, H. Saathoff, K. H. Naumann, T. Leisner, J. Riches, B. Gupta, N. Motta and Z. D. Ristovski, "Influence of biodiesel fuel composition on the morphology and microstructure of particles emitted from diesel engines", *Carbon*, **2016**, 104, pp.179-189.
- [148] W. Merchan-Merchan, S. G. Sanmiguel and S. McCollam, "Analysis of soot particles derived from biodiesels and diesel fuel air-flames", *Fuel*, **2012**, 102, pp.525-535.
- [149] A. Kumar, D-S. Kim and H. Omidvarborna et al., "Experimental Modeling of NO_x and PM Generation from Combustion of Various Biodiesel Blends for Urban Transport Buses", *Mineta National Transit Research Consortium*, **2016**.
- [150] J. M. Marchetti, V. U. Miguel and A. F. Errazu, "Possible methods for biodiesel production", *Renewable and Sustainable Energy Reviews*, **2007**, 11(6), pp.1300-1311.
- [151] S. P. Singh and D. Singh, "Biodiesel production through the use of different sources and characterization of oils and their esters as the substitute of diesel: A review", *Renewable and Sustainable Energy Reviews*, **2010**, 14(1), pp.200-216.
- [152] M. R. Kholghy, J. Weingarten, A. D. Sediako, J. Barba, M. Lapuerta and M. J. Thomson, "Structural effects of biodiesel on soot formation in a laminar coflow diffusion flame", *Proceedings of the Combustion Institute*, **2017**, 36(1), pp.1321-1328.
- [153] M. Frenklach and H. Wang, "Detailed modelling of soot particle nucleation and growth", *Twenty-Third Symposium (International) on Combustion*, **1990**, 23(1), pp.1559-1566.
- [154] H. Bockhorn, "Ultrafine particles from combustion sources: approaches to what we want to know", *Philosophical Transactions of The Royal Society A – Mathematical Physical and Engineering Sciences*, **2000**, no. 358(1775), pp. 2659-2672.
- [155] F. G. Emmerich, "Evolution with heat treatment of crystallinity in carbons", *Carbon*, **1995**, 33(12), pp. 1709-1715.
- [156] M. Levy and P. Wong, "The Oxidation of Pyrolytic Graphite at Temperatures of 1400°–1800°F and at Air Velocities of 25–100 cm/sec", *Journal of Electrochemical Society*, **1964**, 111(9), pp.1088-1091.
- [157] I. Morjan, I. Voicu, R. Alexandrescu, I. Pasuk, I. Sandu et al., "Gas composition in laser pyrolysis of hydrocarbon-based mixtures: Influence on soot morphology", *Carbon*, **2004**, 42(7), pp. 1269-1273.
- [158] Z. Li, L. Qiu, X. Cheng, Y. Li and H. Wu, "The evolution of soot morphology and nanostructure in laminar diffusion flame of surrogate fuels for diesel", *Fuel*, **2018**, 211, pp.517-528.
- [159] Z. Ma, L. Li, Y. Chao, N. Kang, B. Xu and J. Wu, "Effects of Diesel Oxidation Catalyst on Nanostructure and Reactivity of Diesel Soot", *Energy & Fuels*, **2014**, 28(7), pp.4376-4382.
- [160] A. W. Kandas, I. G. Senel, Y. Levendis and A. F. Sarofim, "Soot surface area evolution during air oxidation as evaluated by small angle X-ray scattering and CO₂ adsorption", *Carbon*, **2005**, 43(2), pp. 241-251.
- [161] R. Peterson, "The Oxidation Rate of Diesel Particulate Which Contains Lead", *SAE Technical Paper*, **1987**.
- [162] B. Stanmore, J. Brillhac and P. Gilot, "The ignition and Combustion of Cerium Doped Diesel Soot", *SAE Technical Paper*, **1999**.

- [163] J. Song, M. Alam and A. L. Boehman, "Characterization of Diesel and Biodiesel soot", *Prepr. Pap.-Am. Chem. Soc. Div. Fuel Chem.*, **2004**, 49(2), pp.767-769.
- [164] T. Seguelong and W. Naschke, "Series application of a diesel particulate filter with a Ceria-based Fuel-Borne Catalyst", *MTZ worldwide*, **2002**, 63(3), pp. 13-15.
- [165] B.R. Stanmore, J.F. Brilhac, P. Gilot, "The oxidation of soot: a review of experiments, mechanisms and models", *Carbon*, **2001**, 39(15), pp. 2247-2268.
- [166] A. Setiabudi, M. Makkee and J. A. Moulijn, "The role of NO₂ and O₂ in the accelerated combustion of soot in diesel exhaust gases", *Applied Catalysis B: Environmental*, **2004**, 50(3), pp.185-194.
- [167] R. Matarrese, L. Castoldi and L. Lietti, "Oxidation of model soot by NO₂ and O₂ in the presence of water vapor", *Chemical Engineering Science*, **2017**, 173, pp.560-569.
- [168] I. Atribak, A. Bueno-López, A. García-García, "Uncatalysed and catalysed soot combustion under NO_x+O₂: Real diesel versus model soots", *Combustion and Flame*, **2010**, 157(11), pp.2086-2094.
- [169] M. Issa, H. Mahzoul, A. Brillard and J-F. Brilhac, "Catalytic Carbon Oxidation in The Presence of Cerium Oxide: Experimental Study and Modeling of The Effect of Oxygen Concentration", *Chemical Engineering Technology*, **2009**, 32(12), pp.1859-1865.
- [170] P. A. Kumar, M. D. Tanwar, S. Bensaid, N. Russo and D. Fino, "Soot combustion improvement in diesel particulate filters catalysed with ceria nanofibers", *Chemical Engineering Journal*, **2012**, 207-208, pp.258-266.
- [171] P. Miceli, S. Bensaid, N. Russo and D. Fino, "CeO₂-based catalysts with engineered morphologies for soot oxidation to enhance soot-catalyst contact", *Nanoscale Research Letters*, **2014**, 9, pp.254-263.
- [172] M. Piumetti, S. Bensaid, N. Russ and D. Fino, "Nanostructured ceria-based catalysts for soot combustion: Investigations on the surface sensitivity", *Applied Catalysis B: Environmental*, **2015**, 165, pp.742-751.
- [173] M. Issa, C. Petit, A. Brillard and J.F. Brilhac, "Oxidation of carbon by CeO₂: Effect of the contact between carbon and catalytic particles", *Fuel*, **2008**, 87(6), pp.740-750.
- [174] N. Zouaoui, M. Issa, D. Kehrlí and M. Jeguirim, "CeO₂ catalytic activity for soot oxidation under NO/O₂ in loose and tight contact", *Catalysis Today*, **2012**, 189(1), pp.65-69.
- [175] J. P. A. Neeft, M. Makkee and J. A. Moulijn, "Catalysts for the oxidation of soot from diesel exhaust gases. I. An exploratory study", *Applied Catalysis B: Environmental*, **1996**, 8(1), pp.57-78.
- [176] J. Christensen, J-D. Grunwaldt and A. D. Jensen, "Importance of the oxygen bond strength for catalytic activity in soot oxidation", *Applied Catalysis B: Environmental*, **2016**, 188, pp.235-244.
- [177] D. Gardini, J. M. Christensen, C. D. Damsgaard, A. D. Jensen and J. B. Wagner, "Visualizing the mobility of silver during catalytic soot oxidation", *Applied Catalysis B: Environmental*, **2016**, 183, pp.28-36.

THIS PAGE WAS INTENTIONALLY LEFT BLANK

8 Appendix

A. TEM image processing with *Image J*®

The measurement of carbon fringe length of different soot particles was carried out with TEM micrographs obtained at high resolution. In this case, it was possible to distinguish graphene layers and measure the length of parallel carbon segments.

The first step consisted on the conversion of a digital image composed by a matrix of elements, which are called pixels, into a value in nanometres. For instance, as it can be observed in [Figure A- 1](#), 5 nm correspond to 361 pixels. Thus, when a line is traced, the software immediately converts the distance in nanometres (nm).

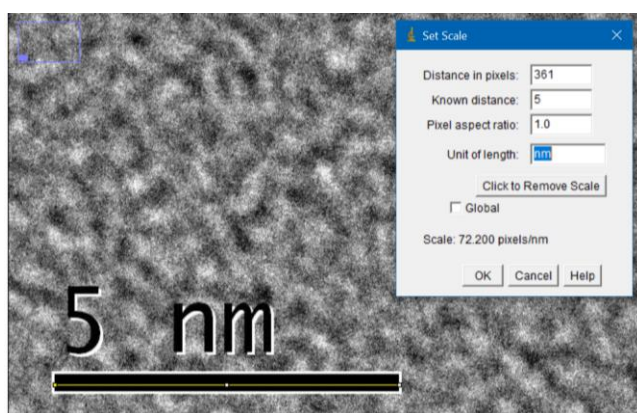


Figure A- 1. Definition of the scale (conversion of pixels into nanometres).

The next step was to select the area of interest ([Figure A- 2](#)). This selection must be done carefully because in some images different particles can be superimposed.

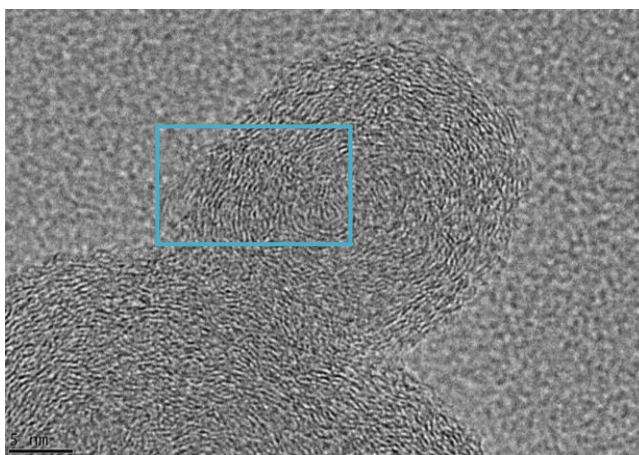


Figure A- 2. Selection of the area of interest (blue square).

The third step was to apply a filter and to reduce the electronic noise ([Figure A- 3](#)). This step is important to obtain well defined structures.

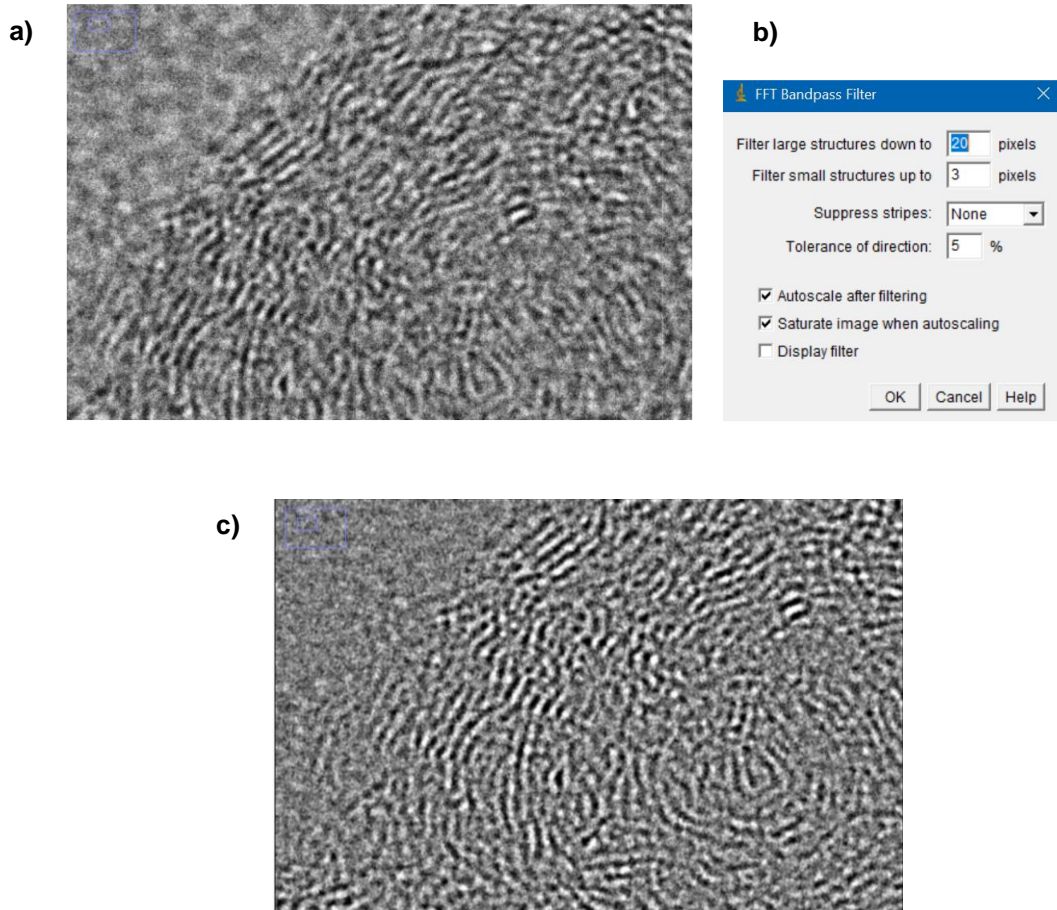


Figure A- 3. a) Zone of interest. b) Application of a filter and reduction of the noise. c) Filtered image.

Finally, the filtered image was transformed into a binary format by setting a threshold brightness value. In this study, the filtering and thresholding of each micrograph was done manually based on operator’s judgement. The objective was to obtain an image which could clearly show the graphene layers that compose soot particles. Single phase regions, surrounded by the opposite phase (and hence isolated from the other regions of the same phase), were identified as objects, in this case as fringes (Figure A- 4).

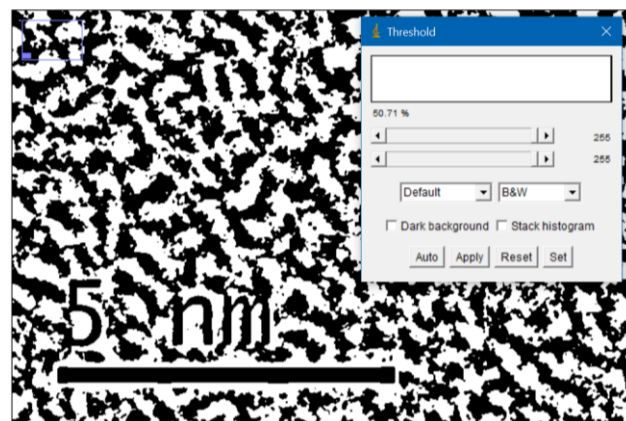


Figure A- 4. Application of a threshold brightness value (conversion into a binary format).

The distribution of fringe length was obtained by measuring the length of at least 400 parallel fringes, manually (Figure A- 5), from different TEM images (~10 images for each sample). For the spherules diameter, the same procedure was followed but the results were not presented as a distribution curve due to the reduced amount of collected data.

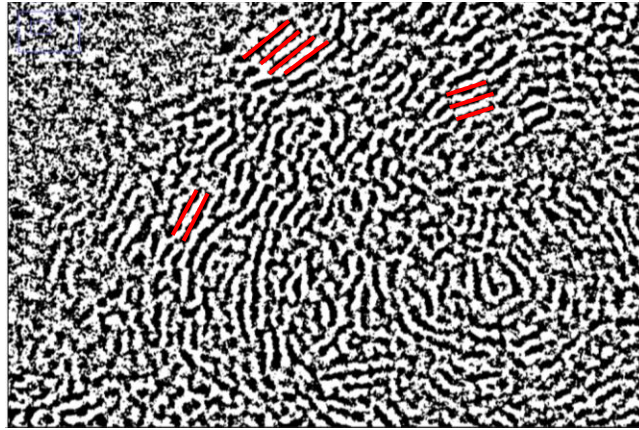


Figure A- 5. Measurement of the length of parallel carbon fringes.

B. Calculation of soot conversion

In order to obtain the temperature at 10, 50 and 90% of soot conversion, it was assumed that all the carbon present in the sample was converted into CO and CO₂. Thus, the calculation was made in terms of CO_x emissions (ppm) along all the experiment. For each time interval (2 seconds), CO_x emissions were cumulated and converted in percentage (%). Then, a cumulative curve was made in function of the temperature (Figure B- 1).

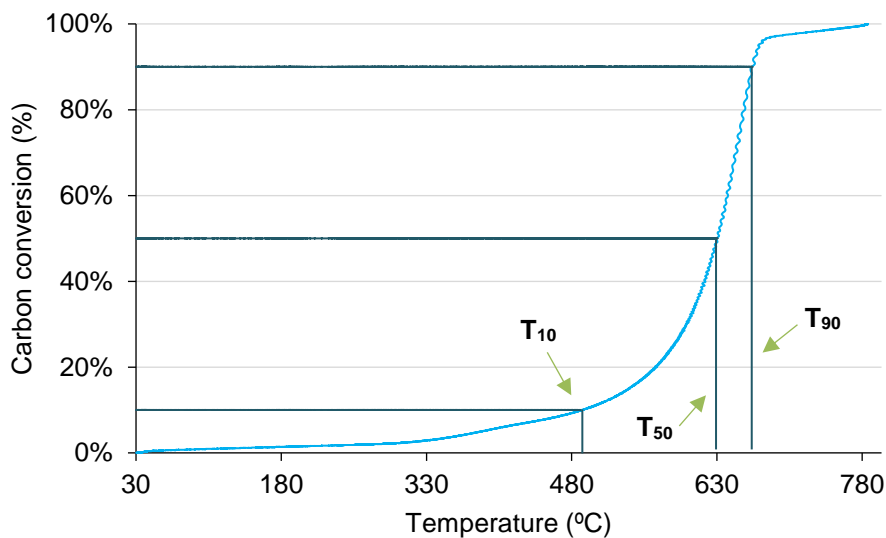


Figure B- 1. Cumulative curve of CO_x emissions in function of the temperature for «B100-BM» sample, under 9% O₂/Ar.

C. Laser particle size analysis

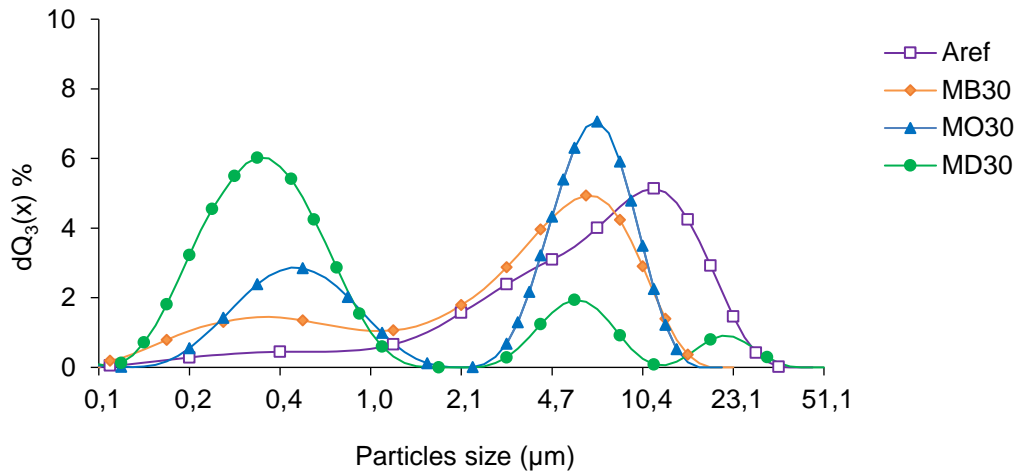


Figure C- 1. Size distribution of “model” soot aggregates from the diesel surrogate and biodiesel surrogates (30%).

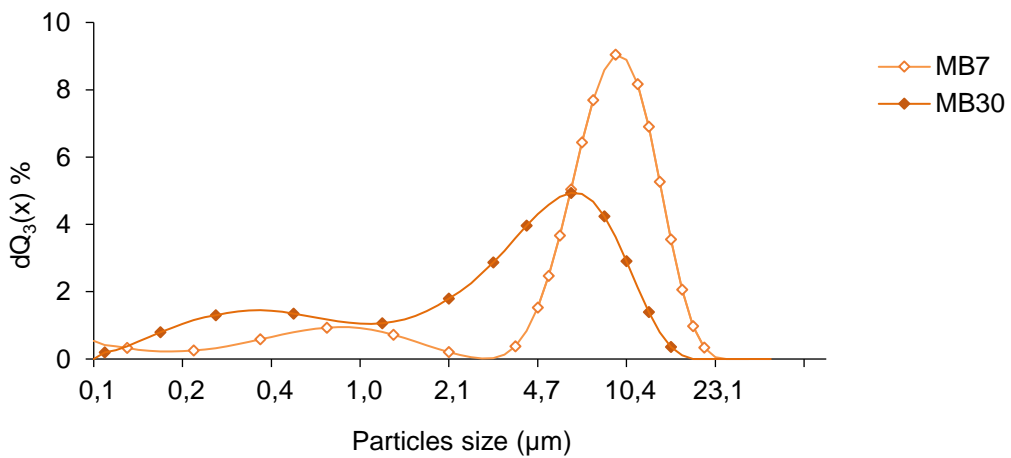


Figure C- 2. Size distribution of “model” soot aggregates from biodiesel surrogates with 7 and 30% of methyl butanoate.

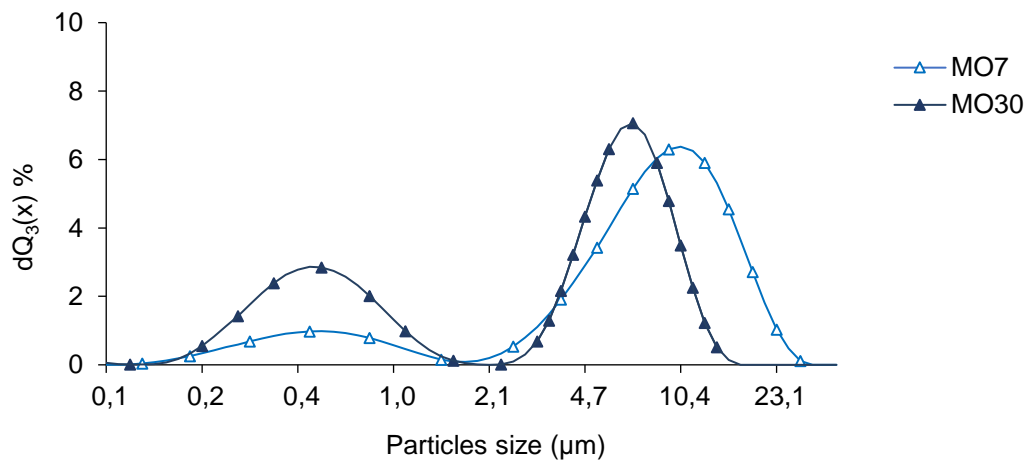


Figure C- 3. Size distribution of “model” soot aggregates from biodiesel surrogates with 7 and 30% of methyl octanoate.

D. Thermogravimetric analysis (TGA)

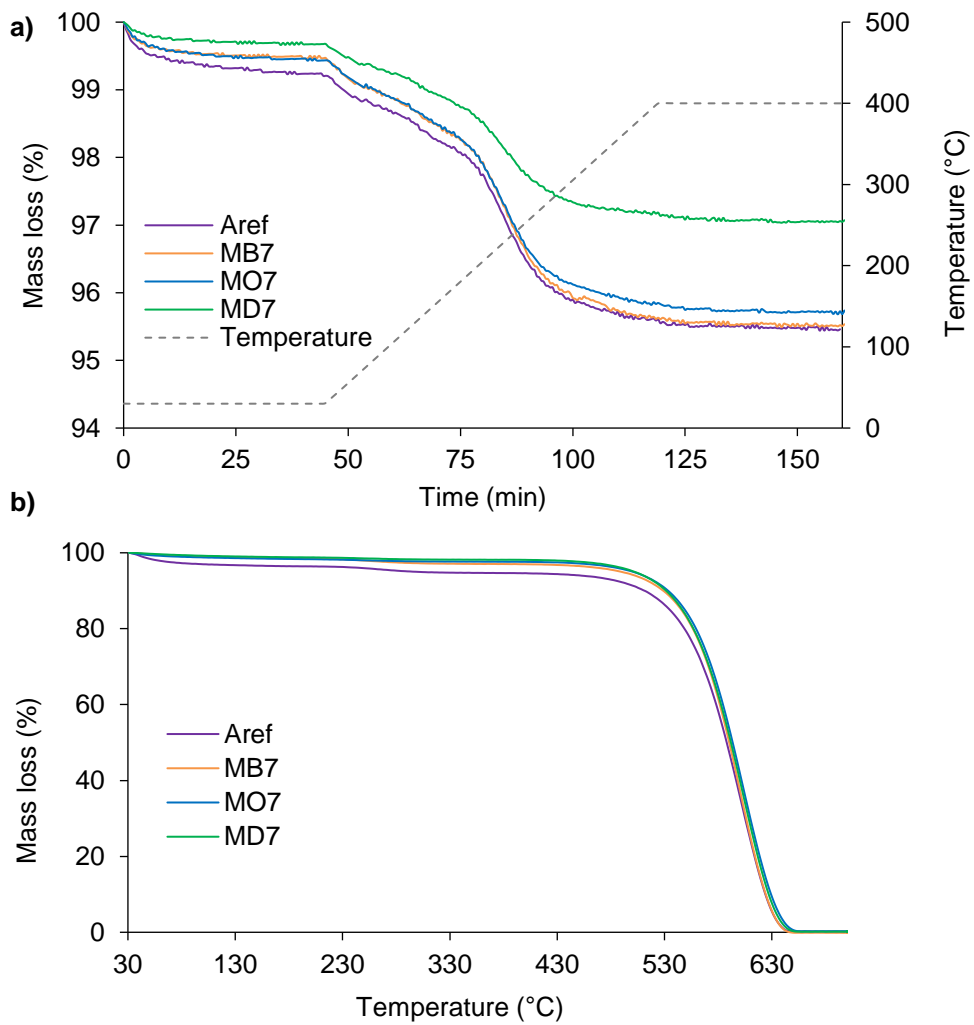
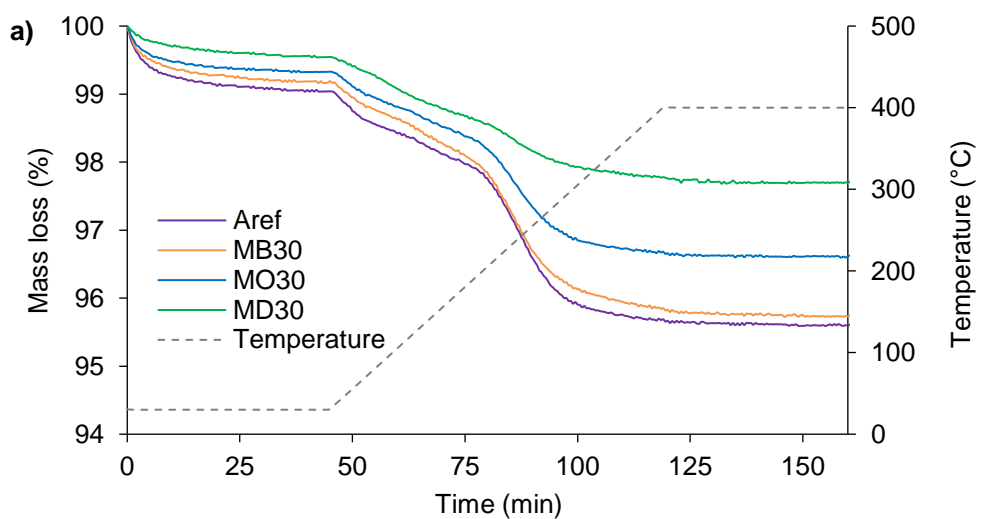


Figure D- 1. Thermogravimetric analysis under nitrogen (a) and under air (b) of "model" soot from biodiesel surrogates with 7% of methyl ester-based additives and from diesel surrogate «Aref».



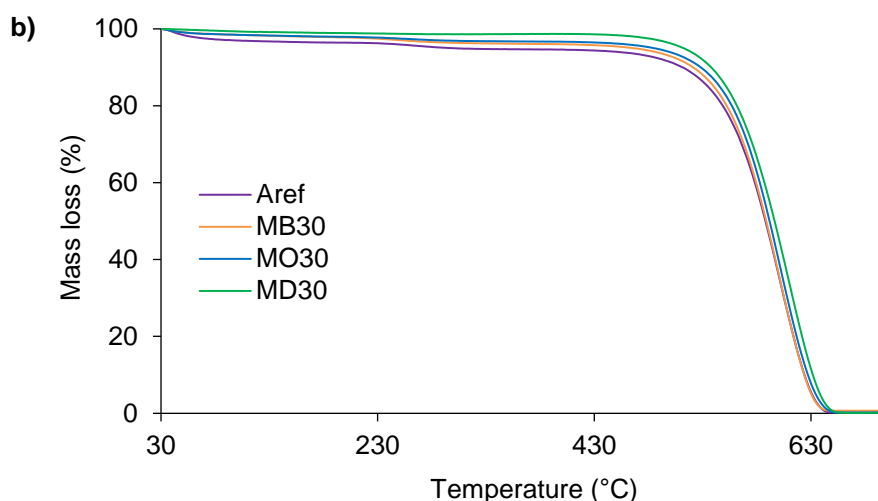


Figure D- 2. Thermogravimetric analysis under nitrogen (a) and under air (b) of “model” soot from biodiesel surrogates with 30% of methyl ester-based additives and from diesel surrogate «Aref».

E. Raman Spectroscopy

Table E- 1. Results of Raman spectroscopy for «Aref» soot.

Band	Relative intensity	Raman shift (cm⁻¹)	FWHM
G	1,85	1589	68
D1	2,41	1335	120
D2	0,20	1616	50
D3	1,10	1512	220
D4	0,40	1219	192

Table E- 2. Results of Raman spectroscopy for «MB7» soot.

Band	Relative intensity	Raman shift (cm⁻¹)	FWHM
G	1,81	1590	66
D1	2,32	1337	130
D2	0,39	1618	50
D3	1,12	1523	200
D4	0,40	1225	300

Table E- 3. Results of Raman spectroscopy for «MO7» soot.

Band	Relative intensity	Raman shift (cm⁻¹)	FWHM
G	1,77	1590	64
D1	2,35	1337	126
D2	0,51	1620	70
D3	0,97	1511	174
D4	0,35	1224	240

Table E- 4. Results of Raman spectroscopy for «MD7» soot.

Band	Relative intensity	Raman shift (cm⁻¹)	FWHM
G	1,70	1593	66
D1	2,29	1342	118
D2	0,41	1616	100
D3	1,11	1512	200
D4	0,48	1241	220

Table E- 5. Results of Raman spectroscopy for «MB30» soot.

Band	Relative intensity	Raman shift (cm⁻¹)	FWHM
G	1,95	1587	65
D1	2,39	1332	128
D2	0,18	1618	50
D3	1,14	1515	187
D4	0,42	1219	293

Table E- 6. Results of Raman spectroscopy for «MO30» soot.

Band	Relative intensity	Raman shift (cm⁻¹)	FWHM
G	1,89	1591	65
D1	2,52	1337	121
D2	0,09	1623	52
D3	1,14	1517	204
D4	0,37	1219	146

Table E- 7. Results of Raman spectroscopy for «MD30» soot.

Band	Relative intensity	Raman shift (cm⁻¹)	FWHM
G	1,97	1585	62
D1	2,71	1334	113
D2	0,18	1616	40
D3	1,07	1514	220
D4	0,39	1241	172

Table E- 8. Results of Raman spectroscopy for «B7-BM» soot.

Band	Relative intensity	Raman shift (cm ⁻¹)	FWHM
G	1,09	1590	69
D1	1,44	1342	141
D2	0,10	1620	174
D3	0,62	1514	169
D4	0,21	1232	130

Table E- 9. Results of Raman spectroscopy for «B100-BM» soot.

Band	Relative intensity	Raman shift (cm ⁻¹)	FWHM
G	1,12	1588	70
D1	1,38	1340	134
D2	0,09	1620	198
D3	0,63	1508	172
D4	0,29	1233	155

F. Transmission Electron Microscopy (TEM)

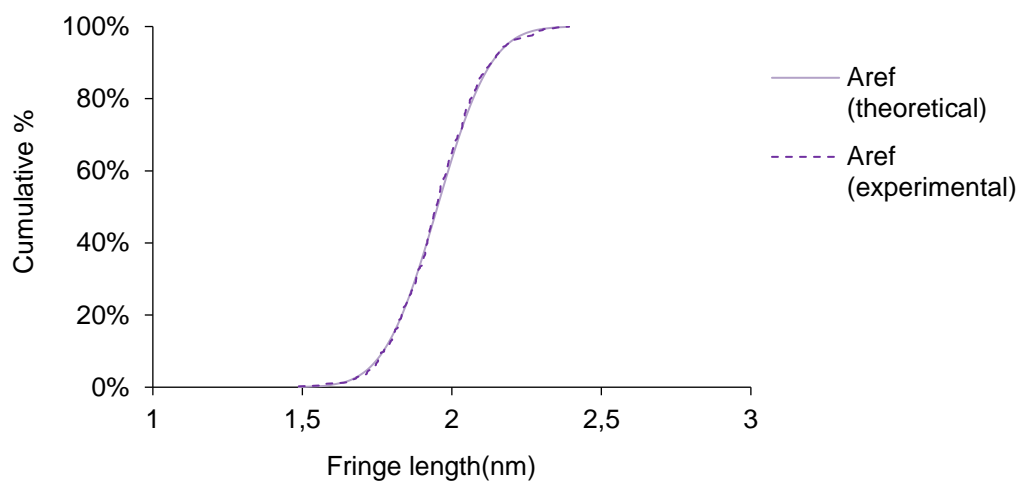


Figure F- 1. Theoretical and experimental cumulative curves of «Aref» size distribution.

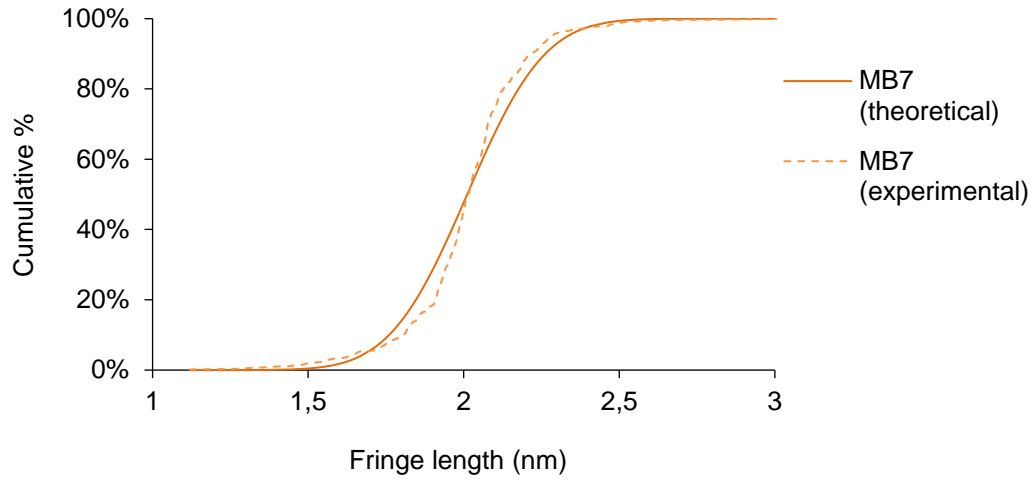


Figure F- 2. Theoretical and experimental cumulative curves of «MB7» size distribution.

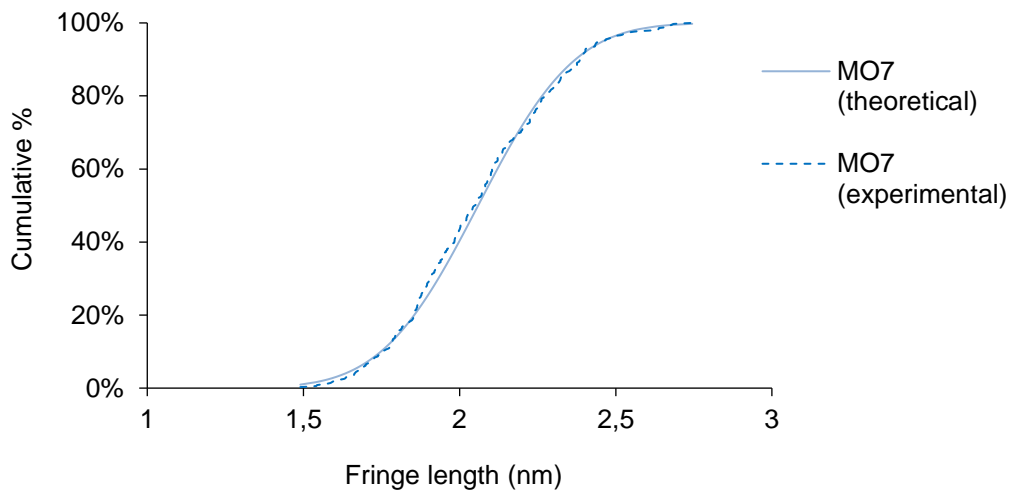


Figure F- 3. Theoretical and experimental cumulative curves of «MO7» size distribution.

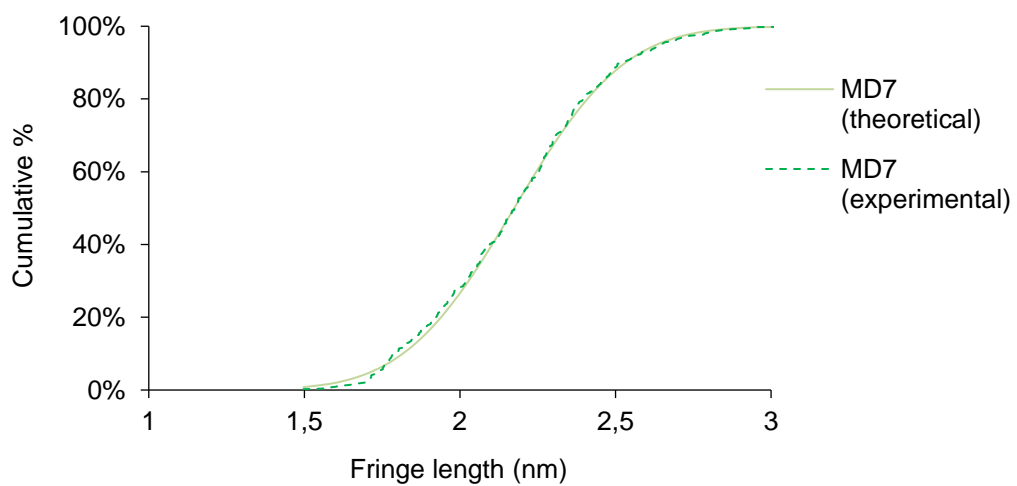


Figure F- 4. Theoretical and experimental cumulative curves of «MD7» size distribution.

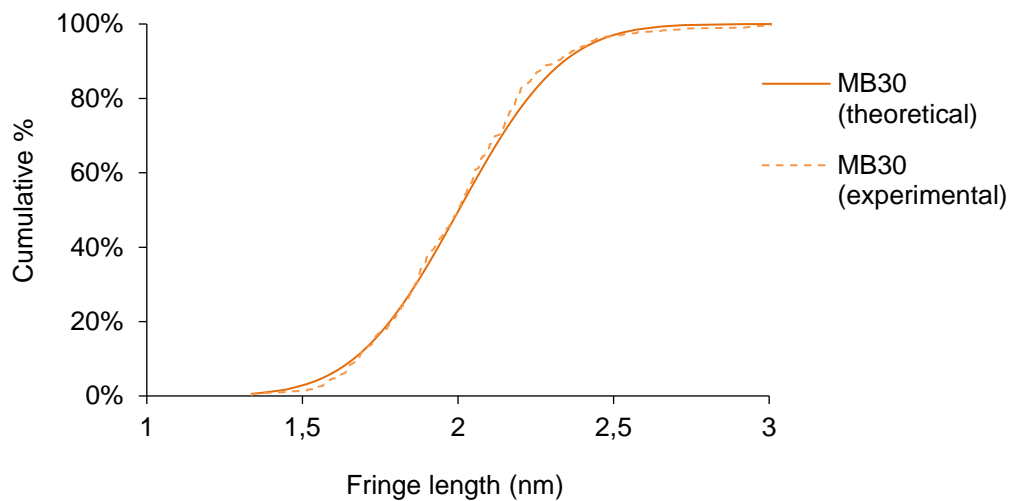


Figure F- 5. Theoretical and experimental cumulative curves of «MB30» size distribution.

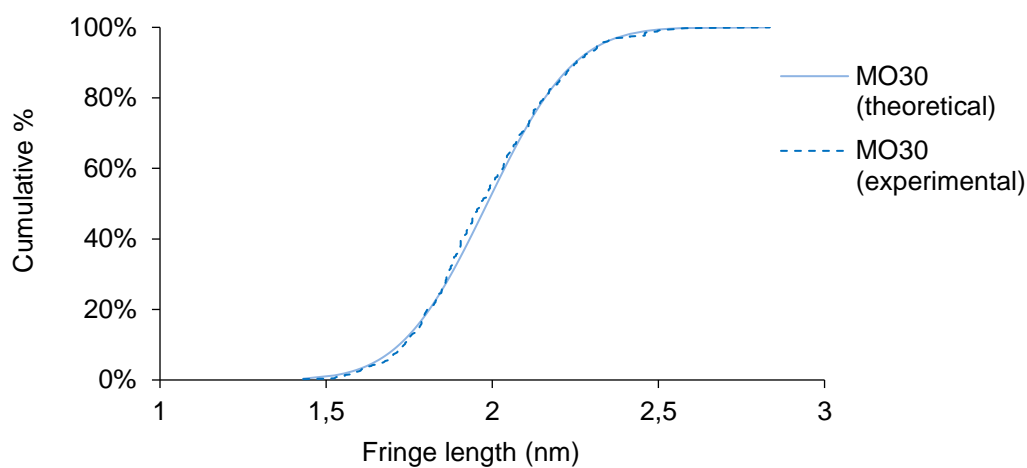


Figure F- 6. Theoretical and experimental cumulative curves of «MO30» size distribution.

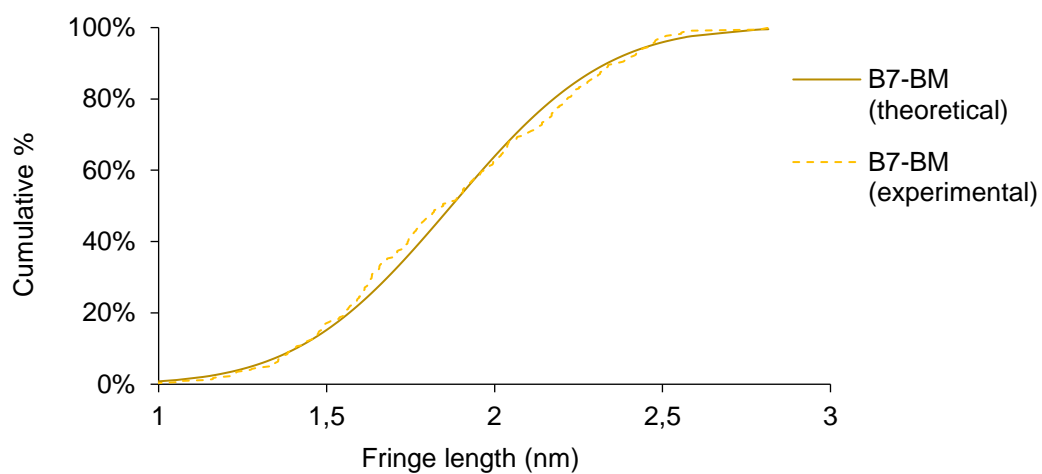


Figure F- 7. Theoretical and experimental cumulative curves of «B7-BM» size distribution.

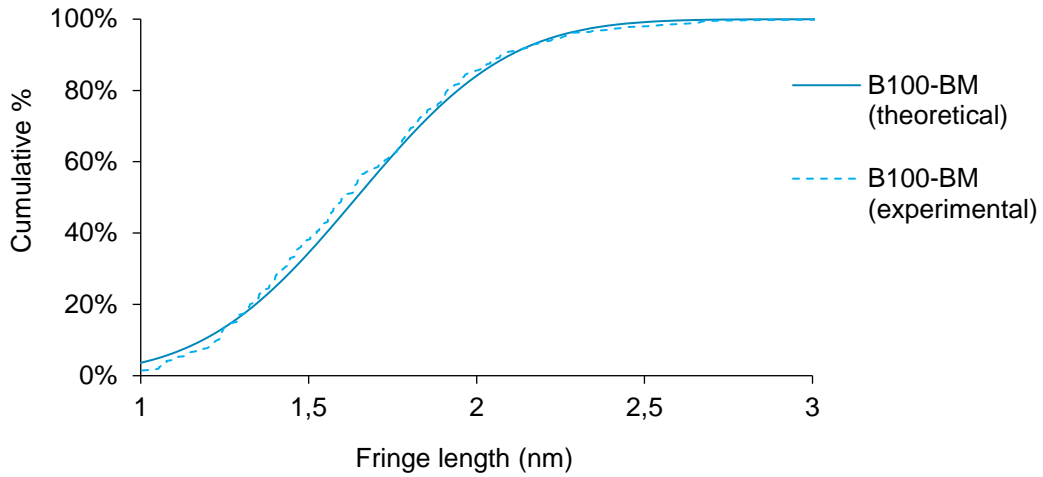


Figure F- 8. Theoretical and experimental cumulative curves of «B100-BM» size distribution.

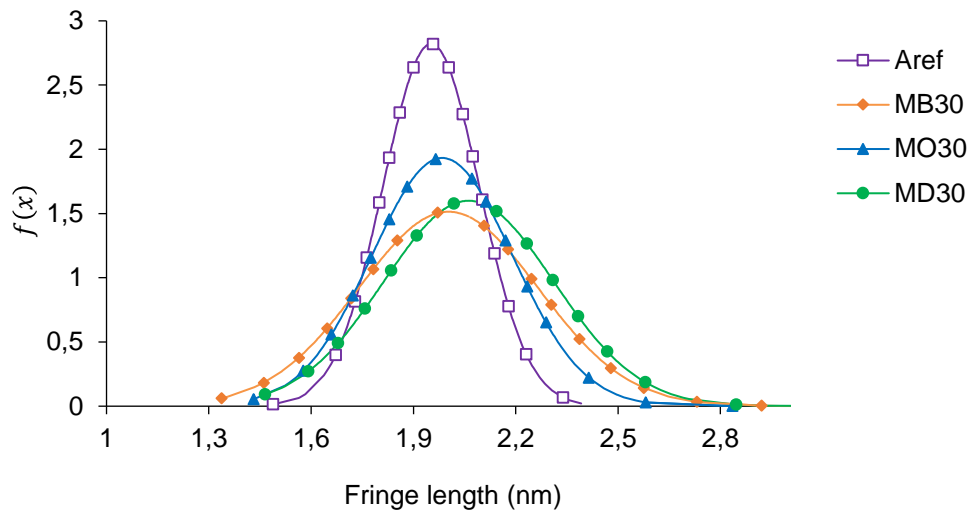


Figure F- 9. Carbon fringe length distribution of soot produced by combustion of «Aref» and biodiesel surrogates with 30% of methyl ester-based additives.

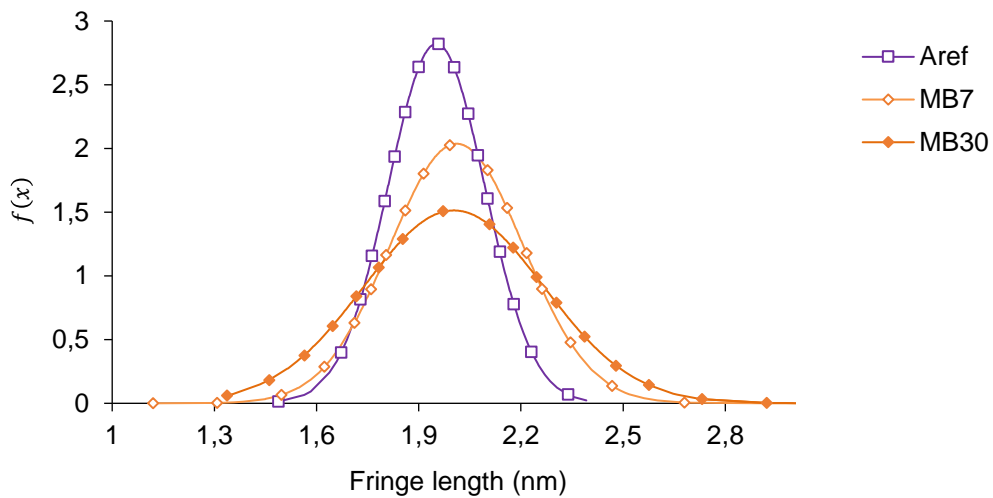


Figure F- 10. Carbon fringe length distribution of soot produced by combustion of «Aref» and biodiesel surrogates with 7 and 30% of methyl butanoate.

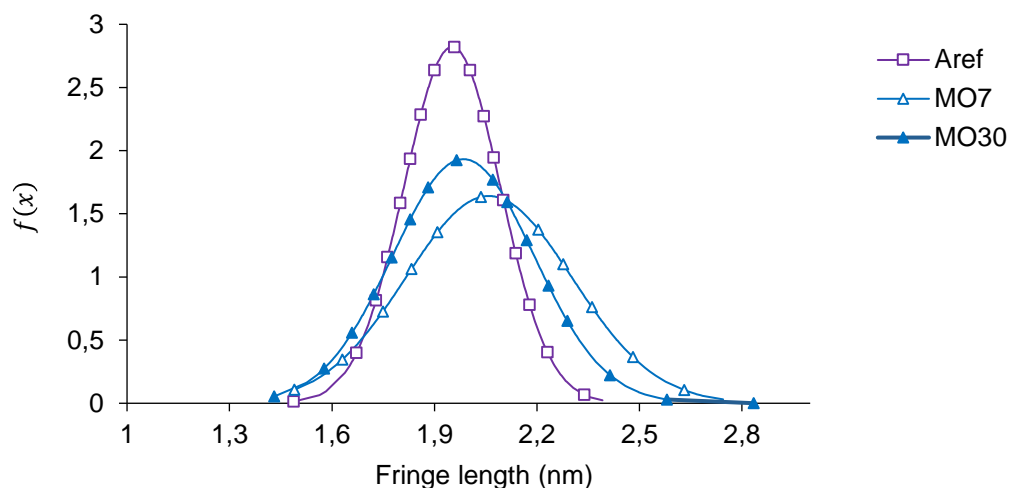


Figure F- 11. Carbon fringe length distribution of soot produced by combustion of «Aref» and biodiesel surrogates with 7 and 30% of methyl octanoate.

G. Characterization of MnO_x-CeO₂ mixed oxides

The chemical compositions located on the surface of the catalysts have an important role in the soot oxidation reactivity. Table G- 1 shows the relative content of the surface chemical components of the catalyst, obtained by X-ray photoelectron spectroscopy (XPS) [132].

Table G- 1. XPS results of the MnO_x-CeO₂ catalyst.

Element (at%)		Ce (at%)		Mn (at%)			O (at%)	
Ce	Mn	Ce ⁴⁺	Ce ³⁺	Mn ⁴⁺	Mn ³⁺	Mn ²⁺	O _{latt}	O _{sur} +O _{ads}
16,3	2,7	14,2	2,1	1,15	0,27	0,50	32,3	48,7

H. Temperature programmed oxidation (TPO)

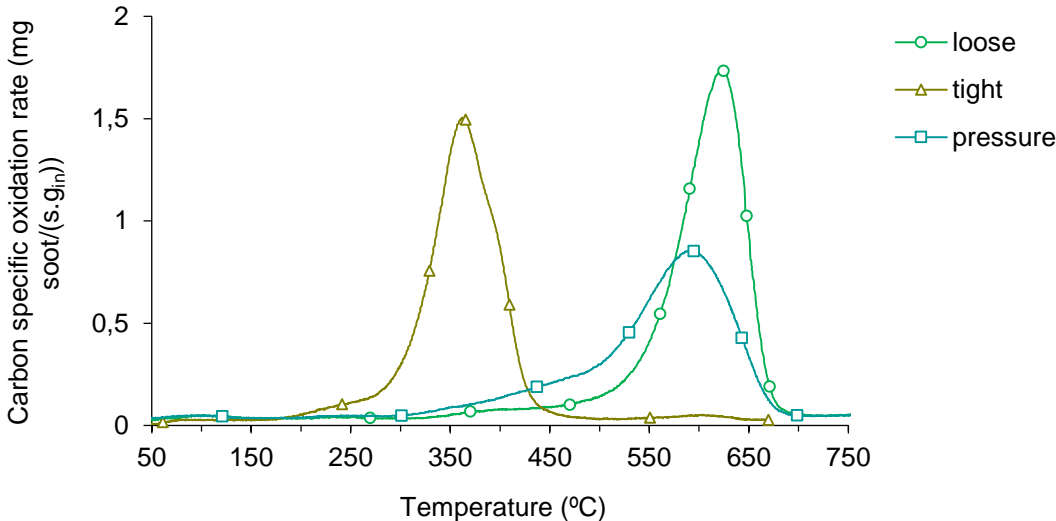


Figure H- 1. Carbon specific oxidation rate (mg/(s.g_{in})) of «MD7» soot, in loose, pressure and tight contact conditions, under 9%O₂ and 91%Ar.

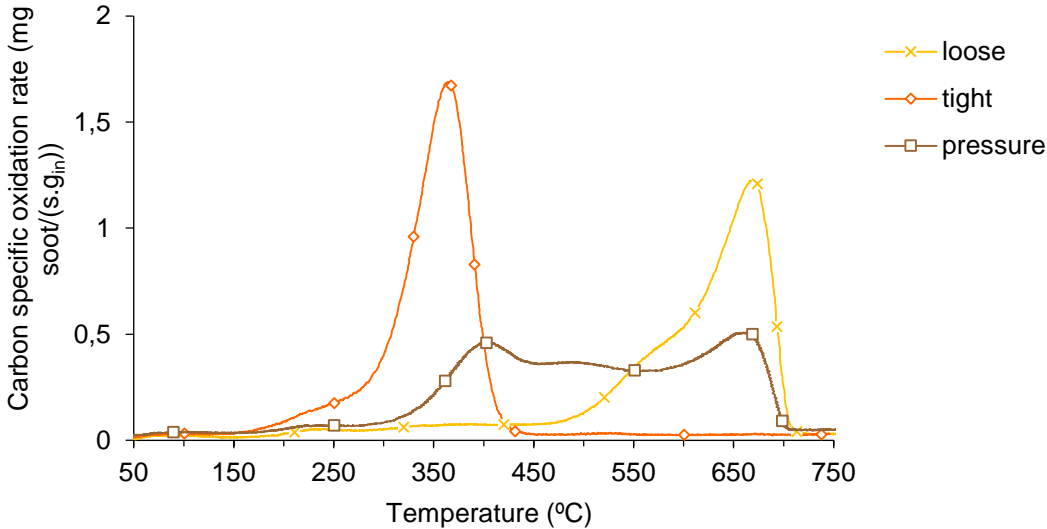


Figure H- 2. Carbon specific oxidation rate (mg/(s.g_{in})) of «B7-BM» soot, in loose, pressure and tight contact conditions, under 9%O₂ and 91%Ar.